ÉCOLE DE TECHNOLOGIE SUPÉRIEURE
UNIVERSITÉ DU QUÉBEC

THESIS PRESENTED TO
ÉCOLE DE TECHNOLOGIE SUPÉRIEURE

IN FULFILLMENT OF THE THESIS REQUIREMENT
FOR THE DEGREE OF DOCTOR OF PHILOSOPHY
Ph.D.

BY
ZHENGKUN FENG

A NONLINEAR COMPUTATIONAL AEROELASTICITY MODEL FOR AIRCRAFT WINGS

MONTREAL, AUGUST 3, 2005

THIS THESIS WAS EVALUATIED

BY THE COMMITTEE COMPOSED BY :

Dr. Azzeddine Soulaïmani – Thesis Supervisor

Département de Génie Mécanique, École de technologie supérieure

Dr. Christian Masson – President

Département de Génie Mécanique, École de technologie supérieure

Dr. Van Ngan Le – Examiner

Departement de Génie Mécanique, École de technologie supérieure

Dr. Stuart J. Price – External Examiner

Department of Mechanical Engineering, Mcgill University

THIS THESIS WAS DEFENDED IN FRONT OF THE EXAMINATION

COMMITTEE AND THE PUBLIC

ON JULY 12, 2005

AT ÉCOLE DE TECHNOLOGIE SUPÉRIEURE

A NONLINEAR COMPUTATIONAL AEROELASTICITY MODEL FOR AIRCRAFT WINGS

Zhengkun Feng

ABSTRACT

The design of a large aircraft at high speeds is a challenge in the very active research on aeroelasticity. The computational aeroelasticity analysis in 3D for such a large system of nonlinear equations becomes available due to the recent highly developed computing technology.

This thesis deals with the development of a CFD-based coupling code which is based on the equations of the structural motion and the Euler equations of inviscid compressible transonic flows. The strategy of segregating such a complex multidisciplinary system gives the advantages of the software development in modularity and the reuse of the developed solvers of the subsystems. The non-matching of the grids on the fluid-structure interface due to the difference of the element sizes and types of the fluid and the structural models is resolved by adding the matcher module in the coupling algorithm. The information transfers from one solver to another satisfy conservation of energy. The nonlinear aerodynamic model is described by the kinematic ALE description and discretized on the moving mesh which is updated by the mesh solver. The CSD-MAM model in which the modal superposition approach is based on the linear structural theories is used to reduce the computing time and the memory consumption. Another comparable CSD-FEM model based directly on the finite element discrete approach is also built for the extension to general structural dynamics. The nonlinearity is another source of the complexity of the aeroelasticity model although it is assumed only from the aerodynamics of the transonic flow and from the geometric nonlinearities due to the mesh motion. The nonlinear GMRES algorithm with the ILUT preconditioner is implemented in the robust CFD solver where the SUPG numerical stabilization techniques and a shock captor are applied to the transonic flow dominated by convection. The second order Gear-Scheme is used for the time discretization.

The components of this nonlinear computational aeroelasticity model are validated one by one with numerical experiments. The complete model is validated by the AGARD 445.6 aeroelastic wing immersed in transonic flows with Mach number 0.96 which corresponds to the lowest point of the transonic dip. The flutter simulations have given satisfying results compared to experimental ones.

UN MODÈLE DE CALCUL NUMÉRIQUE DE L'AÉROELASTICITÉ NONLINÉARE POUR DES AILES D'AVIONS

Zhengkun Feng

SOMMAIRE

Cette thèse présente le développement d'un code d'aéroélasticité nonlinéaire basé sur un solveur CFD robuste afin de l'appliquer aux ailes flexibles en écoulement transsonique. Le modèle mathématique complet est basé sur les équations du mouvement des structures et les équations d'Euler pour les écoulements transsoniques non-visqueux. La stratégie de traiter tel système complexe par un couplage étagé présente des avantages pour le développement d'un code modulaire et facile à faire évoluer. La non-correspondance entre les deux grilles de calcul à l'interface fluide-structure, due aux différences des tailles et des types des éléments utilisés par la résolution de l'écoulement et de la structure, est résolue par l'ajout d'un module spécifique. Les transferts des informations entre ces deux grilles satisfont la loi de la conservation de l'énergie. Le modèle nonlinéaire de la dynamique du fluide basé sur la description Euler-Lagrange est discrétisé dans le maillage mobile. Le modèle pour le calcul des structures est supposé linéaire dans lequel la méthode de superposition modale est appliquée pour réduire le temps de calcul et la dimension de la mémoire. Un autre modèle pour la structure basé directement sur la méthode des éléments finis est aussi développé. Il est également couplé dans le code pour prouver son extension future aux applications plus générales. La nonlinéarité est une autre source de complexité du système bien que celle-ci est prévue uniquement dans le modèle aérodynamique. L'algorithme GMRES nonlinéaire avec le preconditioneur ILUT est implémenté dans le solveur CFD où un capteur de choc pour les écoulements transsoniques et la technique de stabilisation numérique SUPG pour des écoulements dominés par la convection sont appliqués. Un schéma du second ordre est utilisé pour la discrétisation temporelle.

Les composants de ce code sont validés par des tests numériques. Le modèle complet est appliqué et validé sur l'aile aéroélastique AGARD 445.6 dans le cas du nombre de Mach 0.96 qui est une valeur critique en flottement. Les simulations de flottement donnent des résultats numériques satisfaisants en comparaison avec ceux expérimentaux.

UN MODÈLE DE CALCUL NUMÉRIQUE DE L'AÉROELASTICITÉ NONLINÉARE POUR DES AILES D'AVIONS

Zhengkun Feng

RÉSUMÉ

La conception d'un avion en vol transsonique mène souvent aux ailes de grandes tailles et flexibles qui ont besoin d'être stables de point de vue aéroélastique. L'avancement des technologies du calcul scientifique permet de trouver des solutions numériques pour des systèmes complexes avec des équations nonlinéaires et de grandes tailles qui étaient nonaccessibles dans le passé. Pourtant, la simulation numérique reste encore difficile en aéroelasticité nonlinéaire. Cela à cause de deux volets de complexité dans l'analyse de l'aéroélasticité : la nonlinéarité des écoulements transsonique et l'interaction nonlinéaire entre le fluide et la structure. Premièrement, un modèle classique décrit par l'aéroélasticité linéaire n'est plus suffisant, car le choc et son mouvement ont besoin d'une description précise. Deuxièmement, l'aéroélasticité se traduit en interaction fluide-structure, où les déplacements d'une structure dans un écoulement affectent la configuration de celui-ci. En revanche, la variation d'efforts aérodynamiques induite par le changement de la configuration de l'écoulement provoque elle-même un impact aux déplacements de la structure. Donc, la modélisation de l'aéroélasticité de tel système conduit à établir des équations nonlinéaires par la dynamique de la structure et la dynamique du fluide.

Historiquement, l'évolution du calcul en aéroélasticité de la théorie linéaire vers la théorie nonlinéaire est accompagnée par l'avancement de la technologie informatique. Lorsqu'un avion subsonique qui avait une vitesse moins élevée et la limite de puissance du calcul numérique était un obstacle, l'aéroélasticité linéaire était appliquée pour obtenir des résultats accessibles. Au cours de l'augmentation de la vitesse d'avions, l'aéroélasticité linéaire appliquée aux écoulements transsoniques donne des résultats incohérents avec les résul-

tats expérimentaux. Différentes méthodes basées sur l'aéroélasticité nonlinéaire sont proposées pour tenter à franchir la surdimension des ailes d'avions dans la conception. Par exemple, la méthode basée sur les équations potentielles et sa variante TSD (une méthode basée sur les équations potentielles aux petites perturbations transsoniques) pouvaient décrire l'aérodynamique transsonique en utilisant les outils informatiques disponibles. Évidemment, cela donne des résultats moins précis. Des solutions de haute précision nécessitent des modèles basés sur des hypothèses plus précises.

Dans cette thèse, l'écoulement est supposé non-visqueux, compressible et rotationnel qui est traduit par les équations d'Euler. Ces équations aux dérivées partielles de l'ordre élevé possèdent une forte nonlinéarité. Malgré que la nonlinéarité peut aussi provenir de la structure, il est supposé que la structure est linéaire dans cette thèse. En effet, on s'intéresse à reproduire en premier lieu le phénomène de flottement en présence de petits déplacements de la structure (stabilité autour d'un point d'équilibre).

La complexité de l'aéroélasticité est aussi caractérisée par sa multidisciplinarité. La simulation numérique par la résolution d'une série d'équations nécessite le développement d'un code efficace, robuste et susceptible de le faire évoluer. La stratégie de couplage fluide-structure suppose que le modèle numérique est constitué de deux solveurs de calcul fluide (CFD) et de calcul structural (CSD). Les solutions respectives doivent respecter les conditions aux limites à l'interface fluide-structure. Ainsi, les communications de données à l'interface sont réalisées par un autre module nommé "matcher". Celui-ci permet le transfert des déplacements de la structure du solveur CSD au solveur CFD et l'effort aérodynamique du solveur CFD au solveur CSD. Cette tâche peut être compliquée si les maillages des deux domaines ne coïncident pas. Il est, en général, impossible de transférer l'information noeud à noeud entre les deux solveurs indépendants qui possèdent des maillages incompatibles, car les tailles et les types d'éléments de ces maillages sont différents. Par exemple, le maillage du solveur CFD est plus fin que celui du solveur CSD pour capturer le choc. Et surtout, dans le cas d'une structure mince qui est souvent dis-

crétisée par des éléments de coque, il n'y a pas de noeuds sur la paroi de la structure et donc il n'existe pas de contact direct entre les deux plans où se trouvent les noeuds du fluide et de la structure. L'écart entre ces deux plans est supposé constant, puisque la loi de contraintes planes est appliquée et il est supposé qu'il n'y a pas de déformation dans la direction d'épaisseur pour des structures minces. En outre, le transfert de données doit satisfaire les lois physiques de conservation.

L'aéroélasticité est aussi caractérisée par les frontières mobiles du domaine du fluide. Le maillage utilisé en description Euler n'est pas adéquat. La description cinématique appliquée est la description Euler-Lagrange. Elle permet l'utilisation d'un domaine de calcul mobile. Une méthode de mouvement de maillage est utilisé afin de diffuser le mouvement de la frontière mobile à l'intérieur du domaine tout en évitant une grande distorsion des éléments. Le solveur du maillage calcule le déplacement et la vitesse de chaque noeud du fluide. Enfin, le couplage se réalise entre les solveurs CSD, CFD, le solveur du maillage et le module matcher. Tous les modèles des sous systèmes sont discrétisés en espace par la méthode des éléments finis. Le modèle de l'aéroélasticité nonlinéaire appliquée dans cette thèse se représente ci-après :

CSD modèle

$$\mathbf{M}^s\mathbf{u}^s_{,tt} + \mathbf{D}^s\mathbf{u}^s_{,t} + \mathbf{K}^s\mathbf{u}^s = \mathbf{F}^f$$

Mesh modèle

$$\mathbf{K}^m\mathbf{u}^m = \mathbf{F}$$

CFD modèle

$$\mathbf{M}^f\mathbf{U}^f_{,t} + \mathbf{K}^f(\mathbf{U}^f, \mathbf{w}^f)\mathbf{U}^f = \mathbf{F}^s$$

Matcher module

à l'interface fluide-structure

$$\mathbf{u}^s = \mathbf{u}^m$$

$$\mathbf{u}^s_{,t} = \mathbf{u}^m_{,t} = \mathbf{u}$$

$$\boldsymbol{\sigma}^s_{ij} \cdot \mathbf{n}^s = -p\mathbf{n}^s$$

où $\mathbf{U}$ est le vecteur des variables conservatives, $\mathbf{u}^s_{,tt}$, $\mathbf{u}^s_{,t}$ et $\mathbf{u}^s$ sont respectivement les vecteurs de l'accélération, de la vitesse et du déplacement de la structure, $\mathbf{u}$ est le vecteur de la vitesse du fluide, $\mathbf{w}$ est le vecteur de la vitesse du grille du fluide, $\mathbf{M}^s$, $\mathbf{D}^s$ et $\mathbf{K}^s$ sont respectivement les matrices de masse, d'amortissement et de rigidité de la structure, $\mathbf{K}^m$ est la matrice de la rigidité du maillage du fluide, $\mathbf{M}^f$ et $\mathbf{K}^f$ sont respectivement les matrices de masse et de rigidité du fluide, $\mathbf{F}^f$ et $\mathbf{F}^s$ sont respectivement les vecteurs de l'effort aérodynamique et de la source de la structure, $\mathbf{u}^m$ est le vecteur du déplacement nodal du fluide, $\mathbf{F}$ est le vecteur de solicitation qui représente les déplacements des frontières mobiles, $\boldsymbol{\sigma}^s_{ij}$ est la contrainte de la structure, $\mathbf{n}^s$ est le vecteur du normal unitaire à l'interface fluide-structure , p est la pression du fluide. Dans le modèle CSD, le vecteur d'effort externe correspond aux forces nodales à l'interface fluide-structure. Dans le modèle du maillage, les déplacements des noeuds à l'interface fluide-structure sont obtenus par le mouvement de la structure. Sur la frontière lointaine, les déplacements des noeuds sont imposés à zéro. Dans le module CFD, la vitesse du fluide normale à l'interface fluide-structure est égale à la vitesse normale de la structure. Sur la frontière lointaine, la vitesse est imposée à la vitesse de l'écoulement de l'entrée.

L'algorithme Newmark est utilisé pour la discrétisation en temps des équations d'élastodynamique. Un premier solveur nommé CSD-MAM est développé en appliquant la méthode d'analyse modale qui est compacte et économique pour un modèle linéaire. Dans un

autre solveur nommé CSD-FEM, les systèmes d'équations algébriques résultants de la discrétisation spatio-temporelle sont résolus à l'aide des méthodes itératives où l'algorithme GMRES avec un preconditioneur ILUT est implémenté. Pour le solveur CFD, la méthode d'élément fini stabilisée SUPG est adopté. Le schéma de couplage fluide-structure utilise l'algorithme itératif Gauss-Seidel. L'algorithme général se résume dans le processus suivant :

Algorithme du couplage Gauss-Seidel :

1. Allouer les tableaux de mémoires pour le module matcher, les solveurs CSD, CFD et le solveur du maillage.
2. Identifier les noeuds du fluide sur sa frontière mobile.
3. Identifier les éléments associés de la structure de chaque noeud du fluide sur l'interface fluide-structure par le module matcher.
4. Initialiser le solveur CFD, calculer la pression nodale sur la frontière mobile du fluide et projeter cette pression sur son élément structurel associé.
5. Initialiser le déplacement et la vitesse nodale de la structure à zéro et calculer l'accélération nodale à partir du déplacement initial, de la vitesse initiale et de la force externe.
6. Boucle de temps dans le solveur CFD jusqu'à l'étape 16.
7. Appliquer une perturbation structurelle ou une force distribuée sur la structure pendant le premier pas de calcul.
8. Boucle itérative de couplage jusqu'à l'étape 15.
9. Appeler le matcher module pour effectuer la projection de pression et calculer le déplacement structurel en appelant le solveur CSD.
10. Calculer le déplacement nodal du fluide sur sa frontière mobile.
11. Appeler le solveur du maillage pour calculer les déplacements nodals du fluide dans son domaine entier.
12. Mise à jour des coordonnées des noeuds du fluide et calculer la vitesse de la grille du fluide.

13. Mise à jour de la normale de chaque élément du fluide sur sa frontière mobile et calculer la vitesse nodale sur cette frontière.
14. Utiliser GMRES préconditioné par ILUT dans le calcul du solveur CFD et calculer la pression nodale aérodynamique.
15. Fin de boucle d'itération de couplage.
16. Fin de boucle de temps.
17. Fin de calcul.

Le processus du couplage est appliqué pour la simulation de flottement. À l'étape 7, le système de l'aéroélasticité reçoit une perturbation sur la structure au premier pas de temps de calcul. L'oscillation du système aéroélastique est déclenchée. L'analyse de la stabilité se fait par l'observation de la réponse autour de la solution initiale. Cependant, si la réponse est une oscillation avec une amplitude croissante, le système est considéré instable.

La validation du code global de l'aéroélasticité nonlinéaire commence par une validation rigoureuse de tous ses modules. D'abord les deux modules CSD-MAM et CSD-FEM sont comparés. La différence entre les résultats obtenus par ces deux solveurs n'est pas significative lorsque la réponse est dominée par les premiers modes. Par la suite, le couplage est effectué entre le solveur CSD, le solveur du maillage et le module matcher sans intervention du solveur CFD. Une force de forme Dirac est appliquée sur un point de la structure pendant le premier pas du calcul. Le code est capable de diffuser le mouvement de la frontière du fluide dans le domaine entier du fluide sans avoir des distorsions trop grandes des éléments. Finalement, le couplage complet entre les solveurs CFD, CSD, le solveur du maillage et le module matcher est validé sur l'aile aéroélastique AGARD 445.6. D'abord, une solution est obtenue par le solveur CFD en considérant que la structure est rigide. Cette solution est prise comme une solution initiale pour déclencher la simulation du flottement de l'aile. A partir de ce moment, une force de forme Dirac est appliquée sur un point du bout d'aile. L'oscillation du mouvement de l'aile est déclenchée. Les

simulations donnent des résultats satisfaisants en comparaison avec ceux expérimentaux. Une analyse du phénomène de flottement est effectué dans le cas où le nombre de Mach est à 0.96. Dans ces conditions, la valeur critique de la pression dynamique est minimale et sa valeur expérimentale est à 61.3 $lb/sqft$. Les différentes simulations effectuées sur un maillage relativement grossier montrent une valeur de pression dynamique critique à 60.0 $lb/sqft$ qui est un résultat acceptable vue le maillage utilisé.

Cette thèse à permis de contribuer à :

- Développer deux codes de calcul de structures en élasto-dynamique : un basé sur la méthode d'analyse modale (CSD-MAM) et un autre basé directement sur la méthode des éléments finis (CSD-FEM).
- Développer un solveur du maillage pour assurer que le mouvement du maillage du fluide suit bien le mouvement de la structure à l'interface fluide-structure.
- Développer un module pour effectuer l'échange des informations à l'interface fluide-structure : transfert de l'effort aérodynamique du fluide vers la structure et celui du mouvement de la structure vers le fluide.
- Adapter le solveur fluide CFD pour tenir compte du mouvement du maillage. Le solveur CFD solver a déjà été développé et validé par le laboratoire GRANIT.
- Réaliser le couplage complet des tous les modules. Pour ce faire, un algorithme itératif de type Bloc-Gauss-Seidel-nonlinéaire est utilisé.
- Valider le code de l'aéroélasticité nonlinéaire en l'appliquant au cas test expérimental de l'aile aéroélastique AGARD 445.6.

ACKNOWLEDGEMENTS

I would like to give my most sincere acknowledgements to my supervisor Dr. Azzeddine Soulaïmani, Professor of Mechanical Engineering at École de Téchnologie Supérieure Montréal, for providing me the great opportunity of doing this research and for his financial and moral support. I would like to express my deepest gratitude for his guidance and advice. The benefits from his remarkable creativity, profound insight, wide vision, inspirational leadership and experiences will remain as a rich source in my professional life.

I wish to thank Dr. Christian Masson, Professor at École de Téchnologie Supérieure Montréal, for presiding over the committee of the qualification and the evaluation of this thesis and for his critique. I am grateful to Dr. Van Ngan Le, Professor at École de Téchnologie Supérieure Montréal and Dr. Stuart J. Price, Professor at Mcgill University for accepting to be members of the same committee, for their critique and for having taught me with excellent pedagogical skills in their courses.

Grateful thanks go to École de Téchnologie Supérieure and Pratt & Whitney Canada for additional financial support. Thanks also go to Bombardier Aerospace and National Science and Engineering Research Council of Canada for funding this research.

Special thanks go to the members of the research group GRANIT for their help and encouragement and to Emmanuel Lorin, maître de Conference en Mathématiques à l'Université

Paris XI (Orsay) for the comments on this thesis. Thanks to Mrs. Devaki C. Groulx, Professor at Mcgill University for the English correction.

I would like to express my special gratitude to my parents, my brother, my sisters and their families who have always supported and encouraged me. Thanks go to all my friends who have helped me along the way.

CONTENTS

LIST OF TABLES

Page

LIST OF FIGURES

Page

LIST OF ABBREVIATIONS AND NOTATIONS

Abbreviations

AC	Aerodynamic center
CG	Gravity center
$CSD-MAM$	Computational Structural Dynamics with Modal Analysis Method
$CSD-FEM$	Computational Structural Dynamics with Finite Element Method
EA	Elastic axis
$GMRES$	Generalized Minimal RESidual
$ILUT$	Incomplete LU Decomposition with Threshold
MC	Mass center

English symbols

a	Sound speed
a_∞	Sound speed of oncoming flow
A_1, A_2	Aerodynamic operators for lift and moment
$\mathbf{a}_1, \mathbf{a}_2$	Covariant base vectors
$\mathbf{a}^1, \mathbf{a}^2$	Dual vectors of $\mathbf{a}_1$, $\mathbf{a}_2$
b	Semi-chord of wing section
bx_a	Distance between the elastic axis and the center of gravity
$\mathbf{b}$	Physical quantity per unit mass in a control volume
c	Chord of a wing section
C_p	Constant pressure specific heat
C_v	Constant volume specific heat
d_z	Structural damping of deflection

d_θ	Structural damping of torsion
$\mathbf{D}$	Structural damping matrix
$\bar{\mathbf{D}}$	Aeroelastic damping matrix
$\bar{\mathbf{D}}_s$	Symmetrical component of the unsymmetrical matrix $\bar{\mathbf{D}}$
e	Internal energy or index for elements
E	Elastic modulus of isotropic material
$\bar{\mathbf{E}}$	Aeroelastic stiffness matrix
f	Index to fluid
$\mathbf{f}_s$	Surface force vector
$\mathbf{f}_v$	Volume force vector
$\mathbf{F}_0$	Static load vector
$\mathbf{F}_{aero}$	Aerodynamic load vector
$\mathbf{F}_A$	Concentrating force at point A
$\mathbf{F}(t)$	External nodal concentrating force vector
$\mathbf{F}_\zeta$	Matrix of vectors of covariant base
$\mathbf{g}$	Acceleration of gravity
$\mathbf{G}$	Matrix of behavior of shear stress
h	Element characteristic size
$\mathbf{H}_t, \mathbf{H}$	Matrices of elastic behavior
$\mathbf{i}, \mathbf{j}, \mathbf{k}$	Orthogonal cartesian base
I	Moment of inertia
$\mathbf{I}$	Unit diagonal matrix
J	Geometric Jacobian transform coefficient
k	Heat conductivity
k_z	Linear spring coefficient

k_θ	Torsional spring coefficient
$\mathbf{K}$	Structural stiffness matrix
L	Aerodynamic lift
$\mathbf{L}_\zeta$	Gradients of displacement
m	Mass
M	Mach number
M_∞	Mach number of oncoming flow
M_{ea}	Aerodynamic moment around the elastic axis
$\mathbf{M}$	Structural mass matrix
n	Total number of element
$\mathbf{n}$	Unit normal vector
N	Shape function
p	Pressure
$\mathbf{p}_0$	Eigenvector of a system without damping
q	Dynamic pressure or heat flux
$\mathbf{Q}, \mathbf{Q}_\zeta$	Orthogonal transform matrices
$\mathbf{Q}^T$	Transpose matrix of $\mathbf{Q}$
R	Air constant
s	Index to structure
S_t	Boundary of control volume at instant t
$\mathbf{s}_0(t)$	External modal excitation
$\bar{\mathbf{S}}_k$	Skew-symmetrical component of the unsymmetrical matrix $\mathbf{D}$
t	Time
$\mathbf{t}_1, \mathbf{t}_2, \mathbf{n}$	Orthogonal base at point p
$\mathbf{t}_{1\zeta}, \mathbf{t}_{2\zeta}, \mathbf{n}_\zeta$	Orthogonal base at point q

T	Temperature
$\mathbf{T}$	Coordinates transform matrix
$\mathbf{U}$	Conservative variables
u	Air speed in the flow direction
u', v'	Small perturbation of velocities u, v
$\mathbf{u}^f$	Fluid nodal displacement vector
$\mathbf{u}^s$	Structural nodal displacement vector
$\mathbf{u}^*_{p_A}$	Displacement vector of node p_A
$\mathbf{u}^*_q$	Virtual displacement vector of point q
u_∞	Velocity of the oncoming flow
v	Air speed in the flow transversal direction
$\mathbf{V}$	Velocity of flow
$\mathbf{w}$	Grid velocity
$\dot{W}$	Rate of work on the structure in one oscillating period
W_c	Internal work due to shear stress.
W^e_c	Elementary internal work due to shear stress
W_{ext}	External virtual work
W_{int}	Internal virtual work
W^e_{mf}	Elementary internal work due to flection
$\mathbf{W}$	Weighting functions
$\mathbf{x}_p$	Position vector of point p
$d\mathbf{x}_p$	Position differential vector of point p
$\mathbf{x}_q$	Position vector of point q
$d\mathbf{x}_q$	Position differential vector of point q
X, Y, Z	Global cartesian coordinates

$X_{,\xi}, Y_{,\xi}, Z_{,\xi}$	Partial derivatives of X, Y and Z in ξ direction
$X_{,\eta}, Y_{,\eta}, Z_{,\eta}$	Partial derivatives of X, Y and Z in η direction
z	Vertical displacement
$\dot{z}$	Vertical velocity
$\ddot{z}$	Vertical acceleration
$\mathbf{z}(t)$	Generalized modal coordinate vector

Greek symbols

β_1^*	Rotation of vector $\mathbf{n}$ in $(\mathbf{n}, \mathbf{t}_1)$ plane
β_2^*	Rotation of vector $\mathbf{n}$ in $(\mathbf{n}, \mathbf{t}_2)$ plane
$\boldsymbol{\gamma}_s^*, \boldsymbol{\gamma}_\alpha^*$	Shear strain at point p
$\gamma_{xy}^*, \gamma_{yz}^*$	Shear strain at point q
θ	Torsional displacement
$\dot{\theta}$	Torsional velocity
$\ddot{\theta}$	Torsional acceleration
λ	Second viscosity coefficient
μ	First viscosity coefficient
γ	Specific hear ratio
Γ_1	Fluid moving boundary.
ε	Small scale
$\boldsymbol{\varepsilon}$	Strain tensor
ξ, η, ζ	Independent curvilinear coordinates
ρ	density
$\boldsymbol{\sigma}_x, \boldsymbol{\sigma}_{xy}, \boldsymbol{\sigma}_{xz'}, \boldsymbol{\sigma}_y, \boldsymbol{\sigma}_{yz'}$	Curvilinear components of stress
$\boldsymbol{\sigma}_f$	Fluid stress

$\boldsymbol{\sigma}_s$	Structural stress
ν	Poisson coefficient of isotropic material
ϕ	Velocity potential
$\boldsymbol{\phi_n}$	Numerical aerodynamic load flux
ω	Frequency
ω_0	Frequency of a system without damping
Ω_t	Domain of control volume at instant t
$\boldsymbol{\omega}$	Flow vorticity

INTRODUCTION

Aircrafts with more performance and safety are required to satisfy strong competition among airline companies, which make tremendous effort to attract customers with a safe, comfortable environment and less expensive services. In fact, customers' requirements always lead to new technological advances. Recently, the demand for faster airplanes has led to the construction of transonic airplanes at Mach number close to unity. In general, the challenge is to build stable and large wings with optimal design, which operate in transonic regime at a higher Mach number to satisfy these requirements. However, a large wing makes the structure more flexible and its operation in transonic regime yields complex phenomena, such as shock formation, moving shock waves and flow induced vibrations [1,2].

A flexible structure in airflow yields a two-way fluid-structure interaction. The structural motion induced by the aerodynamic loads alters the configuration of the fluid domain, which in turn, alters the aerodynamic loads on the structure. Aeroelasticity is a particular case of fluid-structure interaction, where the fluid is air. Instability is a substantial issue in aeroelasticity : a small perturbation from the operating point, such as manoeuvre of control surface of a wing or a small change of the oncoming wind, will produce an oscillation of structural motion. This oscillation decays and finally disappears completely if the system is dynamically stable. For an unstable system, the oscillation will increase until structural failure occurs. This phenomenon is known as flutter. The critical one between the two precedent cases, where the oscillation keeps a constant amplitude, is called critical flutter and the flow speed at this point is known as the flutter speed.

Aeroelasticity in transonic regime is complex due to its nonlinearity. In the early days, commercial aircrafts operated at low Mach numbers, such as in low subsonic regime, where linear models were accurate enough to describe aerodynamics. Aeroelastic analysis in this regime became relatively simple. As the Mach number increases from a lower

value to a higher value, particularly to a value close to unity, strong shock waves dominate aeroelastic behavior. Linear aeroelastic theory is not able to give accurate flutter predictions and nonlinear aeroelasticity must be applied.

Analysis of nonlinearity for large transonic aircraft wings can be performed with wind tunnel testing and numerical simulations. However, some limitations, such as time consumption and testing costs, exist in the wind tunnel testing as the dimension of a wing increases [3, 4]. Numerical simulations have much more advantage than the wind tunnel testing. A computer or a cluster of computers cost less than a wind tunnel system. The cost of a numerical simulation is also much less than that of a wind tunnel testing. Numerical simulation which offers a way to partially replace the wind tunnel testing is able to give results much more quickly. Certainly, a mature computational code must be validated by the wind tunnel testing. Such validated computational software is able to guide the wind tunnel testing in order to minimize the costs during aircraft design.

Although numerical simulation has many advantages, it was impossible to simulate complex nonlinear aeroelastic systems when the computer technology was less developed. Recently remarkable growth in the supercomputer technology has made complex computations available in the aeroelasticity research as in other domains. The processors speed and the memory capacity increase quickly. Other strategies, such as parallel computations [5, 6], have been investigated. These advantages of the computer technologies are of great benefit to the research of computational aeroelasticity, which is complex and multidisciplinary.

This thesis begins with this general introduction in the current chapter. In Chapter 1, a discussion of the background according to the literature will be presented. Then a general presentation of the methodology for aeroelasticity models will be stated. Chapter 2 deals with the theories on which our nonlinear aeroelasticity models are based. First, the linear structural dynamic model based on the shell structure theories will be presented. Sec-

ondly, linear and nonlinear aerodynamics models will be discussed. A linear mesh model based on the fictitious elasticity is then presented. Thereafter, the boundary conditions on the fluid-structure interface will be discussed. Chapter 3 deals with the description of the solvers of the subsystems presented in the precedent chapter. These solvers are described by the governing equations under discrete forms in space by the finite element method and in time by the finite difference method for the CFD (Computational fluid Dynamics), the CSD (Computational Structural Dynamics) and the mesh solvers. The matcher module presents the "pairing" between the fluid points and the structural elements, the surface tracking and the aerodynamic loads projection. In Chapter 4, the CFD-based coupling algorithm of the nonlinear computational aeroelasticity solver will be presented. In Chapter 5, numerical experiments of the validation of the CSD solvers, the matcher module and the mesh solver will be presented. Then numerical simulation results of nonlinear aeroelasticity applied to the AGARD 446.5 aeroelastic wing will be presented. Finally, concluding remarks will be drawn.

CHAPTER 1

NONLINEAR COMPUTATIONAL AEROELASTICITY

Aeroelasticity of aircraft wings is described by the mutual interaction between aerodynamics and structural dynamics. Aeroelasticity models are based on physic hypotheses. When flight speed is in subsonic regime, the hypotheses of linear theories can be applied. However, as flight speed increases, the linear aeroelasticity theories become inaccurate in calculating the dynamic responses of aircrafts in transonic flow. The models must be refined to describe complex aeroelastic phenomena. In this chapter a literature review will be presented and the objective of this thesis will be stated. Then, its problematic will be described in detail. Finally, a general presentation of the methodology will be introduced.

1.1 Background

In classical aeroelastic theories where Mach number is less than about 0.7, aerodynamic loads (lift and moment) are assumed to be linear functions of a structural motion (displacement, velocity and acceleration) and vice versa. According to this hypothesis, the aeroelasticity analysis results in linear equations [1, 7, 8]. Although aerodynamic theory in such aeroelasticity analysis is based on the Navier-Stokes equations which describe completely aerodynamic behaviors, more hypotheses were used for the purpose of simplification. Indeed, at low Mach number, airflow is considered inviscid and incompressible [9]. Moreover, the flow is assumed irrotational [10, 11]. These hypotheses lead to the linear potential equation of the classical aerodynamics where solutions can be obtained simply by linear superposition. For example, the most well-known Doublet Lattice method [12, 13] is widely applied in the linear aeroelastic analyses [14–16]. The commercial software MSC/NASTRAN is based on this method [17]. Other methods are developed and applied in computational aerodynamics using linear potential flow theory, such as the

Vortex-Lattice method [18–20] and the panel method [21–25]. As the Mach number of the oncoming flow increases to more than about 0.7, airflow is characterized by a transonic flow, where the flow becomes supersonic in some regions even though the Mach number of oncoming flow is still less than unity. The linear aerodynamic theories are no longer available since the flow can not be assumed incompressible [26]. A transonic dip [27–33] occurs in the flutter boundary which is unable to be captured by subsonic linear unsteady aerodynamic theories. This gradual dropping of flutter speed from the subsonic regime to a minimum in the transonic regime and then a rapid rising towards the supersonic regime is produced by complex transonic phenomena, such as the shock formation and the shock wave motion. In fact, the shock is the cause of the nonlinearity of a transonic flow which is not able to be captured by the linear aerodynamic theory [34]. Nonlinear aeroelasticity theories must be introduced to overcome this difficulty. The transonic small disturbance (TSD) equation method [28, 29, 34, 35] based on the full potential equation had been developed to obtain useful solutions when the computing technology was still less advanced. The flow is linearized around the free stream by assuming a small disturbance away from the free stream. In fact, the governing equations are dominated by nonlinearity which presents shock phenomena. The full potential equation which presents more completely the nonlinearity of a transonic flow gives improved solutions [36,37]. However, the flow is still assumed irrotational in both of the above methods. The accuracy is not affected when the shock is weak. For the purpose of capturing strong shocks, the Euler equations which represents rotational compressible flows are able to describe more accurately the nonlinearity of transonic flows [28, 38]. Certainly, calculations based on the Euler equations were not fast enough in the early days because of the limitation of the computer technology. However, the recent increase in computer speed and the improved algorithms for the numerical solutions of aerodynamics lead to a more accurate computation of aerodynamic loads in computational aeroelasticity with increasing geometrical complexity [39].

As the aeroelasticity model based on the Euler equations [40, 41] has relatively high computational loads, the complete three-dimensional aeroelastic problem of transonic flow is difficult to analyze because it has mixed linear and non-linear operators, symmetric and asymmetric matrices, explicit and implicit coupling, and can become physically unstable [42]. Although the direct method [43], where the fluid and the structural governing equations are combined and treated as a single monolithic system of equations, has advantages on algorithm stability and accuracy, it is impractical to rewrite a completely new code for solving a complex aeroelastic system [44–46]. In fact, computational aeroelasticity which is characterized by multiphysics is a particular case of fluid-structure interaction [47]. Its evolution is always accompanied by those of the CFD and CSD models which have different mathematical and numerical properties [2, 46]. Fluid dynamics is dominated by the Navier-Stokes/Euler equations while structural dynamics is dominated by the elasto-dynamics equations. Traditionally, due to the computation complexity and computer technology limitations, a complete aeroelasticity system was analyzed using CFD and CSD software separately by different working groups and then using data communication between them. Such loosely coupled strategy becomes less effective for large structures with higher computational accuracy. The tight coupling strategy replaces the separating working groups through the CSD and CFD solvers and uses an information transfer module for the communication between them [48]. This strategy facilitates the development of the complete software by developing CSD and CFD codes separately. The most interesting feature of this coupling strategy is the reutilization of the existing well-established CSD and CFD codes [49].

The strategy to segregate a complete computational aeroelastic model into a CSD model and a CFD model has much advantage in the software development. However, two problems should be solved : one is the time-varying fluid domain due to the moving fluid boundary which follows the structural motion, another one is the problem of non-matching between the fluid and the structural grids on the fluid-structure interface [50, 51].

The change of the flow configuration caused by the structural motion yields limitation to apply the same spatial discretization for a complete computational aeroelasticity model. As the fluid-structure interface is in motion, the flow configuration is a time function [52]. The space near the fluid-structure interface will belong to a part of the fluid domain in one instant and another part of the structure domain in another instant. The fluid mesh should be repaired during the computation. The zonal grid technique [53] and the local remeshing [54] are techniques to avoid excessive element distortions of the fluid mesh near the moving structure. Another technique uses the interpolation of the speeds of the far-field boundaries and the moving fluid boundary to update the fluid grid speed [37]. In order to avoid strong distortions of the fluid mesh near the structure, an effective adaptive moving mesh is necessary. The Arbitrary-Eulerian-Lagrangian kinematic description [55, 56] which is generally applied in fluid-structure interaction [57] has the most interest. This method which is improved for numerical simulations with moving boundaries [58] is popular for adaptive moving meshes. As a result, the coupling becomes CFD-CSD-mesh coupling after another solver known as the "mesh solver" has been added to adapt to the moving fluid boundaries [59].

An information transfer module is required to establish the communication between the CSD and the CFD codes due to the non-matching of the fluid and the structural grids on the fluid-structure interface [60]. Because these two codes are independent, the structural mesh and the fluid mesh are not necessarily compatible. Furthermore, they may have different element types. Even if they have the same element types, the fluid element size is always smaller than the structural element size for specific purposes of computations [45, 61, 62]. It is required to transfer the displacement of the structural boundary nodes to the fluid boundary nodes and the aerodynamic loads of the fluid boundary nodes to the structural boundary nodes. For the sake of computational accuracy, the information transfer must satisfy conservation of energy [47, 63–66]. This information transfer is simple if the fluid spatial discretizing points coincide with structural discretizing points at the

fluid structure interface (same type and size for both CFD and CSD solvers). But usually, it is complex due to the non-matching of the two space discretizations at the fluid-structure interface. A special module known as matcher must be built for the purpose of information transfer on this interface [51].

Using a modular approach makes a modification of any solver and its reutilization easier [59]. Two approaches are possible to couple the three-field computational disciplines. One is the loose coupling [49] which has a convergence problem [67]. Another one is the tight coupling which has properties of numerical stability and accuracy close to the direct method.

The transonic aeroelasticity with Mach number close to unity with a low angle of attack is one key area of the aeroelasticity analysis [27]. The goal of this thesis is to provide contributions in developing a comprehensive software of computations of nonlinear aeroelasticity using coupling strategy with an application of a robust CFD solver [59, 61, 69, 87, 97, 100]. This CFD-based software will be able to provide accurate flutter predictions.

1.2 Problematic and Methodology

Aeroelasticity is the study of the interaction between inertial, elastic and aerodynamic forces. "The structural flexibility of the body and the interaction of this flexibility with the aerodynamic forces is the whole essence of aeroelasticity [70]."

Structural flexibility is the source of aeroelasticity. If an airflow passes over a rigid structure, such as a wall, aeroelasticity does not exist. However, as an airflow passes over a thin flexible structure, such as a modern aircraft wing, the structural motion can not be neglected. A simple example of aeroelasticity is a typical section of an airfoil in an airflow as shown in Figure 1. This airfoil section with chord c, semi-chord b, mass m and moment of inertia I is flexibly mounted on its elastic axis via a linear spring k_z and a torsional spring

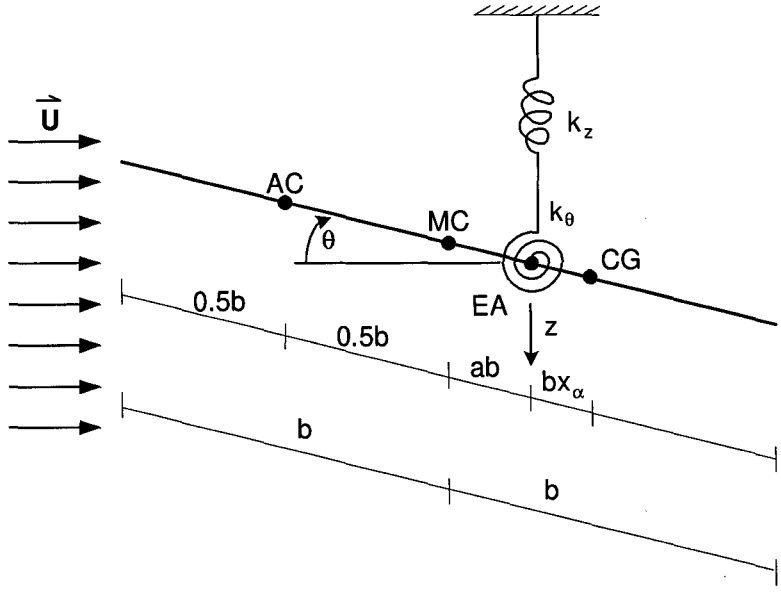

Figure 1 A typical section of airfoil in airflow

k_θ. AC, MC, EA and CG are respectively the aerodynamic center, the mass center, the elastic axis and the gravity center. The system is assumed to have the following two degrees of freedom : the vertical motion z and the torsional motion θ. Using Lagrange's equation yields the following equations of motion :

$$\begin{bmatrix} m & mbx_a \\ mbx_a & I + mb^2x_\alpha^2 \end{bmatrix} \begin{Bmatrix} \ddot{z} \\ \ddot{\theta} \end{Bmatrix} + \begin{bmatrix} k_z & 0 \\ 0 & k_\theta \end{bmatrix} \begin{Bmatrix} z \\ \theta \end{Bmatrix} = \begin{Bmatrix} -L \\ M_{ea} \end{Bmatrix} \tag{1.1}$$

where bx_α is the distance between the elastic axis and the gravity center, L is the aerodynamic lift and M_{ea} is the aerodynamic moment around the elastic axis. The right hand side of these equations represents the aerodynamic loads which are functions of the structural

motion. L and M_{ea} can be described by the following two expressions :

$$L = A_1(q, z, \theta, \dot{z}, \dot{\theta}, \ddot{z}, \ddot{\theta}) \tag{1.2}$$

$$M_{ea} = A_2(q, z, \theta, \dot{z}, \dot{\theta}, \ddot{z}, \ddot{\theta}) \tag{1.3}$$

where A_1 and A_2 are aerodynamic operators for the lift and moment. They may be linear or nonlinear. $z, \dot{z}, \ddot{z}, \theta, \dot{\theta}, \ddot{\theta}$ are respectively the vertical displacement, velocity, acceleration and the torsional displacement, velocity, acceleration. q is the free steam dynamic pressure given by the following equation :

$$q = \frac{\rho u^2}{2}$$

where u is the component of the local flow velocity which is perpendicular to the lift. In general, the equations of the structural motion contain the following structural damping matrix :

$$\mathbf{D} = \begin{bmatrix} d_z & 0 \\ 0 & d_\theta \end{bmatrix}$$

where d_z is the structural deflection damping and d_θ the structural torsion damping. Adding the structural damping into equations (1.1) yields the following system :

$$\mathbf{M}\ddot{\mathbf{p}} + \mathbf{D}\dot{\mathbf{p}} + \mathbf{E}\mathbf{p} = \mathbf{F}_{aero} \tag{1.4}$$

with

$$\mathbf{p} = \begin{Bmatrix} z \\ \theta \end{Bmatrix}$$

and

$$\mathbf{F}_{aero} = \left\{ \begin{array}{c} -L \\ M_{ea} \end{array} \right\}$$

where $\mathbf{p}$ is the structural displacement vector; $\mathbf{M}$, $\mathbf{D}$, $\mathbf{E}$ denote respectively the structural inertial, damping and stiffness matrices; $\mathbf{F}_{aero}$ is the aerodynamic loads vector whose entries are functions of the structural motion and the aerodynamic pressure.

In the classical elastic analysis as shown in the following equations, the right hand side of equations (1.4) is presented by the prescribed loads $\mathbf{F}$:

$$\mathbf{M}\ddot{\mathbf{p}} + \mathbf{D}\dot{\mathbf{p}} + \mathbf{E}\mathbf{p} = \mathbf{F} \tag{1.5}$$

The stability of such a system is determined by the structural mass, damping and stiffness matrices. However, for an aeroelasticity system, the aerodynamic loads $\mathbf{F}_{aero}$ on the right hand side of equations (1.4) are functions of the dynamic pressure, the structural displacement, velocity and acceleration as expressed in equations (1.2) and (1.3). A stable structural dynamic system described by equations (1.5) of a classical elastic system may become an unstable system described by equations (1.4) of an aeroelastic system if an airflow passes over the structure. Using quasi-steady linearized aerodynamic theory, equations (1.2) and (1.3) will yield linear relation with the structural displacement, velocity and acceleration. The aerodynamic loads can be written as below if the effect of structural acceleration is neglected [70] :

$$\mathbf{F}_{aero} = \mathbf{F}_0 - q(\mathbf{K}\mathbf{p} + \mathbf{B}\dot{\mathbf{p}}) \tag{1.6}$$

where $\mathbf{F}_0$ is the static loads vector, which defines the equilibrium position. $\mathbf{K}$ and $\mathbf{B}$ are respectively the aerodynamic stiffness matrix and the aerodynamic damping matrix. They

are independent of the structural motion. The second term on the right hand side of the above equations represents the aerodynamic loads vector which depends on the structural motion. Combining the structural and the aerodynamic damping and stiffness yields :

$$\mathbf{M}\ddot{\mathbf{p}} + \bar{\mathbf{D}}\dot{\mathbf{p}} + \bar{\mathbf{E}}\mathbf{p} = \mathbf{F}_0 \tag{1.7}$$

with

$$\bar{\mathbf{D}} = \mathbf{D} + q\mathbf{B}$$

$$\bar{\mathbf{E}} = \mathbf{E} + q\mathbf{K}$$

where $\bar{\mathbf{D}}$ is the aeroelastic damping matrix combining the structural damping with the aerodynamic damping, $\bar{\mathbf{E}}$ is the aeroelastic stiffness matrix combining the structural stiffness with the aerodynamic stiffness. These matrices which are functions of the dynamic pressure q determine the stability of the aeroelastic system. They can become negative definite matrices if the dynamic pressure is too strong.

Suppose that the static loads are harmonic functions, such as $\mathbf{F}_0 = \mathbf{A}\sin\omega t$, the oscillating response of the structural displacements has the following form :

$$\mathbf{p} = \mathbf{a}\sin\omega t + \mathbf{b}\cos\omega t$$

The rate of work $\dot{W}$ on the structure in one period can be described as [70] :

$$\frac{\dot{W}}{\pi} = \begin{bmatrix} \mathbf{a}^t & \mathbf{b}^t \end{bmatrix} \begin{bmatrix} \omega\bar{\mathbf{D}}_s & -\bar{\mathbf{S}}_k \\ -\bar{\mathbf{S}}_k & \omega\bar{\mathbf{D}}_s \end{bmatrix} \begin{bmatrix} \mathbf{a} \\ \mathbf{b} \end{bmatrix} = \begin{bmatrix} \mathbf{a}^t & \mathbf{b}^t \end{bmatrix} [G] \begin{bmatrix} \mathbf{a} \\ \mathbf{b} \end{bmatrix}$$

where $\bar{\mathbf{D}}_s$ is the symmetrical part of $\bar{\mathbf{D}}$, $\bar{\mathbf{S}}_k$ is the skew-symmetrical component of $\bar{\mathbf{S}} = \bar{\mathbf{E}} - \omega^2\mathbf{M}$. The stability of the system is influenced by aerodynamic loads since $\mathbf{G}$ depends

on the dynamic pressure q. If $\mathbf{G}$ is a positive definite matrix, $\dot{W}$ is positive, the system is stable. The airflow absorbs energy produced by the structure. Otherwise, the airflow feeds energy to the structure and the oscillation of the structural motion increases. As a result, the system becomes unstable [42].

In the frequency analysis, the matrices $\mathbf{M}, \bar{\mathbf{D}}, \bar{\mathbf{E}}$ determine the eigenvalues of the system, which can have real or complex values. If the real parts of the eigenvalues are negative, the system is stable. Otherwise, it is unstable. For a step perturbation of $\mathbf{F}_0$, there are five possible responses of the structural motion as shown in Figure 2. In the first case, all of the eigenvalues are negative reals, therefore, the response decays and finally the system returns to its equilibrium position. Hence the system is stable. In the second case, some of the eigenvalues are complex eigenvalues, but the real parts of all complex eigenvalues are negative. The system has an oscillating response, which decays and finally the system returns to its equilibrium position as well, so the system is also stable. The third case is similar to the second case except that with at least one complex eigenvalue with zero real part, the response yields neutral oscillation. The system is in a critical stability. In the fourth case, all of the eigenvalues are real, but at least one eigenvalue is positive, therefore, the response increases exponentially. The system is unstable (divergence). In the fifth case, some of the eigenvalues are complex, but at least one real eigenvalue is positive or at least one complex eigenvalue has positive real part. The system has oscillating response, which will increase exponentially. Therefore, the system is also unstable (flutter).

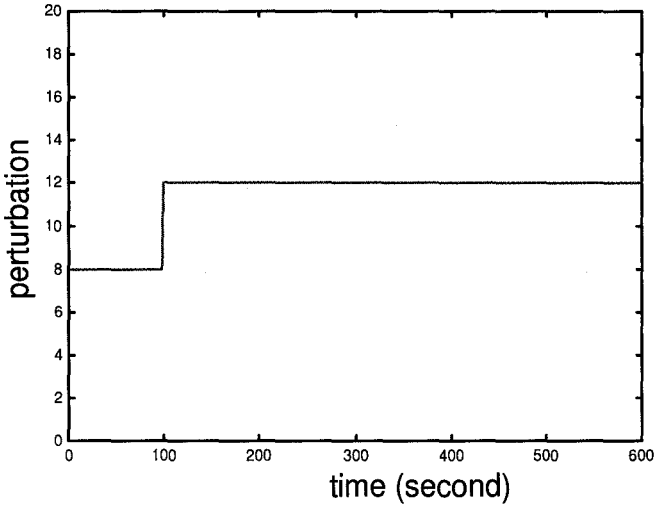

Step input perturbation

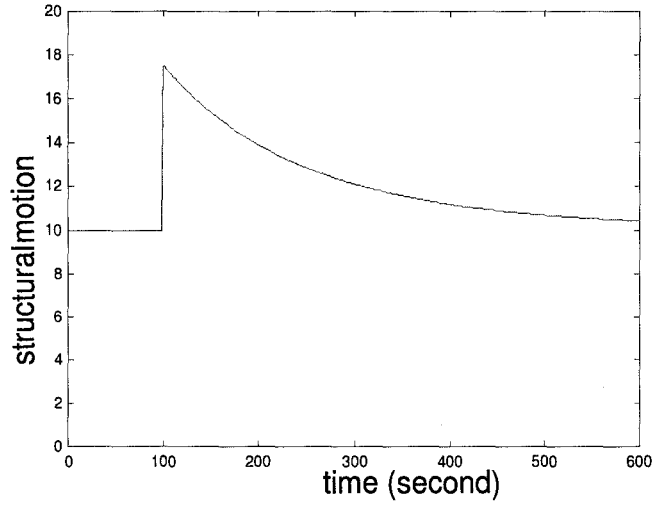

Case 1 Stable response without oscillation

Figure 2 Stable and unstable responses of a structural motion

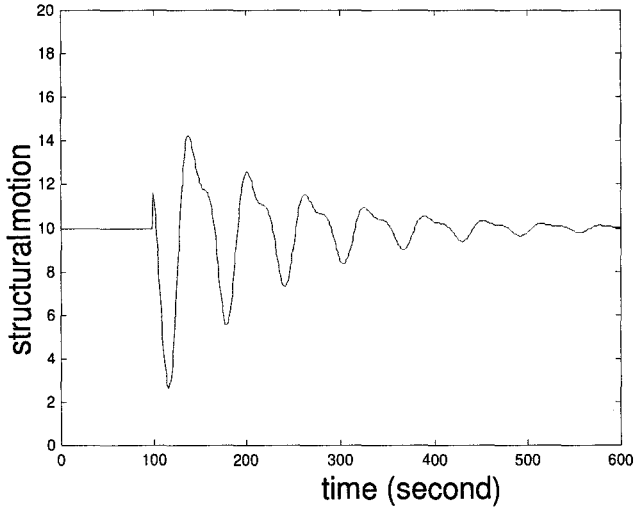

Case 2 Stable response with oscillation

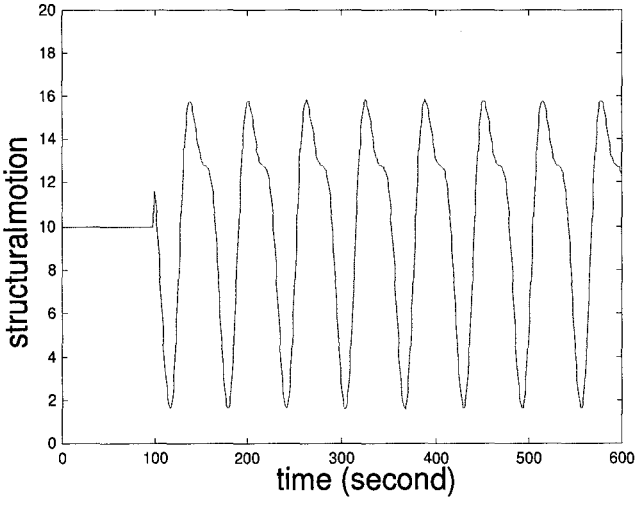

Case 3 Critical flutter

Figure 2 Stable and unstable responses of a structural motion (continued)

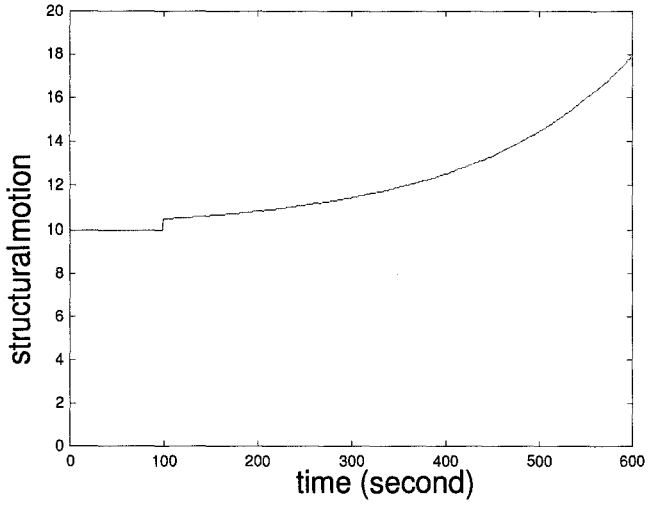

Case 4 Divergence

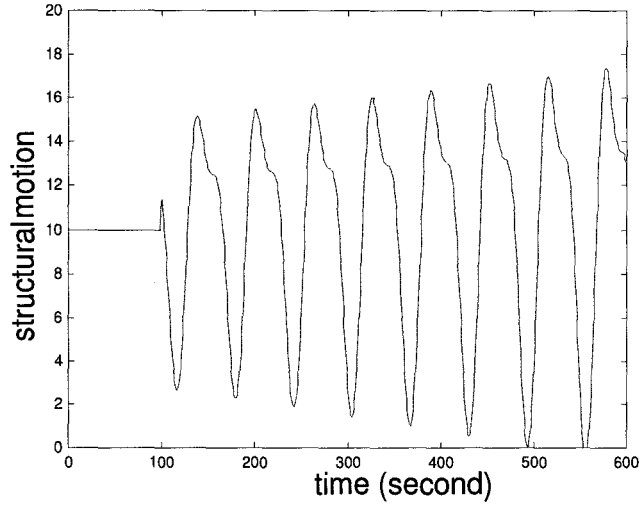

Case 5 Flutter

Figure 2 Stable and unstable responses of a structural motion (continued)

The relation between the inertial, the elastic and the aerodynamic forces of a typical section of an airfoil is expressed by equations (1.4) using linearized quasi-steady aerodynamics. However, in the case of a three-dimensional flexible wing in a transonic flight regime,

the aerodynamic forces can not be expressed by equations (1.6). Because of nonlinear effects, it is difficult or impossible to get a set of governing equations similar to equations (1.7) by applying the quasi-steady aerodynamics theory. Unsteady aerodynamics is suggested to get an accurate solution. The equations of nonlinear aeroelasticity based on the fluid-structure interaction is described by equations (1.4). The nonlinear aerodynamic load vector $\mathbf{F}_{aero}$ can be obtained by the CFD solver. The accurate solution strategies of these equations by nonlinear computational aeroelasticity will be discussed in detail in the following chapters.

CHAPTER 2

GOVERNING EQUATIONS OF AEROELASTICITY SYSTEMS

2.1 Introduction

The proposed nonlinear aeroelasticity model is based on the coupling between the structural dynamics, the fluid dynamics and the mesh models through an information transfer module (matcher). The nonlinearity is assumed only from the Euler equations of transonic airflow. For the structural nonlinearity, the reader is referred to Ref. [41, 72, 73]. The coupling procedure performs the exchanges between the aerodynamic loads and the structural motion on the fluid-structure interface.

Theories on which each subsystem is relied will be presented in this chapter. First, the CSD models will be described. The CSD models are derived from shell theory of thin structures. Since the linear dynamic behavior of a structure is characterized by its modes, a modal superposition method can be used. If these modal parameters are available, it is possible to resolve the differential equations by the mode superposition approach which is much more economic than the direct finite element discrete approach. The nonlinear aerodynamic model is described by the nonlinear Euler equations in ALE kinematic description with moving mesh [55, 58]. Finally the information transfer "matcher" module will be presented.

2.2 Structural dynamics model

Structural dynamics describes the behavior of a moving structure as a function of time. Such behavior is usually expressed by partial differential equations in the Lagrangian description, where the motion of particles is observed. For simple problems, analytical solutions of these partial differential equations can be found. But for problems with a complex

geometry, these equations are solved by numerical methods which give approximate solutions at certain spatial points and at certain instants.

2.2.1 Shell structures

A real wing is a complicated structure which is composed of several components (Figure 3). Wing structures [74] are usually modeled using finite elements, such as three dimensional solid, beam, plate and shell elements. A complete design of a wing-box modeled with beams, plates and other structural elements can be found in Ref. [75]. Since an aircraft wing skin has usually small thickness compared to the other dimensions, they can be approximately modeled by shells. A shell structure is particularly a three-dimensional

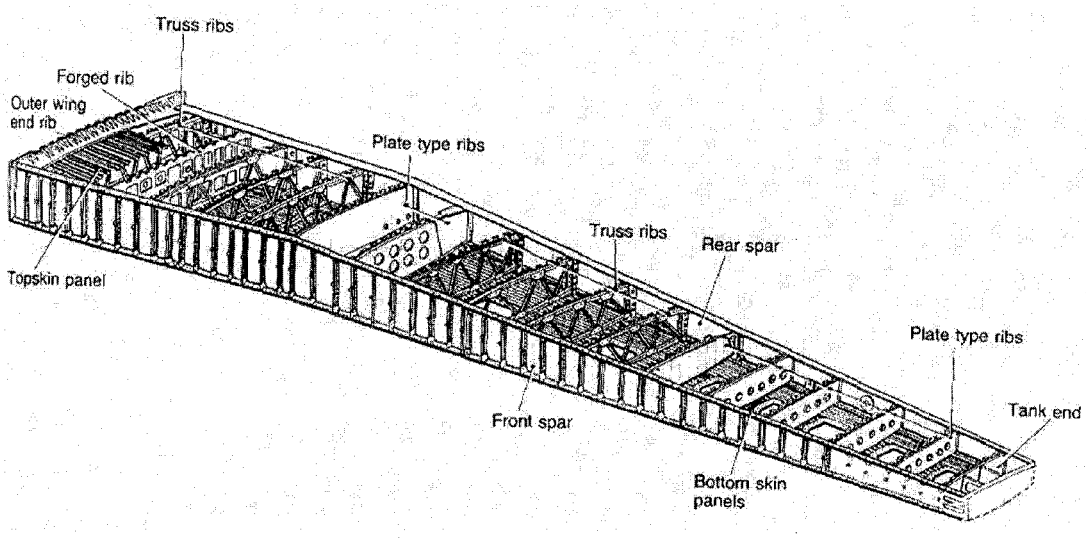

Figure 3 Wing-box configuration (sources from Ref. [76])

solid with a small thickness. It is bounded by two closely spaced curved surfaces. Another curved surface generated by the points on the half distance between these two curved surfaces is known as the middle surface. This surface characterizes the behavior of the shell. The deformation of the shell is determined completely by the displacement of the middle

surface. In this thesis, the material is supposed isotropic and homogenous. The relation between the stress and the deformation is considered linear. Furthermore, the displacement in the thickness direction is assumed linear and small. It is assumed that any straight line normal to the middle surface stays straight after deformations. The hypothesis of plane stress is also applied to uncouple the effects between the membrane bending and the transversal strain. The structural dynamic model is based on the following shell theories [77]. Since our test case is the AGARD 445.6 aeroelastic wing which is an experimental wing with small thickness, we will consider only shell structural elements.

2.2.1.1 Description of a middle surface

The dynamic behaviors of a shell are characterized by its middle surface described in the 3D Cartesian coordinate system. However, any point on the middle surface can be determined by two independent curvilinear coordinates ξ and η. Suppose that p is a point on the middle surface (Figure 4), its position vector $\mathbf{x}_p$ can be written as :

$$\mathbf{x}_p = X(\xi,\eta)\mathbf{i} + Y(\xi,\eta)\mathbf{j} + Z(\xi,\eta)\mathbf{k} \tag{2.1}$$

where **i**, **j** and **k** denote the orthogonal vectors in the Cartesian coordinate system with fixed global reference; X, Y, Z denote the Cartesian coordinates.

The position differential vector $d\mathbf{x}_p$ of point p is a function of $d\xi$ and $d\eta$:

$$d\mathbf{x}_p = \mathbf{x}_{p,\xi}d\xi + \mathbf{x}_{p,\eta}d\eta = \mathbf{a}_1 d\xi + \mathbf{a}_2 d\eta \tag{2.2}$$

where $\mathbf{a}_1$ and $\mathbf{a}_2$ are covariant base vectors which are tangent to the directions defined by ξ and η. In the Cartesian coordinate system, they are defined as :

$$\mathbf{a}_1 = X_{,\xi}\mathbf{i} + Y_{,\xi}\mathbf{j} + Z_{,\xi}\mathbf{k} \tag{2.3}$$

$$\mathbf{a}_2 = X_{,\eta}\mathbf{i} + Y_{,\eta}\mathbf{j} + Z_{,\eta}\mathbf{k} \tag{2.4}$$

where $X_{,\xi}$, $Y_{,\xi}$ and $Z_{,\xi}$ are the partial derivatives of X, Y and Z in ξ; $X_{,\eta}$, $Y_{,\eta}$ and $Z_{,\eta}$ are the partial derivatives of X, Y and Z in η. A unit vector normal to plane $(\mathbf{a}_1, \mathbf{a}_2)$ can be obtained from $\mathbf{a}_1$ and $\mathbf{a}_2$:

$$\mathbf{n} = \frac{\mathbf{a}_1 \times \mathbf{a}_2}{|\mathbf{a}_1 \times \mathbf{a}_2|} \tag{2.5}$$

Vectors $\mathbf{a}_1, \mathbf{a}_2, \mathbf{n}$ define a vector basic for the middle surface :

$$[\mathbf{F}_0] = [\mathbf{a}_1 \vdots \mathbf{a}_2 \vdots \mathbf{n}]$$

The vector base $\mathbf{a}_1$ and $\mathbf{a}_2$ are not orthogonal. Hence, another useful orthogonal base $\mathbf{t}_1, \mathbf{t}_2$ and $\mathbf{n}$ is defined as :

$$[\mathbf{Q}] = [\mathbf{t}_1 \vdots \mathbf{t}_2 \vdots \mathbf{n}]$$

with

$$\mathbf{t}_1 = \mathbf{a}_1/|\mathbf{a}_1|$$

$$\mathbf{t}_2 = \mathbf{n} \times \mathbf{t}_1$$

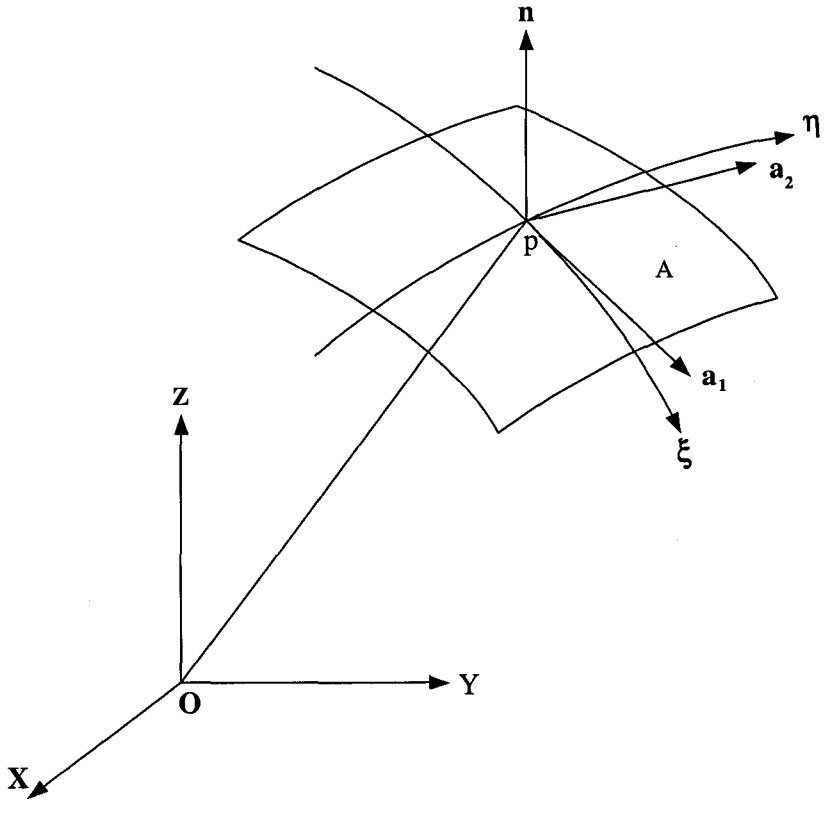

Figure 4 Description of a point on the middle surface

2.2.1.2 Virtual displacement

For a thin shell with constant thickness h and defined by middle surface A through the natural coordinates ξ and η (Figure 5), its coordinate z in the thickness direction is :

$$z = \zeta \frac{h}{2}, \text{ with } -1 \leq \zeta \leq 1$$

Suppose that a point $q(\xi, \eta, \zeta)$ is in the thin shell at the initial time and its corresponding point on the middle surface is defined by equation (2.1). So vector **pq** is normal to the middle surface at point p. The position vector of point q at the initial time is defined as :

$$\mathbf{x}_q(\xi,\eta,\zeta) = \mathbf{x}_p(\xi,\eta) + \zeta\frac{h}{2}\mathbf{n}(\xi,\eta) \tag{2.6}$$

After deformation, point p on the middle surface described by equation (2.1) has moved to position p^* and point q has moved to position q^* (Figure 5). The virtual displacement $\mathbf{u}_q^*$ of point q is defined by the following equations :

$$\mathbf{u}_q^*(\xi,\eta,\zeta) = \mathbf{u}_p^*(\xi,\eta) + \zeta\frac{h}{2}\boldsymbol{\beta}^*(\xi,\eta) \tag{2.7}$$

with

$$\boldsymbol{\beta}^* \cdot \mathbf{n} = 0$$

and

$$\boldsymbol{\beta}^* = \beta_1^*\mathbf{t}_1 + \beta_2^*\mathbf{t}_2$$

where $\mathbf{u}_p^*$ is the virtual displacement of point p, β_1^* is the rotation of vector $\mathbf{n}$ in $(\mathbf{n},\mathbf{t}_1)$ plane, β_2^* is the rotation of vector $\mathbf{n}$ in $(\mathbf{n},\mathbf{t}_2)$ plane.

2.2.1.3 Virtual deformations

The virtual configuration C^* is defined by the virtual position vector $\mathbf{x}_q^*$ which results from the superposition of position vector $\mathbf{x}_q$ and any virtual displacement vector $\mathbf{u}_q^*$ (Figure 5) :

$$\mathbf{x}_q^*(\xi,\eta,\zeta) = \mathbf{x}_q(\xi,\eta,\zeta) + \mathbf{u}_q^*(\xi,\eta,\zeta) \tag{2.8}$$

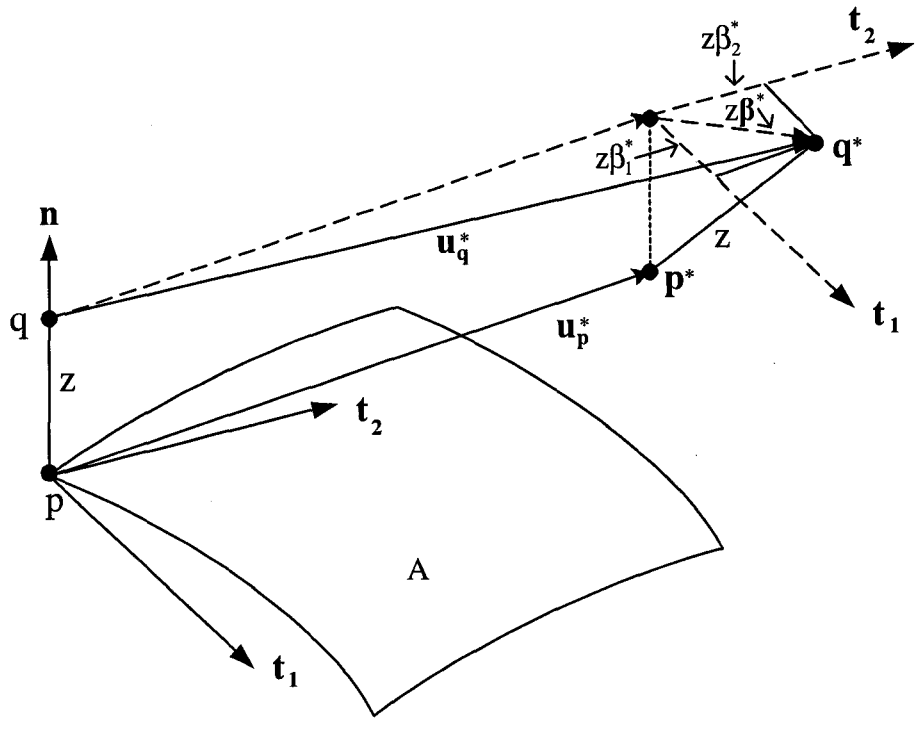

Figure 5 Description of a point inside a shell

The differential of the virtual position vector $d\mathbf{x}_q^*$ is :

$$d\mathbf{x}_q^* = d\mathbf{x}_q + d\mathbf{u}_q^* \tag{2.9}$$

The differentials $d\mathbf{x}_q$ and $d\mathbf{u}_q^*$ can be written as :

$$d\mathbf{x}_q = \mathbf{x}_{q,\xi} d\xi + \mathbf{x}_{q,\eta} d\eta + \frac{h}{2}\mathbf{n} d\zeta \tag{2.10}$$

$$d\mathbf{u}_q^* = \mathbf{u}_{q,\xi}^* d\xi + \mathbf{u}_{q,\eta}^* d\eta + \frac{h}{2}\boldsymbol{\beta}^* d\zeta \tag{2.11}$$

Equations (2.10) and (2.11) give the following relation between the differentials of the

virtual displacement $d\mathbf{u}_q^*$ and the real position vector $d\mathbf{x}_q$:

$$\{d\mathbf{u}_q^*\} = [\mathbf{L}^*]\{d\mathbf{x}_q\} \tag{2.12}$$

with

$$[\mathbf{L}^*] = [\mathbf{L}_\zeta^*][\mathbf{F}_\zeta]^{-1}$$

$$[\mathbf{L}_\zeta^*] = [\mathbf{u}_{q,\xi}^* \vdots \mathbf{u}_{q,\eta}^* \vdots \frac{h}{2}\boldsymbol{\beta}^*]$$

$$[\mathbf{F}_\zeta] = [\mathbf{x}_{q,\xi} \vdots \mathbf{x}_{q,\eta} \vdots \frac{h}{2}\mathbf{n}]$$

A curvilinear orthogonal base $\mathbf{t}_{1\zeta}$, $\mathbf{t}_{2\zeta}$ and $\mathbf{n}_\zeta$ is defined on a tangent plane of point q :

$$[\mathbf{Q}_\zeta] = [\mathbf{t}_{1\zeta} \vdots \mathbf{t}_{2\zeta} \vdots \mathbf{n}_\zeta] \qquad \text{with} \quad \mathbf{n}_\zeta = \frac{h}{2}\mathbf{n}$$

The Cartesian differentials $d\mathbf{u}_q^*$, $d\mathbf{x}_q^*$ and the curvilinear differentials $\{d\mathbf{u}_q^*\}_t$, $\{d\mathbf{x}_q\}_t$ are associated by $[\mathbf{Q}_\zeta]$:

$$\{d\mathbf{u}_q^*\} = [\mathbf{Q}_\zeta]\{d\mathbf{u}_q^*\}_t \tag{2.13}$$

$$\{d\mathbf{x}_q\} = [\mathbf{Q}_\zeta]\{d\mathbf{x}_q\}_t \tag{2.14}$$

hence

$$\{d\mathbf{u}_q^*\}_t = [\mathbf{L}_t^*]\{d\mathbf{x}_q\}_t \tag{2.15}$$

where the subscript t indicates the curvilinear coordinate system. Therefore from equations (2.12), (2.13), (2.14) and (2.15), one obtains the relation between the differential of the virtual displacement vector and the position vector :

$$[\mathbf{L}_t^*] = [\mathbf{Q}_\zeta]^T[\mathbf{L}^*][\mathbf{Q}_\zeta] = [\mathbf{Q}_\zeta]^T[\mathbf{L}_\zeta^*][\mathbf{F}_\zeta]^{-1}[\mathbf{Q}_\zeta]$$

The virtual linear strain tensor in the curvilinear coordinate system is defined by the following symmetrical tensor :

$$[\varepsilon_t^*] = \frac{1}{2}([\mathbf{L}_t^*] + [\mathbf{L}_t^*]^T)$$

with

$$[\varepsilon_t^*] = \begin{bmatrix} \varepsilon_x^* & \frac{1}{2}\gamma_{xy}^* & \frac{1}{2}\gamma_{xz'}^* \\ & \varepsilon_y^* & \frac{1}{2}\gamma_{yz'}^* \\ sym. & & \varepsilon_{z'}^* \end{bmatrix}$$

where x, y are curvilinear coordinates in the orthogonal base $\mathbf{t}_{1\zeta}$, $\mathbf{t}_{2\zeta}$ and $\mathbf{n}_\zeta$. Although $\varepsilon_{z'}^*$ is not zero, its contribution to the virtual work principle is zero since its corresponding stress is zero according to hypothesis of plane stress. So $\varepsilon_{z'}^*$ can be considered zero in the following deformation vector :

$$< \varepsilon_t^* > = << \varepsilon_s^* > \vdots < \gamma_s^* >>$$

where $< \varepsilon_s^* >$ and $< \gamma_s^* >$ are respectively the deformation vectors due to membrane bending and the deformation of shear strain as follow :

$$< \varepsilon_s^* > = < \varepsilon_x^* \quad \varepsilon_y^* \quad \gamma_{xy}^* > \; ; \qquad < \gamma_s^* > = < \gamma_{xz'}^* \quad \gamma_{yz'}^* >$$

2.2.1.4 Principle of virtual work (Mindlin theory)

The hypothesis of the plane stress applied to models of thin shells can be written as :

$$\sigma_{z'} = 0$$

where z' is the direction defined by the unit vector $\mathbf{n}_\zeta$. The components of stress represented in the local coordinate system are :

$$[\sigma_t] = \begin{bmatrix} \sigma_x & \sigma_{xy} & \sigma_{xz'} \\ & \sigma_y & \sigma_{yz'} \\ sym. & & 0 \end{bmatrix}$$

The stress is written in the following vector form :

$$\{\sigma_t\} = < \sigma_x \quad \sigma_y \quad \sigma_{xy} \quad \sigma_{xz'} \quad \sigma_{yz'} >^T$$

Therefore, the internal virtual work represented in the local coordinate system can be written as :

$$W_{int} = \int_V tr([\mathbf{L}_t^*][\sigma_t])dV = \int_V tr([\varepsilon_t^*][\sigma_t])dV = \int_V < \varepsilon_t^* > \{\sigma_t\}dV \qquad (2.16)$$

where tr denotes the trace of a linear matrix.

2.2.1.5 Relation between the stress and the deformation

The hypotheses of linear and isotropic elastic material yield the following linear relation between the stress and the deformation :

$$\{\sigma_t\} = [\mathbf{H}_t]\{\varepsilon_t\}$$

where $[\mathbf{H}_t]$ is a matrix with constant components, $\{\sigma_t\}$ is the stress vector and $\{\varepsilon_t\}$ is the deformation vector. The hypothesis of the uncoupling effects between the membrane bending and the shear stress gives the following components of matrix $[\mathrm{H}_t]$ with the neutral axis normal to the middle surface :

$$[\mathbf{H}_t] = \begin{bmatrix} [H] & 0 \\ 0 & [G] \end{bmatrix}$$

$$[\mathbf{H}] = \begin{bmatrix} H_{11} & H_{12} & H_{13} \\ & H_{22} & H_{23} \\ sym. & & H_{33} \end{bmatrix}$$

$$[\mathbf{G}] = \begin{bmatrix} H_{44} & H_{45} \\ sym. & H_{55} \end{bmatrix}$$

The matrices $[\mathbf{H}]$ and $[\mathbf{G}]$ are symmetrical. Using the hypothesis of isotropic material, one obtains :

$$[\mathbf{H}] = \frac{E}{1-\nu^2} \begin{bmatrix} 1 & \nu & 0 \\ & 1 & 0 \\ sym. & & \dfrac{1-\nu}{2} \end{bmatrix}$$

$$[\mathbf{G}] = \frac{E}{2(1+\nu)} \begin{bmatrix} 1 & 0 \\ sym. & 1 \end{bmatrix}$$

where E and ν are the elastic modulus and the Poisson coefficient. Hence, the internal work described by equation (2.16) becomes :

$$W_{int} = \int_V < \varepsilon_s^* \quad \gamma_s^* > \begin{bmatrix} [\mathbf{H}] & 0 \\ 0 & [\mathbf{G}] \end{bmatrix} \begin{Bmatrix} \varepsilon_s \\ \gamma_s \end{Bmatrix} dV$$

It can be developed as :

$$W_{int} = \int_V (< \varepsilon_s^* > [\mathbf{H}]\{\varepsilon_s\} + < \gamma_s^* > [\mathbf{G}]\{\gamma_s\}) dV = W_m + W_c \tag{2.17}$$

where W_m is the internal work due to the effect of the membrane bending, W_c is the internal work due to the shear stresses.

The conservation of energy expresses that the internal virtual work is equal to the internal work for a structure in equilibrium :

$$W_{int} = W_{ext} \tag{2.18}$$

where W_{ext} is the external work. Suppose that the external forces are the inertial forces of a structure and a concentrating force on a point A, the external virtual work can be written as :

$$W_{ext} = \mathbf{u}_{pA}^* \cdot \mathbf{F}_A - \int_V \mathbf{u}_q^* \rho \ddot{\mathbf{u}}_q^* dV \tag{2.19}$$

where $\mathbf{F}_A$ is the concentrating force at point A, $\mathbf{u}_{pA}^*$ is the displacement vector of node pA. The second term on the right hand side represents the external virtual work due to the inertial forces of the structure.

The integral equations (2.17) and (2.19) can be discretized in space using a numerical method, such as the finite element method [78]. Finally, one can obtain the following

semi-discretized system of equations from equations (2.18) and (2.19) :

$$\mathbf{M}\ddot{\mathbf{u}}(t) + \mathbf{K}\mathbf{u}(t) = \mathbf{F}(t) \tag{2.20}$$

where $\mathbf{u}$ is the nodal displacement vector, $\mathbf{M}$ and $\mathbf{K}$ are the structural mass and stiffness matrices which are symmetrical and positive definite, $\mathbf{F}(t)$ represents the external nodal forces.

2.2.2 Modal superposition approach

Structural vibrations are usually dominated by fundamental frequencies. The displacement can be approached by the first few modes. Modal superposition of truncated modes is an economical way to obtain the structural responses. The following subsections describe the modal analysis method [79, 80]. This method is widely applied in linear structural dynamics [40, 81–84].

2.2.2.1 Eigenmodes and Natural Frequencies

The matrix equations (2.20) for free vibrations without damping are characterized by their mode shapes and natural frequencies. Replacing the external force vector on the right hand side of these equations by zero yields the following natural vibration equations :

$$\mathbf{M}\ddot{\mathbf{u}}(t) + \mathbf{K}\mathbf{u}(t) = 0 \tag{2.21}$$

For each node, the displacement vector $\mathbf{u}(t)$ is defined as :

$$\mathbf{u}_t = < \; u_x \quad u_y \quad u_z \quad \theta_{yz} \quad \theta_{zx} \quad \theta_{xy} \; >^T$$

where u_x, u_y, u_z are the translation displacements in x, y, z directions and θ_{yz}, θ_{zx}, θ_{xy} are the rotational displacements around axes x, y, z. The displacement vector $\mathbf{u}(t)$ can be supposed as the following harmonic type :

$$\mathbf{u}(t) = \mathbf{p}_0 \alpha \cos(\omega_0 t - \phi_0) \tag{2.22}$$

where α, ω_0 and ϕ_0 are respectively the referential amplitude, the frequency of motion and the phase. $\mathbf{p}_0$ is a constant vector; the subscript 0 indicates that the parameter is corresponding to vibration with no damping.

Replacing respectively $\mathbf{u}(t)$ and its second derivative $\ddot{\mathbf{u}}(t)$ in equations (2.21) by equations (2.22) and by its second derivative yields the following matrix equations :

$$(\mathbf{K} - \omega_0^2 \mathbf{M})\mathbf{p}_0 = (\mathbf{K} - \lambda_0 \mathbf{M})\mathbf{p}_0 = 0 \tag{2.23}$$

where $\lambda_0 = \omega_0^2$ represents the eigenvalue. These linear equations give n non-trivial solutions $p_{0i} (i = 1, 2, ..., n)$ which verify the following equations :

$$(\mathbf{K} - \omega_{0i}^2 \mathbf{M})\mathbf{p}_{0i} = (\mathbf{K} - \lambda_{0i} \mathbf{M})\mathbf{p}_{0i} = 0 \qquad (i = 1, 2, ..., n) \tag{2.24}$$

where $\mathbf{p}_{0i}$ is the ith mode vector, λ_{0i} is the ith eigenvalue, ω_{0i} is the ith natural frequency which is one root of the following algebraic characteristic equation :

$$det(\mathbf{K} - \omega_0^2 \mathbf{M}) = det(\mathbf{K} - \lambda_0 \mathbf{M}) = 0 \tag{2.25}$$

Hence the n non-trivial solutions of equations (2.24) can be written as :

$$\mathbf{u}_i(t) = \mathbf{p}_{0i} \alpha_i \cos(\omega_{0i} t - \phi_{0i}) \tag{2.26}$$

The orthogonality of the modal vectors is a fundamental property which makes equations (2.21) uncoupled. For any two natural frequencies ω_{0i} and ω_{0j} with corresponding modal vector $\mathbf{p}_{0i}$ and $\mathbf{p}_{0j}$, equations (2.24) give the following two equations :

$$\mathbf{K}\mathbf{p}_{0i} = \omega_{0i}^2\mathbf{M}\mathbf{p}_{0i} \tag{2.27}$$

$$\mathbf{K}\mathbf{p}_{0j} = \omega_{0j}^2\mathbf{M}\mathbf{p}_{0j} \tag{2.28}$$

Multiplying equations (2.27) by $\mathbf{p}_{0j}^T$, then transposing the left and right hand sides yields :

$$\mathbf{p}_{0j}^T\mathbf{K}^T\mathbf{p}_{0i} = \omega_{0i}^2\mathbf{p}_{0j}^T\mathbf{M}^T\mathbf{p}_{0i} \tag{2.29}$$

Because $\mathbf{M}$ and $\mathbf{K}$ are symmetrical and positively defined, these equations can be written as :

$$\mathbf{p}_{0i}^T\mathbf{K}\mathbf{p}_{0j} = \omega_{0i}^2\mathbf{p}_{0i}^T\mathbf{M}\mathbf{p}_{0j} \tag{2.30}$$

Similarly, multiplying equations (2.28) by $\mathbf{p}_{0i}^T$ yields :

$$\mathbf{p}_{0i}^T\mathbf{K}\mathbf{p}_{0j} = \omega_{0j}^2\mathbf{p}_{0i}^T\mathbf{M}\mathbf{p}_{0j} \tag{2.31}$$

Subtracting equations (2.30) from equations (2.31) yields :

$$(\omega_{0i}^2 - \omega_{0j}^2)\mathbf{p}_{0i}^T\mathbf{M}\mathbf{p}_{0j} = 0 \tag{2.32}$$

If $i \neq j$, then equations (2.31) and (2.32) give the following orthogonal property between modal vectors : $\mathbf{p}_{0i}^T$ and $\mathbf{p}_{0j}^T$ $(i = 1, 2, ..., n)$:

$$\mathbf{p}_{0i}^T \mathbf{M} \mathbf{p}_{0j} = 0$$
$$\mathbf{p}_{0i}^T \mathbf{K} \mathbf{p}_{0j} = 0$$

If $i = j$, equations (2.31) and (2.32) give :

$$\mathbf{p}_{0i}^T \mathbf{M} \mathbf{p}_{0i} = \mu_i$$
$$\mathbf{p}_{0i}^T \mathbf{K} \mathbf{p}_{0i} = \kappa_i \omega_{0i}^2$$

where μ_i and κ_i are two non-zero scales. Because multiplication of a modal vector by a scale gives the same modal vector, μ_i and κ_i can be chosen as unity. Therefore, the normalization by the mass matrix gives the following general orthogonal property

$$\mathbf{p}_{0i}^T \mathbf{M} \mathbf{p}_{0i} = \delta_{ij}$$
$$\mathbf{p}_{0i}^T \mathbf{K} \mathbf{p}_{0i} = \omega_{0i}^2$$

where δ_{ij} is the Kronecker symbol. The n linear independent modal vectors $\mathbf{p}_{0i} (i = 1, 2, ..., n)$ give the following modal matrix $\mathbf{P}_0$:

$$\mathbf{P}_0 = [\ \mathbf{p}_{01}\ \ \mathbf{p}_{02}\ \ \mathbf{p}_{03}\ \ \cdots\cdots\ \ \mathbf{p}_{0n}\ ]$$

Hence, the orthogonality can be expressed as :

$$\mathbf{P}_0^T \mathbf{M} \mathbf{P}_0 = \mathbf{I}$$
$$\mathbf{P}_0^T \mathbf{K} \mathbf{P}_0 = \mathbf{\Lambda}$$

where $\mathbf{I}$ is a unit matrix of order n, $\mathbf{\Lambda}$ is a diagonal matrix with square frequencies on the diagonal elements as :

$$\mathbf{\Lambda} = diag(\ \omega_{01}^2\ \ \omega_{02}^2\ \ \omega_{03}^2\ \ .....\ \ \omega_{0n}^2\ )$$

2.2.2.2 Complete Modal Superposition

The linear combination of n modal vectors $\mathbf{p}_0$ $(n = 1, 2, 3, ..., n)$ represents the temporal responses $\mathbf{u}(t)$ of the discrete partial differential equations of a structural system in a forced regime described by the following matrix equations :

$$\mathbf{M}\ddot{\mathbf{u}}(t) + \mathbf{D}\dot{\mathbf{u}}(t) + \mathbf{K}\mathbf{u}(t) = \mathbf{F}(t) \tag{2.33}$$

with its initial conditions :

$$\mathbf{u}(0) = \mathbf{u}_0$$

$$\dot{\mathbf{u}}(0) = \dot{\mathbf{u}}_0$$

where **D** is the Rayleigh damping matrix which is given by the following equations :

$$\mathbf{D} = \alpha\mathbf{M} + \beta\mathbf{K}$$

where α, β denote respectively the coefficients proportional to the mass and stiffness matrices **M** and **K** [80].

In equations (2.33), $\mathbf{u}(t)$ is the displacement vector normalized by the mass matrix which can be described as :

$$\mathbf{u}(t) = \sum_{i=1}^{n} z_i \mathbf{p}_{0i} = \mathbf{P}_0 \mathbf{z}(t) \tag{2.34}$$

where $\mathbf{P}_0$ is the mode matrix, $\mathbf{z}(t)$ is a generalized modal coordinates vector described as :

$$\mathbf{z(t)} = [\ z_1\ \ z_2\ \ z_3\ \ .....\ \ z_n\ ]$$

Replacing $\mathbf{u}(t)$ and its first and second derivatives in equation (2.33) by those of equation (2.34), then multiplying it by the transpose of mode matrix $\mathbf{P}_0^T$ and finally normalizing it by the mass matrix $\mathbf{M}$ yields :

$$\ddot{\mathbf{z}}(t) + \Delta_0 \dot{\mathbf{z}}(t) + \Lambda_0 \mathbf{z} = \mathbf{s}_0(t) \tag{2.35}$$

with the following initial conditions :

$$\mathbf{z}(0) = \mathbf{P}_0^T \mathbf{M} \mathbf{u}_0$$
$$\dot{\mathbf{z}}(0) = \mathbf{P}_0^T \mathbf{M} \dot{\mathbf{u}}_0$$

where Δ_0 ($\Delta_0 = \mathbf{P}_0^T \mathbf{D} \mathbf{P}$) and Λ_0 ($\Lambda_0 = \mathbf{P}_0^T \mathbf{K} \mathbf{P}$) are respectively the modal damping matrix and the modal stiffness matrix. $\mathbf{s}_0(t)$ ($\mathbf{s}_0(t) = \mathbf{P}_0^T \mathbf{F}(t)$) is the modal force vector.

Because the matrices Δ_0 and Λ_0 are diagonal matrices in equations (2.35), the matrix equations (2.33) which are coupled among the n degrees of freedom can be transformed into n uncoupled equations described as below :

$$\ddot{z}_i(t) + \delta_{0i} \dot{z}_i(t) + \lambda_{0i} z_i(t) = \ddot{z}_i(t) + 2\eta_i \omega_{0i} \dot{z}_i(t) + \omega_{0i}^2 z_i(t) = s_{0i}(t) \tag{2.36}$$

with the following initial conditions :

$$z_i(0) = \mathbf{p}_{0i}^T \mathbf{M} \mathbf{u}_0$$
$$\dot{z}_i(0) = \mathbf{p}_{0i}^T \mathbf{M} \dot{\mathbf{u}}_0$$

where $\eta_i = \delta_{0i}/(2\omega_{0i})$ is the ith modal damping coefficient, $s_{0i}(t) = \mathbf{p}_{0i}^T \mathbf{F}(t)$ is the ith modal excitation. Each uncoupled equation can be explicitly integrated. The solution of

equation (2.36) can be written as :

$$z_i(t) = e^{-\eta_i \omega_{0i} t} \left\{ \frac{\dot{z}_i(0) + \eta_i \omega_{0i} z_i(0)}{\omega_i} \sin \omega_i t + z_i(0) \cos \omega_i t \right\} + \frac{\int_0^t s_{0i}(t-\tau) e^{-\eta_i \omega_{0i} \tau} \sin \omega_i \tau d\tau}{\omega_i} \tag{2.37}$$

where ω_{0i} is the ith natural frequency and $\omega_i = \omega_{0i}\sqrt{1-\eta_i^2}$ is the ith structural frequency with damping.

The general solution for forced regime described by matrix equation (2.33) can be obtained using the modal superposition approach with the first n modal responses described by equation (2.36) :

$$\mathbf{u}(t) = \mathbf{u}_{solicit}(t) + \mathbf{u}_{init}(t) \tag{2.38}$$

with

$$\mathbf{u}_{solicit}(t) = \sum_{i=1}^{n} \frac{\mathbf{p}_{0i}}{\omega_i} \int_0^t s_{0i}(t-\tau) e^{-\eta_i \omega_{0i} \tau} \sin \omega_i \tau d\tau \tag{2.39}$$

$$\mathbf{u}_{init}(t) = \sum_{i=1}^{n} \mathbf{p}_{0i}^T \mathbf{M} e^{-\eta_i \omega_{0i} t} \left\{ \frac{1}{\omega_i} [\dot{\mathbf{u}}_0 + \eta_i \omega_{0i} \mathbf{u}_0] \sin \omega_i t + \mathbf{u}_0 \cos \omega_i t \right\} \tag{2.40}$$

If the excitation is assumed as $\mathbf{F}(t) = \mathbf{g}\psi(t)$, where $\mathbf{g}$ is a static solicitation which is independent of time and $\psi(t)$ is a time scale function, the modal force can be written as :

$$s_{0i}(t) = \mathbf{p}_{0i}^T \mathbf{g} \psi(t)$$

Furthermore, if the structural system is initially immobile ($\mathbf{u}_0 = 0$ and $\dot{\mathbf{u}}_0 = 0$), the general responses described by equations (2.38) become :

$$\mathbf{u}(t) = \sum_{i=1}^{n} \frac{\mathbf{p}_{0i}\mathbf{p}_{0i}^T\mathbf{g}}{\omega_i} \int_0^t \psi(t-\tau) e^{-\eta_i \omega_{0i} \tau} \sin \omega_i \tau d\tau \tag{2.41}$$

These responses show that the modes with high natural frequencies have less influence on the displacement than the fundamental natural frequencies because the responses are divided by the natural frequency ω_i and $e^{-\eta_i \omega_{0i} t}$ decays more quickly.

2.2.2.3 Partial Modal Superposition

Since the main contribution to the response is given by the fundamental modes, the modes can be limited to a certain number for the purpose of reducing the computation cost in the forced regime. If the first $m(m < n)$ modes $\mathbf{p}_{0i}(i = 1, 2, ..., m)$ are used to get the responses, the time responses can be approximated by :

$$\mathbf{u}(t) = \sum_{i=1}^{m} z_i(t) \mathbf{p}_{0i} \tag{2.42}$$

where z_i is the ith generalized coordinate. Substituting the displacement vector described by equations (2.42) and its first and second derivatives into equations (2.33) yields :

$$\ddot{z}_i(t) + 2\eta_i \omega_{0i} \dot{z}_i(t) + \omega_{0i}^2 z_i(t) = s_{0i}(t) \qquad (i = 1, 2, ..., m) \tag{2.43}$$

For an initially immobile structure, if the excitation is in the form $\mathbf{F}(t) = \mathbf{g}\psi(t)$ on a structure initially immobile, the responses can be written as :

$$\mathbf{u}(t) = \sum_{i=1}^{m} \frac{\mathbf{p}_{0i}\mathbf{p}_{0i}^{T}\mathbf{g}}{\omega_i}\theta_i(t) \tag{2.44}$$

with

$$\theta_i(t) = \int_0^t \psi(t-\tau)e^{-\eta_i\omega_{0i}\tau}\sin\omega_i\tau d\tau$$

where $\mathbf{g}$ is a vector which is independent of time, θ_i is a temporal factor which depends on the structural spectrum and the time scalar function $\psi(t)$.

2.3 Unsteady aerodynamics

Aerodynamics is the study of the dynamic behavior of airflow which is usually viscous and compressible. This behavior can be described by mathematical equations under certain hypotheses. In the early days, in order to get accessible knowledge of aerodynamic behavior by the available computing technologies, different hypotheses for airflow behavior were applied to simplify the aerodynamic description. For example, airflow at low speed is considered inviscid incompressible where linear theories can be applied. At high speed, where the elasticity characterized by sound, air speed must be considered, airflow far from solid boundaries can be still considered inviscid, but compressible. These hypotheses yield accurate approximate solutions outside the boundary layer. In this thesis, air is assumed inviscid compressible. More accurate solution can be achieved by considering air as a viscous compressible fluid which is beyond the scope of this thesis.

2.3.1 Linear aerodynamics for inviscid incompressible flow

Aerodynamic behaviors such as lift and moment acting on aircraft is very slightly affected by air elasticity at low flight speed [85] (for example, less than 400 km/h) which was the speed of aircraft in the early days. Since the airflow is assumed inviscid incompressible, the density and temperature are constant. Therefore, only the continuity of mass and the Newton's law govern the flow behavior.

The continuity of mass leads to the following conservation equation which is described by the divergence of a steady flow at any point in the flow field. For a control volume the mass getting in is equal to the mass getting out, hence :

$$div\mathbf{u} = 0 \tag{2.45}$$

where **u** is the velocity of airflow at the point.

The Newton's law yields the following equations of momentum conservation :

$$\rho\frac{D\mathbf{u}}{Dt} = \rho\mathbf{g} - \nabla p \tag{2.46}$$

where p defines the pressure at any point in the flow field, $D\mathbf{u}/Dt$ defines particle acceleration, ρ defines the density of air and **g** defines the acceleration of gravity.

The flow can be considered irrotational. An irrotational flow is characterized by its zero vorticity ($\omega = 0$) and can be described by a velocity potential. The velocity potential associates with flow velocity through the following equation :

$$\mathbf{u} = \nabla\phi$$

where ϕ is velocity potential. Equation (2.45) become the potential equation as :

$$\nabla^2\phi = 0$$

2.3.2 Linear aerodynamics for inviscid compressible flow

Compressible flow is characterized by the Mach number which is the ratio of air speed to the sound speed. The density is no longer considered constant. The temperature has become a variable as well. As air can still be considered inviscid, potential flow is still available to describe its dynamic behavior. The equation of continuity for steady inviscid compressible flow is :

$$div(\rho\mathbf{u}) = 0 \tag{2.47}$$

It can be described by the following velocity potential equation :

$$\frac{\partial}{\partial x}\left(\rho\frac{\partial\phi}{\partial x}\right) + \frac{\partial}{\partial y}\left(\rho\frac{\partial\phi}{\partial y}\right) + \frac{\partial}{\partial z}\left(\rho\frac{\partial\phi}{\partial z}\right) = 0 \tag{2.48}$$

After development, it becomes :

$$\rho\nabla^2\phi + u\frac{\partial\rho}{\partial x} + v\frac{\partial\rho}{\partial y} + w\frac{\partial\rho}{\partial z} = \rho\nabla^2\phi + (\mathbf{u}\cdot\nabla)\rho = 0 \tag{2.49}$$

If the variation of density is very small, the nonlinear term $(\mathbf{u}\cdot\nabla)\rho$ can be neglected compared to $\rho\nabla^2\phi$. Therefore, the governing equation for inviscid compressible flow becomes :

$$\nabla^2\phi \approx 0 \tag{2.50}$$

This is a linear equation similar to that of an inviscid incompressible flow. The neglected term $(\mathbf{u} \cdot \nabla)\rho$ depends on air speed. When the air speed increases, the importance of this term increases, and the accuracy of the solutions decreases. Furthermore, at high air speed, other phenomena such as shock formation will also affect the computational accuracy.

2.3.3 Nonlinear aerodynamics for inviscid compressible flow

Since the temperature changes in compressible flow, the mechanical energy is no longer conserved. The first law of thermodynamics must be applied. The equation of conservation of energy includes intrinsic energy which involves air temperature. The equations of states are also used to close the equations of conservation of mass, momentum and energy since two additional unknowns (the temperature and the density) are added to the system of equations.

Air can be considered as perfect gas at a low temperature whose state can be described by the following equation :

$$p = \rho RT \tag{2.51}$$

where R is air constant which depends on the molecular weight of gas, T is air temperature, p is the gas pressure. Evidently, only two of the three variables p, ρ and T determine the state of gas. Therefore, the intrinsic energy is only a function of temperature :

$$de = C_v dT \tag{2.52}$$

where e is the intrinsic energy, C_v is constant volume specific heat.

The Bernoulli's equation can be written as :

$$\frac{\gamma}{\gamma-1}\frac{p_1^{1/\gamma}}{\rho_1}p^{(\gamma-1)/\gamma}+\frac{V^2}{2}=\frac{\gamma}{\gamma-1}\frac{p_1}{\rho_1}+\frac{V_1^2}{2} \tag{2.53}$$

with

$$\gamma = C_v/C_p$$

where γ is the specific heat ratio, C_p is the constant pressure specific heat.

The following sound speed is the travel speed of small disturbance produced by a moving body in steady compressible fluid, it is a function of variation of pressure and density :

$$a=\sqrt{\frac{dp}{d\rho}}$$

For an isentropic flow, where p/ρ^γ is constant, the sound speed can be written as :

$$a=\sqrt{\gamma\frac{p}{\rho}}$$

For perfect gas, $a=\sqrt{\gamma RT}$, the sound speed depends only on temperature.

Since airflow is no longer considered incompressible at high speed, air elasticity must be considered. Mach number ($M = V/a$) is used to describe the compressibility of air. In incompressible flow, the sound speed is infinite since the density is assumed to be constant. The disturbance caused by a moving body can propagate instantaneously at all points in the fluid. At low Mach number, the speed of moving body is much less than sound speed, the flow field can extend to infinity in all directions. In this case the flow can be still considered approximately as incompressible.

inviscid compressible flow can be described by the small perturbation theory. For a two-dimensional steady compressible flow, the conservation of mass and momentum are represented by the following equations :

$$u\frac{\partial u}{\partial x}+v\frac{\partial u}{\partial y}=-\frac{1}{\rho}\frac{\partial p}{\partial x} \tag{2.54}$$

$$u\frac{\partial v}{\partial x}+v\frac{\partial v}{\partial y}=-\frac{1}{\rho}\frac{\partial p}{\partial y} \tag{2.55}$$

$$\frac{\partial(\rho u)}{\partial x}+\frac{\partial(\rho v)}{\partial y}=0 \tag{2.56}$$

Using the relation $a^2 = dp/d\rho$ and multiplying respectively equations (2.54) and (2.55) by u and v, one obtains :

$$u^2\frac{\partial u}{\partial x}+uv\frac{\partial u}{\partial y}=-\frac{ua^2}{\rho}\frac{\partial \rho}{\partial x} \tag{2.57}$$

$$uv\frac{\partial v}{\partial x}+v^2\frac{\partial v}{\partial y}=-\frac{va^2}{\rho}\frac{\partial \rho}{\partial x} \tag{2.58}$$

Adding equations (2.57) and (2.58) yields :

$$u^2\frac{\partial u}{\partial x}+uv\frac{\partial u}{\partial y}+uv\frac{\partial v}{\partial x}+v^2\frac{\partial v}{\partial y}=-\frac{a^2}{\rho}\left(u\frac{\partial \rho}{\partial x}+v\frac{\partial \rho}{\partial y}\right) \tag{2.59}$$

Equation (2.56) can be developed as :

$$\frac{\partial u}{\partial x}+\frac{\partial v}{\partial y}=-\frac{1}{\rho}\left(u\frac{\partial \rho}{\partial x}+v\frac{\partial \rho}{\partial y}\right) \tag{2.60}$$

From equations (2.59) and (2.60), one obtains :

$$\left(\frac{u^2}{a^2}-1\right)\frac{\partial u}{\partial x}+\frac{uv}{a^2}\left(\frac{\partial u}{\partial y}+\frac{\partial v}{\partial x}\right)+\left(\frac{v^2}{a^2}-1\right)\frac{\partial v}{\partial y}=0 \tag{2.61}$$

Using the properties of irrotational flow yields the following equation :

$$\left(\frac{u^2}{a^2}-1\right)\frac{\partial^2\phi}{\partial x^2}+2\left(\frac{uv}{a^2}\right)\frac{\partial^2\phi}{\partial x\partial y}+\left(\frac{v^2}{a^2}-1\right)\frac{\partial^2\phi}{\partial y^2}=0 \tag{2.62}$$

where ϕ is the velocity potential. For inviscid incompressible flow, the sound speed is infinite. Equation (2.62) becomes the linear Laplace equation. For inviscid compressible flow, equation (2.62) is nonlinear since the coefficients of the second partial derivatives $\partial^2\phi/\partial x^2$, $\partial^2\phi/\partial x\partial y$ and $\partial^2\phi/\partial y^2$ are functions of velocity. However, in the case of inviscid compressible flow past a thin body at a small angle of attack, the disturbance to the flow is very small, therefore the small perturbation method can be applied. For example, for a uniform flow with velocity u_∞ past a thin structure, the components of perturbation of velocity u' and v' can be considered as very small compared to the oncoming velocity u_∞. The total velocity at any point of the flow field can be described by the following two components :

$$u=u_\infty+u'=u_\infty+\frac{\partial\phi}{\partial x} \tag{2.63}$$

$$v=v'=\frac{\partial\phi}{\partial y} \tag{2.64}$$

where ϕ is the perturbation velocity potential. The velocity potential in equation (2.62) can be replaced by perturbation velocity potential since the second partial derivates of the

potential of a uniform velocity are zero. Equation (2.62) yields the following equation after replacing u and v by equation (2.63) and (2.64) :

$$\left(\frac{u_\infty^2 + 2u_\infty u' + u'^2}{a^2} - 1\right)\frac{\partial^2\phi}{\partial x^2} + 2\left(\frac{u_\infty v' + u'v'}{a^2}\right)\frac{\partial^2\phi}{\partial x\partial y} + \left(\frac{v'^2}{a^2} - 1\right)\frac{\partial^2\phi}{\partial y^2} = 0 \tag{2.65}$$

Neglecting the high order of perturbation, equation (2.65) becomes :

$$\left(\frac{u_\infty^2 + 2u_\infty u'}{a^2} - 1\right)\frac{\partial^2\phi}{\partial x^2} + 2\left(\frac{u_\infty v'}{a^2}\right)\frac{\partial^2\phi}{\partial x\partial y} - \frac{\partial^2\phi}{\partial y^2} = 0 \tag{2.66}$$

From the energy equation of an adiabatic flow, one obtains :

$$\frac{V^2}{2} + \frac{a^2}{\gamma - 1} = \frac{V_\infty^2}{2} + \frac{a_\infty^2}{\gamma - 1} \tag{2.67}$$

After **u** is replaced by $(u_\infty + u')\mathbf{i} + v'\mathbf{j}$ and the high order terms of the perturbation velocity are neglected, equation (2.67) becomes :

$$\left(\frac{a}{a_\infty}\right)^2 = 1 - (\gamma - 1)M_\infty^2\frac{u'}{u_\infty} \tag{2.68}$$

Multiplying equation (2.67) by $(a/a_\infty)^2$ yields the following full potential equation :

$$\left[(M_\infty^2-1)+\frac{(\gamma+1)M_\infty^2}{u_\infty}\frac{\partial\phi}{\partial x}\right]\frac{\partial^2\phi}{\partial x^2}+2\left(\frac{M_\infty^2}{u_\infty}\frac{\partial\phi}{\partial y}\right)\frac{\partial^2\phi}{\partial x\partial y} \\ +\left[\frac{(\gamma-1)M_\infty^2}{u_\infty}\frac{\partial\phi}{\partial x}-1\right]\frac{\partial^2\phi}{\partial y^2}=0 \tag{2.69}$$

For a thin structure, the term $2(M_\infty^2\phi_y/u_\infty)$ can be neglected. If the flow is inviscid and incompressible, $M_\infty = 0$, equation (2.69) is still linear Laplace equation. In subsonic flow, M_∞ is small, if :

$$abs\left[\frac{(\gamma+1)M_\infty^2}{u_\infty}\frac{\partial\phi}{\partial x}\right]\ll abs(M_\infty^2-1),$$

the following condition :

$$abs\left[\frac{(\gamma+1)M_\infty^2}{u_\infty}\frac{\partial\phi}{\partial x}\right]\ll 1$$

will be also automatically satisfied, equation (2.69) becomes :

$$(1-M_\infty^2)\frac{\partial^2\phi}{\partial x^2}+\frac{\partial^2\phi}{\partial y^2}=0 \tag{2.70}$$

Therefore, in subsonic flow, a linear equation can still be applied. However, in transonic flow, even for thin structure, equation (2.69) is nonlinear, it becomes the following un-

steady full potential equations :

$$\left[(M_\infty^2-1)+\frac{(\gamma+1)M_\infty^2}{u_\infty}\frac{\partial\phi}{\partial x}\right]\frac{\partial^2\phi}{\partial x^2}+\left[\frac{(\gamma-1)M_\infty^2}{u_\infty}\frac{\partial\phi}{\partial x}-1\right]\frac{\partial^2\phi}{\partial y^2}=0 \qquad (2.71)$$

2.3.4 Conservation equations in the ALE formulation

The physical model of unsteady aerodynamics is usually described in space and in time by partial differential equations using conservation laws. Eulerian kinematic description is applied to obtain these partial differential equations where the domain is fixed. However, it is no longer available to aeroelasticity analysis due to moving boundaries. Arbitrary-Lagrangian-Eulerian (ALE) kinematic description (see section 2.4.1) is used to overcome this restriction. In this section, the conservative equations in this description will be discussed.

Suppose that a system occupies a control volume at initial time. This volume moves with arbitrary velocity **w** (Figure 6). It contains a material characterized by physical quantity **B**, which is related to its physical quantity per unit mass **b** by the following equation :

$$\mathbf{B}(t)=\int_{\Omega_t}\rho\mathbf{b}d\Omega_t$$

where Ω_t is the domain of control volume at instant t, ρ is the fluid density. The variation of **B** from instant t_0 to t is the difference of quantity between the quantity getting into the control volume and the quantity getting out of the control volume in addition to the variation of the quantity in the volume. Its derivative can be described by the following equation :

$$\frac{D\mathbf{B}}{Dt}=\frac{D}{Dt}\int_{\Omega_t}\rho\mathbf{b}D\Omega_t=\lim_{\Delta t\to 0}\frac{\mathbf{B}_{vc}(t)-\mathbf{B}_{vc}(t_0)}{\Delta t}+\oint_{S_t}\rho\mathbf{b}(\mathbf{u}-\mathbf{w})\cdot\mathbf{n}dA \qquad (2.72)$$

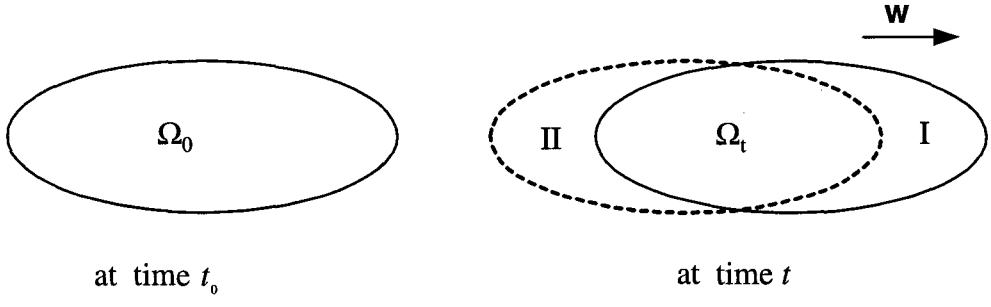

Figure 6 Evolution of a physical quantity of control volume

From the second term of the right hand side of equation (2.72), one can get the following integral formulation using Gauss theorem :

$$\oint_{S_t} \rho \mathbf{b}(\mathbf{u}-\mathbf{w}) \cdot \mathbf{n} dA = \int_{\Omega_t} div(\rho \mathbf{b}(\mathbf{u}-\mathbf{w})) d\Omega_t = \int_{\Omega_0} J div(\rho \mathbf{b}(\mathbf{u}-\mathbf{w})) d\Omega_0 \quad (2.73)$$

The first term on the right hand of equation (2.72) can be written as :

$$\lim_{\Delta t \to 0} \frac{\mathbf{B}_{vc}(t) - \mathbf{B}_{vc}(t_0)}{\Delta t} = \lim_{\Delta t \to 0} \frac{\int_{\Omega_t} \rho \mathbf{b} d\Omega_t - \int_{\Omega_0} \rho \mathbf{b} d\Omega_0}{\Delta t} = \frac{\partial}{\partial t} \int_{\Omega_t} \rho \mathbf{b} d\Omega_t \quad (2.74)$$

where Ω_0 is the domain of control volume at time t_0. Using the relation of geometrical transformation $\Omega_t = J\Omega_0$, where J is the geometric Jacobian transform coefficient, equation (2.74) becomes :

$$\frac{\partial}{\partial t} \int_{\Omega_t} \rho \mathbf{b} d\Omega_t = \frac{\partial}{\partial t} \int_{\Omega_0} \rho \mathbf{b} J d\Omega_0 = \int_{\Omega_0} \frac{\partial(\rho \mathbf{b} J)}{\partial t} d\Omega_0 \quad (2.75)$$

Using the Piola-Kirchoff identity $\partial J/\partial t = J div\mathbf{w}$ [86] (called also "geometric conservation law"), equations (2.72), (2.73), (2.74), (2.75) yield the following conservative equations in ALE description :

$$\boxed{\frac{D}{Dt}\int_{\Omega_t} \rho\mathbf{b}d\Omega_t = \int_{\Omega_t} [\frac{\partial(\rho\mathbf{b})}{\partial t} + div(\rho\mathbf{bu}) - \mathbf{w}\nabla(\rho\mathbf{b})]d\Omega_t} \tag{2.76}$$

If $\mathbf{w} = \mathbf{u}$, the control volume moves with the same speed as the material particles, equation (2.76) represents the Lagrangian description. If $\mathbf{w} = 0$, the control volume is immobile, equation (2.76) represents the Eulerian description.

If $\mathbf{b} = 1$, one obtains the following continuity equation according to the conservation law of mass :

$$\frac{D}{Dt}\int_{\Omega_t} \rho\mathbf{b}d\Omega_t = \int_{\Omega_t} \left(\frac{\partial\rho}{\partial t} + div(\rho\mathbf{u}) - \mathbf{w}\nabla\rho\right) d\Omega_t = 0 \tag{2.77}$$

The equivalent partial differential equation is

$$\boxed{\frac{\partial\rho}{\partial t} + div(\rho\mathbf{u}) - \mathbf{w}\nabla\rho = 0} \tag{2.78}$$

If $\mathbf{b} = \mathbf{u}$, one obtains the following equations of momentum conservation :

$$\frac{D}{Dt}\int_{\Omega_t} \rho\mathbf{u}d\Omega_t = \int_{\Omega_t} \left(\frac{\partial(\rho\mathbf{u})}{\partial t} + div(\rho\mathbf{uu}) - \mathbf{w}\nabla(\rho\mathbf{u})\right) d\Omega_t = \int_{\Omega_t} \rho\mathbf{f}_v d\Omega_t + \oint_{S_t} \mathbf{f}_s dS_t \tag{2.79}$$

where $\mathbf{f}_v$ denotes the volume force vector on the control volume Ω_t, $\mathbf{f}_s$ denotes the pressure and the shear stress denotes force vector on the surface S_t which represents the moving fluid boundary. $\oint_{S_t} \mathbf{f}_s dS_t$ can be transformed into an integration on the volume Ω_t using the following Gauss theorem :

$$\oint_{S_t} \mathbf{f}_s dS_t = \int_{\Omega_t} (-grad(p) + div\boldsymbol{\sigma}) d\Omega_t$$

where p denotes the pressure and $\boldsymbol{\sigma}$ the viscous stress tensor on the surface S_t. Therefore equations (2.79) become

$$\int_{\Omega_t} \left(\frac{\partial(\rho \mathbf{u})}{\partial t} + div(\rho \mathbf{u}\mathbf{u}) - \mathbf{w}\nabla(\rho \mathbf{u}) \right) d\Omega_t = \int_{\Omega_t} (\rho \mathbf{f}_v - grad(p) + div\boldsymbol{\sigma}) d\Omega_t \quad (2.80)$$

The equivalent partial differential equations of equations (2.80) are :

$$\boxed{\frac{\partial(\rho \mathbf{u})}{\partial t} + div(\rho \mathbf{u}\mathbf{u}) - \mathbf{w}\nabla(\rho \mathbf{u}) = \rho \mathbf{f}_v - grad(p) + div\boldsymbol{\sigma}} \quad (2.81)$$

with the Stokes law :

$$\boldsymbol{\sigma} = \lambda(div\mathbf{u})\mathbf{I} + 2\mu\mathbf{D}$$

where μ denotes the dynamic viscosity and λ denotes the second coefficient of viscosity, $\mathbf{D}$ denotes the rate of the strain deformation tensor :

$$\mathbf{D} = \frac{1}{2}\left(\nabla\mathbf{u} + (\nabla\mathbf{u})^T\right)$$

If $\mathbf{b} = e_t$, one can obtain the following energy conservation equation :

$$\frac{D}{Dt}\int_{\Omega_t} \rho e_t d\Omega_t = \int_{\Omega_t} \left(\frac{\partial(\rho e_t)}{\partial t} + div(\rho e_t \mathbf{u}) - \mathbf{w} \cdot \nabla(\rho e_t) \right) d\Omega_t \tag{2.82}$$

$$= \int_{\Omega_t} (\rho \mathbf{f}_v \cdot \mathbf{u} + div(\boldsymbol{\sigma} \cdot \mathbf{u}) - div\mathbf{q}) d\Omega_t$$

where e_t denotes the total specific kinetic energy, $\mathbf{n}$ denotes the normal on the surface S_t of the control volume Ω_t, $\mathbf{q}$ denotes the heat flux described by Fourier law ($\mathbf{q} = -k\nabla T$), where T denotes the temperature and k denotes the conductivity. Therefore, the partial differential equation for total specific kinetic energy becomes :

$$\boxed{\frac{\partial(\rho e_t)}{\partial t} + div(\rho e_t \mathbf{u}) - \mathbf{w} \cdot \nabla(\rho e_t) = \rho \mathbf{f}_v \cdot \mathbf{u} + div(\boldsymbol{\sigma} \cdot \mathbf{u}) - \nabla \cdot (k\nabla T)} \tag{2.83}$$

Equations (2.78), (2.81) and (2.83) are the Navier-Stokes equations described in the ALE kinematic description. For inviscid compressible flow, where no stress tensor exists, the Navier-Stokes equations reduce to the Euler equations.

Remark: The Navier-Stokes equations for unsteady viscous compressible flow model described by equations (2.78), (2.81) and (2.83) in the ALE kinematic description can be written in following compact form [87] :

$$\mathbf{U}_{,t} + \mathbf{F}^{adv}_{i,i} - \mathbf{w}_i \mathbf{U}_{,i} = \mathbf{F}^{diff}_{i,i} + \mathbf{F}^{s} \tag{2.84}$$

where $\mathbf{U}$ denotes the conservative variables vector [61], $\mathbf{U} =< \rho \ \rho\mathbf{u} \ \rho e >^T$, $\mathbf{F}_i^{adv}$, $\mathbf{F}_i^{diff}$ denote respectively the convective flux and the diffusive flux in the ith-space direction as follow :

$$\mathbf{F}_i^{adv} =< \ \rho\mathbf{u}_i \ \ \rho\mathbf{u}\mathbf{u}_i \ \ (\rho e + p)\mathbf{u}_i \ >^T$$
$$\mathbf{F}_i^{diff} =< \ 0 \ \ -\boldsymbol{\sigma} \ \ -\boldsymbol{\sigma}\cdot\mathbf{u} - \lambda\nabla T \ >^T$$

The pressure and the temperature are two additional unknowns which need two more equations to close the equations. The following two equations of states for ideal gas adapted to compressible air are used to close the system of equations due to the additional unknowns p and T :

$$p = (\gamma - 1)\rho C_v T$$

$$T = \frac{E}{\rho} - \frac{|\ \mathbf{u}\ |^2}{2\rho^2}$$

where E ($E = \rho e_t$) denotes the total energy per unit mass, C_v denotes the constant volume specific heat.

2.4 Dynamic mesh model

Since the fluid-structure interface moves, adaptation for fluid mesh is necessary during flow computations. The Eulerian description which is applied to a fixed fluid mesh is no longer valid. As well, the Lagrangian description which is applied to moving domains in structural dynamics, cannot be directly applied. The Arbitrary-Lagrangian-Eulerian (ALE) kinematic description is used for the purpose of adapting the fluid moving boundaries and providing a moving fluid grid without large distortions. Application can be found in other fluid-structure interaction computations and in hydrodynamics with free surfaces [58, 88].

The dynamic mesh is represented by a fictitious linear elastic model. The structural motion is transmitted to the moving fluid boundaries through the fluid-structure interface. Then the motion of the fluid boundaries is distributed into the whole fluid domain by the mesh model.

2.4.1 ALE description

The fluid domain (Figure 7) will be represented by a fictitious linear elastic material for the purpose of establishing the dynamic mesh model which is a purely mathematical one, where the density, elastic modulus and Poisson coefficient have no physical interpretation. The domain closed by Γ_2 represents a structure. The domain closed by Γ_1 and Γ_2 represents the fluid domain. The fluid boundary Γ_2 is a moving boundary due to the structural motion. The fluid boundary Γ_1 is imposed fixed because it is far away from the moving structure. The points near the moving structure will have stronger displacements than the points inside the fluid domain.

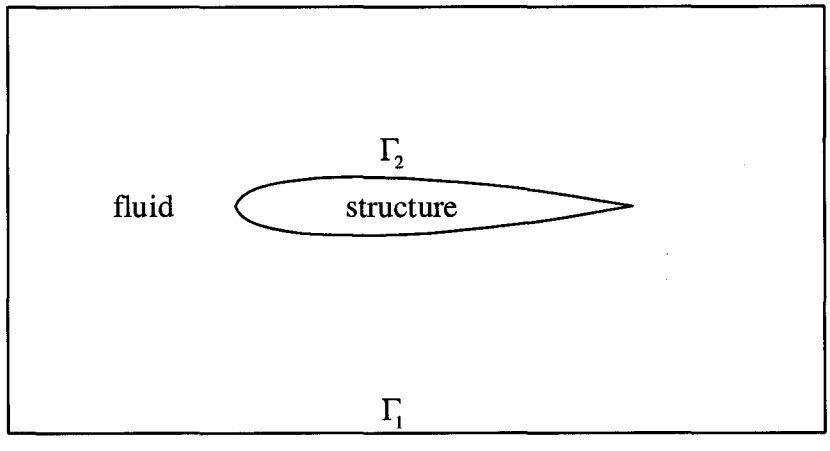

Figure 7 Fluid domain and boundaries conditions

The mathematical equations in 2D or 3D which describe the fluid domain motion can be written as :

$$\frac{\partial \sigma_{ij}(\mathbf{u}^m)}{\partial x_j} = 0 \qquad 1 \leqslant i \leqslant 3, \;\; 1 \leqslant j \leqslant 3 \tag{2.85}$$

with the following boundary conditions :

$$\mathbf{u}^m \mid_{\Gamma_1} = 0 \tag{2.86}$$

$$\mathbf{u}^m \mid_{\Gamma_2} = \mathbf{U}^f(x, y, z, t) \tag{2.87}$$

and

$$\frac{\partial \mathbf{u}^m}{\partial t} \mid_{\Gamma_2} = \frac{\partial \mathbf{U}^f(x, y, z, t)}{\partial t} \tag{2.88}$$

where $\mathbf{U}^f$ is the displacement of the moving fluid-structure interface, $\mathbf{u}^m$ is the displacement vector of the mesh, $\boldsymbol{\sigma}^m$ is the stress tensor of the fictitious elastic material. The body forces of the fictitious elastic material are assumed zero. The properties of linear elastic material give :

$$\{\boldsymbol{\sigma}^m\} = [\mathbf{H}]^m \{\boldsymbol{\varepsilon}^m\} \tag{2.89}$$

with

$$[\mathbf{H}]^m = \frac{E^m}{(1+\nu^m)(1-2\nu^m)} \begin{bmatrix} 1-\nu^m & \nu^m & \nu^m & 0 & 0 & 0 \\ \nu^m & 1-\nu^m & \nu^m & 0 & 0 & 0 \\ \nu^m & \nu^m & 1-\nu^m & 0 & 0 & 0 \\ 0 & 0 & 0 & \frac{1-2\nu^m}{2} & 0 & 0 \\ 0 & 0 & 0 & 0 & \frac{1-2\nu^m}{2} & 0 \\ 0 & 0 & 0 & 0 & 0 & \frac{1-2\nu^m}{2} \end{bmatrix}$$

where ϵ^m is the strain of the material, $[\mathbf{H}]^m$ is the matrix of elastic behavior, E^m is the elastic modulus, ν^m is the Poisson coefficient. They are fictitious parameters. In this thesis, ν^m and E^m are respectively chosen as zero and $2(1 + volume^{-1})$, where $volume$ is the volume of each fluid element.

The strain vector for small structural motion is defined as :

$$\{\epsilon^m\} = \begin{Bmatrix} \frac{\partial u_x^m}{\partial x} \\ \frac{\partial u_y^m}{\partial y} \\ \frac{\partial u_z^m}{\partial z} \\ \frac{\partial u_y^m}{\partial x} + \frac{\partial u_x^m}{\partial y} \\ \frac{\partial u_x^m}{\partial z} + \frac{\partial u_z^m}{\partial x} \\ \frac{\partial u_z^m}{\partial y} + \frac{\partial u_y^m}{\partial z} \end{Bmatrix} \tag{2.90}$$

Therefore from equations (2.89) and (2.90) one obtains the following stress tensor :

$$\{\sigma^m\} = \begin{Bmatrix} H_{11}\dfrac{\partial u_x^m}{\partial x} + H_{12}\dfrac{\partial u_y^m}{\partial y} + H_{13}\dfrac{\partial u_z^m}{\partial z} \\ H_{21}\dfrac{\partial u_x^m}{\partial x} + H_{22}\dfrac{\partial u_y^m}{\partial y} + H_{23}\dfrac{\partial u_z^m}{\partial z} \\ H_{31}\dfrac{\partial u_x^m}{\partial x} + H_{32}\dfrac{\partial u_y^m}{\partial y} + H_{33}\dfrac{\partial u_z^m}{\partial z} \\ H_{44}\left(\dfrac{\partial u_y^m}{\partial x} + \dfrac{\partial u_x^m}{\partial y}\right) \\ H_{55}\left(\dfrac{\partial u_x^m}{\partial z} + \dfrac{\partial u_z^m}{\partial x}\right) \\ H_{66}\left(\dfrac{\partial u_z^m}{\partial y} + \dfrac{\partial u_y^m}{\partial z}\right) \end{Bmatrix} \tag{2.91}$$

Using the finite element method in the Galerkin formulation (see section 3.3.1), one obtains the following discrete formulation :

$$\sum_e \int_{\Omega^e} ([\mathbf{B}^m]^T[\mathbf{H}^m][\mathbf{B}^m]d\Omega^e)\mathbf{u}^{m,e} = \sum_e \mathbf{F}^{m,e} \tag{2.92}$$

where $\mathbf{B}^m$ denotes the deformation matrix associated to the interpolations of displacements, $\mathbf{u}^{m,e}$ denotes the vector of nodal displacement, $\mathbf{F}^{m,e}$ denotes the element loads vector which represents the contribution of the condition of the moving boundary. The solution of this matrix equation represents the fluid nodal displacement vector. The stiffness of the element depends on the matrix $\mathbf{H}^m$ which is determined by the Young's modulus E^m and the Poisson coefficient ν^m. Since the elements near the moving boundary are much smaller, the stiffness of the fictitious material must not be homogenous. If the fictitious material for the mesh is too soft, the elements near the moving boundary will produce a

negative Jacobian determinant. The stiffness is assumed to vary in a manner proportional inversely to the element volume :

$$H_{ij}^{m} \sim \frac{1}{volume^{e}}$$

where H_{ij}^{m} is the entry of the elasticity matrix corresponding to ith row and jth column. Therefore, the elements near the moving boundary are more rigid and their deformations are smaller which keeps the Jacobian determinant of all elements positive.

2.5 Compatibility conditions at the fluid-structure interface

In the previous sections, the structural dynamic, fluid dynamic and mesh models in aeroelasticity computation were described. The fluid-structure interaction occurs only on the moving fluid boundary and the wet structural surface. The coupling between these models are performed by an information transfer through the boundary conditions. The fluid loads are transferred from the fluid domain to the structural domain. The structural motion is transferred from the structural domain to the fluid domain. On the fluid-structure interface, each structural point (wet point) corresponds to a fluid point. The compatibility for CSD model and CFD model of Euler flow at any point on the interface can be described by the following compatibility conditions :

• kinematic conditions :

$$\mathbf{x}^{s} = \mathbf{x}^{m} = \mathbf{x}^{f}$$

$$\mathbf{u}^{s} = \mathbf{u}^{m}$$

$$\left(\frac{\partial \mathbf{u}^{s}}{\partial t} - \mathbf{u} \right) \cdot \mathbf{n} = 0$$

• dynamic compatibility conditions :

$$\boldsymbol{\sigma}_s \cdot \mathbf{n} = -p\mathbf{n} \tag{2.93}$$

where $\mathbf{x}^f$, $\mathbf{x}^m$ and $\mathbf{x}^s$ denote respectively the fluid, mesh and structural positions, $\mathbf{u}$, $\mathbf{u}^m$ and $\mathbf{u}^s$ denote respectively the fluid velocity, the mesh and the structural displacements, $\boldsymbol{\sigma}^s$ denotes the structural stress tensors, p denotes the fluid pressure of the fluid flow, $\mathbf{n}$ denotes the normal of moving fluid boundary. The displacement of the fluid point is equal to the displacement on the corresponding wet structural point. The load on a structural wet point is equal to the load on its corresponding fluid point.

2.6 Summary

Since aeroelasticity consists of structural dynamics and fluid dynamics, information transfer must be performed between the two different physical domains. Furthermore, fluid mesh adaptation is required due to moving fluid boundaries which follow the structural motion. In this chapter, linear structural dynamics applied to thin structure is described. Linear and nonlinear aerodynamics is discussed according to air speed. The conservation equations which describe inviscid fluid flow are written in the framework of the ALE kinematic description. A linear dynamic mesh model for fluid mesh adaptation is introduced.

CHAPTER 3

DISCRETE FORM OF THE GOVERNING EQUATIONS

3.1 Introduction

The structural dynamics and fluid dynamics governing equations stated in chapter 2 are usually solved by numerical methods. The structural dynamic equations are solved using the finite element method. The partial differential equations of fluid dynamics are usually solved by the finite difference method [9, 89], the finite volume method [90] or the finite element method [50, 55, 56, 78]. In this research, the CFD solver is based on the finite element method. A CSD solver based directly on finite element method (CSD-FEM) is implanted in one coupling solver. Another CSD solver with the modal analysis method (CSD-MAM) which is essentially based on the finite element method for the discretization in space is implanted in another coupling solver. Therefore, two numerical computational aeroelasticity solvers are developed. The difference between the two coupling solvers is in the CSD solvers.

The matcher module, CSD, CFD and mesh solvers will be described in this chapter. The algebraic equations generated from the discretization of the finite element method will be presented. The strategies of time discretizations of these linear or nonlinear equations will be stated.

3.2 Discretization of partial differential equations

Numerical solutions for partial differential equations are based on discrete points in space and in time. In the finite element method, a complex space domain can be divided into a number of simple subdomains known as elements. The approximate solutions in these

elements are expressed through the shape functions :

$$\mathbf{u}^h = N_i(x, y, z)\mathbf{u}_i \qquad (x, y, z) \in \Omega^e \tag{3.1}$$

where $\mathbf{u}^h$ is supposed an approximation of the exact solution. $N_i(x, y, z)$ are the shape functions, $\mathbf{u}_i$ is the nodal solution at the discrete point i (known as node i), Ω^e is the elementary domain. Suppose that a partial differential equation is represented by the following equation :

$$L(\mathbf{u}) = 0 \tag{3.2}$$

where L is an operator. Replacing the unknown in this partial differential equation with its approximation of equation (3.1), then multiplying this equation by a weight function, followed by integrating this equation in its elementary domain Ω^e, the partial differential equation (3.2) is transformed into the following approximate integral equation :

$$\int_{\Omega^e} \delta\mathbf{u}^{h*} L(\mathbf{u}^h) d\Omega^e = 0 \tag{3.3}$$

where $\delta\mathbf{u}^{h*}$ is the weight function. If it is approximated on the same basis as $\mathbf{u}^h$, this equation represents the Galerkin finite element method. The summation of all the elements gives the following assembled equation :

$$\sum_{e=1}^{e=n} \int_{\Omega^e} \delta\mathbf{u}^{h*} L(\mathbf{u}^h) d\Omega^e = 0 \tag{3.4}$$

where n is the total number of elements. Finally, the space discretization equation (3.4) gives the following first or second order ordinary differential equations in the form :

$$\mathbf{C}\dot{\mathbf{u}} + \mathbf{K}\mathbf{u} = 0 \tag{3.5}$$

or in the form :

$$\mathbf{M}\ddot{\mathbf{u}} + \mathbf{D}\dot{\mathbf{u}} + \mathbf{K}\mathbf{u} = 0 \tag{3.6}$$

Equations (3.5) and (3.6) can be discretized in time by explicit or implicit schemes. Explicit schemes are limited in time step [27]. The following implicit second order Gear-Scheme [93, 94] is suitable to approximate the time derivative of $\mathbf{u}$:

$$\frac{d\mathbf{u}(t)}{dt} \simeq \frac{3\mathbf{u}(t+\Delta t) - 4\mathbf{u}(t) + \mathbf{u}(t-\Delta t)}{2\Delta t}$$

After time discretization, equations (3.5) and (3.6) become the following equations :

$$\mathbf{A}\mathbf{u}^{n+2} = \mathbf{R}(\mathbf{u}^{n+1}, \mathbf{u}^{n}) \tag{3.7}$$

or

$$\mathbf{A}\mathbf{u}^{n+4} = \mathbf{R}(\mathbf{u}^{n+3}, \mathbf{u}^{n+2}, \mathbf{u}^{n+1}, \mathbf{u}^{n}) \tag{3.8}$$

For nonlinear problems, the matrix $\mathbf{A}$ depends on the unknowns. This matrix has large dimensions, especially for three-dimensional problems. To solve equation (3.7) or (3.8), we use the GMRES algorithm preconditioned by the ILUT matrix factorization. For more details, we refer to [69].

3.3 CSD solver

The CSD solver in this thesis deals with the linear structural dynamics of thin shells. If both the angle of attack and the displacement are small, linear structural dynamics can be applied. Two approaches are investigated in developing CSD solvers. The first one is the finite element discrete method which is commonly used in structural dynamic computations. The second one which uses the modal analysis method is particularly applied to linear structural dynamics dominated by low fundamental natural frequencies.

3.3.1 CSD solver modeled by finite element method with shell elements

Both CSD-MAM and CSD-FEM solvers are developed using the finite element method. In section 2.2, the characteristics of thin shell has been described and finally the following mathematical equation in the continuous medium has been obtained using the principle of virtual work :

$$\int_V \mathbf{u}_q^* \rho \ddot{\mathbf{u}}_q^* dV + \int_V (< \varepsilon_s^* > [\mathbf{H}]\{\varepsilon_s\} + < \gamma_s^* > [\mathbf{G}]\{\gamma_s\}) dV = \mathbf{u}_{p_A}^* \cdot \mathbf{F}_A \tag{3.9}$$

where V is the volume of the structure. After space discretization by the finite element method, equation (3.9) becomes the following algebraic equations (for more details see Appendix) :

$$\mathbf{M}\ddot{\mathbf{u}}(t) + \mathbf{K}\mathbf{u}(t) = \mathbf{F} \tag{3.10}$$

where $\mathbf{u}$ is the nodal displacement vector, $\mathbf{M}$ and $\mathbf{K}$ are mass and stiffness matrices which are symmetrical and positively defined. In this thesis, equations (3.10) are obtained by the finite element method with shell elements $Q4\gamma24$ [77] which are three-dimensional degenerated elements with constant thicknesses, four nodes and six degrees of freedom

per node (Figure 58). Equations (3.10) represent the elastodynamics equations without structural damping. Generally, the structural dynamics with structural damping matrix **D** is described by the following equations :

$$\mathbf{M}\ddot{\mathbf{u}} + \mathbf{D}\dot{\mathbf{u}} + \mathbf{K}\mathbf{u} = \mathbf{F} \tag{3.11}$$

with the following initial conditions for the displacements and the velocities :

$$\mathbf{u}(0) = \mathbf{u}_0 \tag{3.12}$$

$$\dot{\mathbf{u}}(0) = \dot{\mathbf{u}}_0 \tag{3.13}$$

where $\mathbf{u}_0$ and $\dot{\mathbf{u}}_0$ are respectively the initial displacement and velocity vectors. The following initial acceleration can be obtained from equations (3.11) and the above initial conditions.

$$\mathbf{M}\ddot{\mathbf{u}}(0) = \mathbf{F}(0) - \mathbf{D}\dot{\mathbf{u}}(0) - \mathbf{K}\mathbf{u}(0) \tag{3.14}$$

The displacement, velocity and acceleration vectors at different instants can be obtained using a direct time discretization scheme, such as the popular Newmark's algorithm [95] :

$$\mathbf{u}^k = \mathbf{u}^{k-1} + \dot{\mathbf{u}}^{k-1}\Delta t + (\Delta t)^2((1/2 - \beta)\ddot{\mathbf{u}}^{k-1} + \beta\ddot{\mathbf{u}}^k) \tag{3.15}$$

$$\dot{\mathbf{u}}^k = \dot{\mathbf{u}}^{k-1} + \Delta t((1 - \gamma)\ddot{\mathbf{u}}^{k-1} + \gamma\ddot{\mathbf{u}}^k) \tag{3.16}$$

where Δt denotes time step, $\mathbf{u}^{k-1}$, $\dot{\mathbf{u}}^{k-1}$ and $\ddot{\mathbf{u}}^{k-1}$ denote respectively the displacement, velocity and acceleration at instant t^{k-1}, $\mathbf{u}^k$, $\dot{\mathbf{u}}^k$ and $\ddot{\mathbf{u}}^k$ denote respectively the displacement, velocity and acceleration at instant t^k, γ and β are two arbitrary constants. If $\gamma = 0.5$ and

$\beta = 0$, the algorithm represents an explicit scheme which corresponds to a central finite differential scheme. This scheme is stable only if the time step is small enough. In this thesis, γ and β are chosen respectively as 0.5 and 0.25 which represent an implicit scheme which is unconditionally stable. Substituting equations (3.15) and (3.16) into equations (3.11) yields :

$$\bar{\mathbf{K}}\mathbf{u}^k = \mathbf{R}^k \tag{3.17}$$

With

$$\bar{\mathbf{K}} = \mathbf{K} + \frac{4}{(\Delta t)^2}\mathbf{M} + \frac{2}{\Delta t}\mathbf{D} \tag{3.18}$$

$$\mathbf{R}^k = \mathbf{F}^k + \mathbf{M}\left(\frac{4}{(\Delta t)^2}\mathbf{u}^{k-1} + \frac{4}{\Delta t}\dot{\mathbf{u}}^{k-1} + \ddot{\mathbf{u}}^{k-1}\right) + \mathbf{D}\left(\frac{2}{\Delta t}\mathbf{u}^{k-1} + \dot{\mathbf{u}}^{k-1}\right) \tag{3.19}$$

The implicit Newmark algorithm is represented by the following algorithm :

Implicit Newmark algorithm :

1. Initialize displacement $\mathbf{u}(0)$ and velocity $\dot{\mathbf{u}}(0)$ from equations (3.12) and (3.13)
2. Compute mass matrix $\mathbf{M}$
3. Compute initial acceleration $\ddot{\mathbf{u}}(0)$ from equation (3.14)
4. Do $k = 1, ..., n$ (loop between step 4 and step 10)
5. Compute $\mathbf{R}^k$ from equations (3.19)
6. Compute matrix $\bar{\mathbf{K}}^k$ from equations (3.18)
7. Solve equations (3.17) using linear GMRES algorithm with ILUT preconditioner

8. Compute acceleration using equations (3.15) which yields the following equations

$$\ddot{\mathbf{u}}^k = \frac{4}{(\Delta t)^2}(\mathbf{u}^k - \mathbf{u}^{k-1}) + \frac{4}{\Delta t}\dot{\mathbf{u}}^{k-1} - \ddot{\mathbf{u}}^{k-1}$$

9. Compute velocity $\dot{\mathbf{u}}^k$ using equations (3.16)

10. Go to step 4

3.3.2 Newmark algorithm with superposition of limited modes

Since the motion of linear structures is usually dominated by the first natural frequencies, the resolution of CSD model by the modal analysis method is more economical than the direct finite element discrete method. The dynamic response of a linear structure in forced regime can be approached by the superposition of the first m modes $\mathbf{p}_{0i}$ $(i = 1, 2, 3, ..., m)$:

$$\mathbf{u}(t) = \sum_{i=1}^{m} \mathbf{p}_{0i}\mathbf{z} \tag{3.20}$$

where the generalized coordinate vector $\mathbf{z}$ is the solution of the following uncoupled equation :

$$\ddot{z}_i(t) + 2\eta_i\omega_{0i}\dot{z}_i(t) + \omega_{0i}^2 z_i(t) = s_{0i}(t) \qquad (i = 1, 2, ..., m) \tag{3.21}$$

with the following initial conditions :

$$z_i(0) = \mathbf{p}_{0i}^T\mathbf{M}\mathbf{u}_0$$
$$\dot{z}_i(0) = \mathbf{p}_{0i}^T\mathbf{M}\dot{\mathbf{u}}_0$$

where ω_{0i} is the ith natural frequency, η_i is the ith modal damping coefficient, $s_{0i}(t)$ ($s_{0i}(t) = \mathbf{p}_{0i}^T \mathbf{r}(t)$) is the ith component of the load force projected on the modal basis, $\mathbf{u}_0$ and $\dot{\mathbf{u}}_0$ are respectively the initial displacement and the initial velocity.

The analytical solution for the generalized displacement vector $\mathbf{z}$ by time integration is limited in the case where $s_{0i}(t)$ is a simple mathematical function. It is interesting to solve equation (3.21) by the finite difference method. First, the initial displacement vector $\mathbf{u}_0$ and the initial velocity vector $\dot{\mathbf{u}}_0$ are projected in the base generated by the m modal vectors $\mathbf{p}_{0i}$ $(i = 1, 2, 3, ..., m)$ which are extracted during the modal analysis :

$$z_i^0 = z_i(0) = \mathbf{p}_{0i}^T \mathbf{M} \mathbf{u}_0 \tag{3.22}$$

$$\dot{z}_i^0 = \dot{z}_i(0) = \mathbf{p}_{0i}^T \mathbf{M} \dot{\mathbf{u}}_0 \tag{3.23}$$

where $\mathbf{M}$ is the mass matrix of the structure. From equations (3.21), (3.22) and (3.23), one obtains the following initial acceleration :

$$\ddot{z}_i^0(t) = s_{0i}^0 - 2\eta_i \omega_{0i} \dot{z}_i^0 + \omega_{0i}^2 z_i^0 \qquad (i = 1, 2, ..., m) \tag{3.24}$$

where $s_{0i}^0 = s_{0i}(0)$. The solution at current instant t^k is determined by the solution of the precedent instant t^{k-1} using the Taylor expansion [80] :

$$z_i^k = z_i^{k-1} + \Delta t \dot{z}^{k-1} + (1/2 - \beta)(\Delta t)^2 \ddot{z}_i^{k-1} + \beta (\Delta t)^2 \ddot{z}_i^k \tag{3.25}$$

$$\dot{z}_i^k = \dot{z}_i^{k-1} + (1 - \gamma)\Delta t \ddot{z}_i^{k-1} + \gamma \Delta t \ddot{z}_i^k \tag{3.26}$$

where β and γ are two arbitrary constants, z_i^k, $\dot{z}_i^k$, $\ddot{z}_i^k$ are respectively the generalized displacement, velocity and acceleration of mode i at instant t^k, z_i^{k-1}, $\dot{z}_i^{k-1}$, $\ddot{z}_i^{k-1}$ are re-

spectively the generalized displacement, velocity and acceleration of mode i at instant t^{k-1}.

The following acceleration at instant t^k is obtained using the above algorithm and equation (3.21).

$$\ddot{z}_i^k = s_{0i}^k - 2\eta_i\omega_{0i}\dot{z}_i^k + \omega_{0i}^2 z_i^k \tag{3.27}$$

where s_{0i}^k is modal loads at instant t^k which depends on the fluid loads transferred from the CFD solver. Substituting z_i^k and $\dot{z}_i^k$ of equations (3.25) and (3.26) into equation (3.27) yields :

$$\ddot{z}_i^k = \frac{1}{1 + 2\eta_i\omega_{0i}\gamma\Delta t + \omega_{0i}^2\beta(\Delta t)^2} \tag{3.28}$$
$$\left\{s_{0i}^k - 2\eta_i\omega_{0i}[\dot{z}_i^{k-1} + (1-\gamma)\Delta t\ddot{z}_i^{k-1}] + \omega_{0i}^2[z_i^{k-1} + \Delta t\dot{z}_i^{k-1} + (1/2-\beta)(\Delta t)^2\ddot{z}_i^{k-1}]\right\}$$

$\ddot{z}_i^k$ is used to calculate z_i^k and $\dot{z}_i^k$ in equation (3.25) and (3.26) during the next step. Equations (3.22) to (3.28) gives the Newmark algorithm. This algorithm is implicit if both β and γ are not zero.

The structural displacement, velocity and acceleration at instant t^k can be calculated by the modal superposition of the first m modes :

$$\mathbf{u}(t^k) = \sum_{i=1}^{m} z_i^k(t)\mathbf{p}_{0i}$$

$$\dot{\mathbf{u}}(t^k) = \sum_{i=1}^{m} \dot{z}_i^k(t)\mathbf{p}_{0i}$$

$$\ddot{\mathbf{u}}(t^k) = \sum_{i=1}^{m} \ddot{z}_i^k(t)\mathbf{p}_{0i}$$

For the stability of the Newmark algorithm, the values for β and γ are suggested to be chosen in the following stable zone [80] :

$$1/2 \leq \gamma \leq 3/4$$

$$\beta \leq (\gamma + 1/2)^2/4$$

3.4 Equations of fluid flow discretized by the finite element method

The CFD solver used for the computational aeroelasticity solvers is a code developed in the GRANIT laboratory. This code has already been applied in other research [58, 61, 68] with varieties according to the flow feature. In this thesis, the CFD solver is based on an unsteady flow model for inviscid compressible fluid described by nonlinear partial differential equations. The flow is in transonic regime characterized by shock wave and other phenomena. The shock wave is the main issue analyzed in this thesis. Nonlinearity, particularly introduced by shock wave, produces also numerical instabilities. Techniques for stabilizing the numerical solution, such as SUPG [96] and improved SUPG [93] are implemented.

Navier-Stokes equations defined in a domain with moving boundaries are described in section 2.3.4. These equations in compact form are rewritten as :

$$\mathbf{U}_{,t} + \mathbf{F}_{i,i}^{adv} - \mathbf{w}_i \mathbf{U}_{,i} = \mathbf{F}_{i,i}^{diff} + \mathbf{F}_s \tag{3.29}$$

where $\mathbf{U}$ ($\mathbf{U} =< \rho \quad \rho\mathbf{u} \quad E >$) denotes the conservation variables [93], $\mathbf{F}_i^{adv}$, $\mathbf{F}_i^{diff}$ denote respectively the convective flux and the diffusive flux in the ith-space direction, $\mathbf{F}_s$ is the source vector, $\mathbf{u}$ is the conservation variables vector, $\mathbf{w}$ is the grid velocity, the lower comers denote the partial differential and the repeated index indicates a summation. $\mathbf{F}_i^{adv}$, $\mathbf{F}_i^{diff}$ can be written in the following quasi-linear form :

$$\mathbf{A}_i = \frac{\partial \mathbf{F}_i^{adv}}{\partial \mathbf{U}}$$

$$\mathbf{K}_i = \mathbf{F}_i^{diff}$$

The following equations of state for ideal gas provide additional equations to close the Euler equations :

$$p = (\gamma - 1)\rho(E - \frac{|\mathbf{u}|^2}{2})$$

$$T = C_v(E - \frac{|\mathbf{u}|^2}{2})$$

where C_v is the constant volume specific heat, γ is the specific heat ratio.

When equations (3.29) are multiplied by the weight functions $\mathbf{W}$ and integrated over domain Ω, then, applying the Gauss integral theorem yields the following variational formulation :

$$\begin{aligned} &\int_\Omega \mathbf{W} \cdot (\mathbf{U}_{,t} + \mathbf{F}_{i,i}^{adv} - \mathbf{w}_i \mathbf{U}_{,i} - \mathbf{F}_s) d\Omega \\ &+ \int_\Omega \mathbf{W}_{,i} \cdot \mathbf{F}_i^{diff} d\Omega - \int_\Gamma \mathbf{W} \cdot \mathbf{F}_i^{diff} \mathbf{n} d\Gamma = 0 \end{aligned} \tag{3.30}$$

The following residual vector is written as :

$$\mathbf{R}(\mathbf{U}) = \mathbf{U}_{,t} + \mathbf{F}^{adv}_{i,i} - \mathbf{w}_i \mathbf{U}_{,i} - \mathbf{F}^{diff}_{i,i} - \mathbf{F}_s \tag{3.31}$$

This residual is similar to the residual of partial differential equations in Euler kinematic description [62] except for an additional convective term ($-\mathbf{w}_i \mathbf{U}_{,i}$).

The fluid domain is discretized by linear tetrahedral elements [78, 98] which are simple and commonly used while the geometry of the domain is complex. A real element (Figure 8a) can be transformed into a referential element (Figure 8b) which has the following shape functions :

$$N_1(\xi, \eta, \zeta) = 1 - \xi - \eta - \zeta$$

$$N_2(\xi, \eta, \zeta) = \xi$$

$$N_3(\xi, \eta, \zeta) = \eta$$

$$N_4(\xi, \eta, \zeta) = \zeta$$

The vector of unknown variables is approximated by these shape functions :

$$\mathbf{U} = \sum_{k=1}^{4} N_k(\xi, \eta, \zeta) \mathbf{U}_k \tag{3.32}$$

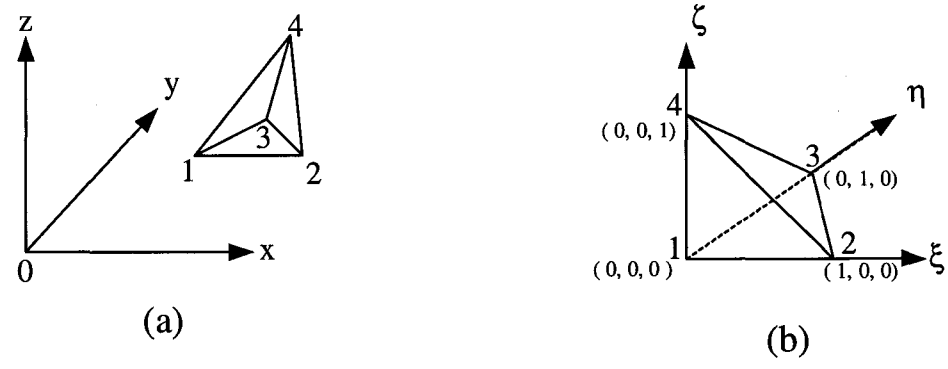

Figure 8 A linear tetrahedral element in real form (a) and referential form (b)

The Galerkin method uses the same shape functions to approximate the following weight functions :

$$\mathbf{W} = \sum_{k=1}^{4} N_k(\xi, \eta, \zeta)\mathbf{W}_k \tag{3.33}$$

The Galerkin finite element formulation often leads to serious numerical instability where the solutions are corrupted by oscillations if the flow is dominated by convection [88]. The SUPG formulation [93, 99] introduces an integral term into the Galerkin variational formulation where the stability inside elements is reinforced by adding the following integral term into equations (3.30) :

$$\sum_e \int_{\Omega_e} A_i^t \mathbf{W}_i \tau R(\mathbf{U}) d\Omega = 0$$

where τ is a matrix of time scale which depends on the element size. For one-dimensional scalar advection dominated flow, one has :

$$\tau = \frac{h}{2a}$$

where h is the element length, a is the flow velocity. For multidimensional flow, the following expression [93] is employed :

$$\tau = (\sum |\widetilde{\mathbf{A}}|)^{-1}$$

A shock capture which depends also on the discrete residual $R(\mathbf{u})$ is added. The shock capture is given by the following expression :

$$\mu_c = C_{k1} h \min(\|\tau R(\mathbf{U})\|, \|\mathbf{u}\|)/2 \tag{3.34}$$

where C_{k1} denotes a tuning parameter. The shock capture adds more dissipation in the vicinity of shocks where the residual $R(\mathbf{u})$ is higher than in smooth zones. After adding the shock capture and the influence term of the far-field boundary conditions, the stabilized variational formulation reads :

$$\begin{aligned}
&\sum_e \int_{\Omega_e} \left[\mathbf{W} \cdot (\mathbf{U}_{,t} + \mathbf{F}^{adv}_{i,i} - \mathbf{w}_i \mathbf{U}_{,i} - \mathbf{F}_s) + \mathbf{W}_{,i} \cdot \mathbf{F}^{diff}_i \right] d\Omega \\
&- \int_{\Gamma_e} \mathbf{W} \cdot \mathbf{F}^{diff}_i \mathbf{n} d\Gamma - \int_{\Gamma_e} \mathbf{W} \cdot \mathbf{A}_{\bar{\mathbf{n}}} (\mathbf{U} - \mathbf{U}_\infty) d\Gamma \\
&+ \sum_e \int_{\Omega_e} \mu_c \nabla \mathbf{W} \cdot \nabla \mathbf{U} d\Omega + \sum_e \int_{\Omega_e} (\mathbf{A}_i - \mathbf{w}_i I)^t \mathbf{W}_{,i} \cdot \tau \cdot \mathbf{R}(\mathbf{U}) d\Omega = 0
\end{aligned} \tag{3.35}$$

where the third integral term is the influence of the far-field boundary conditions. The forth integral term represents the shock capture. The model is completed by adding the

following no-slip boundary conditions for inviscid compressible airflow on the moving fluid boundary :

$$\mathbf{u} \cdot \mathbf{n} = \mathbf{w} \cdot \mathbf{n}$$

where $\mathbf{w}$ is the grid velocity of any node on the moving boundaries, $\mathbf{n}$ is the normal averaged over all elements attached to this node.

The grid velocity for any node is obtained using Gear-Scheme [93, 94] as :

$$\mathbf{w} = \frac{\partial \mathbf{u}^m}{\partial t} = \frac{3\mathbf{x}^{n+1} - 4\mathbf{x}^n + \mathbf{x}^{n-1}}{2\Delta t}$$

where $\mathbf{x}^{n+1}$, $\mathbf{x}^n$ and $\mathbf{x}^{n-1}$ are respectively the coordinates of this node at instants t^{n+1}, t^n and t^{n-1}, Δt is the time step.

Replacing $\mathbf{U}$ and $\mathbf{W}$ in equation (3.35) by equations (3.32) and (3.33) for each element and applying integration over the element yields the following first order semi-discrete equations :

$$\sum_e (\mathbf{C}^e \dot{\mathbf{u}}^e + \mathbf{K}^e \mathbf{u}^e - \mathbf{F}^e = 0)$$

Using time discretization and assembling technique yields a nonlinear system of algebraic equations for the solution of the nodal conservative variables. This nonlinear system is solved at each time step using a matrix-free GMRES algorithm preconditioned by an ILUT factorization [69]. The pressure at each node on the fluid-structure interface is computed using the equations of state. This pressure is transferred to the CSD solver as its prescribed solicitation at the current instant.

3.5 Discrete form of the mesh governing equations

Mesh updating is required in computational aeroelasticity due to the moving boundaries. Moving mesh (see section 2.4.1) is a strategy to distribute the structural motion into the whole fluid domain without large distortion of any fluid element whose connectivity keeps no change during the computation. Only the coordinates of the nodes need to be updated. The fluid domain is considered as a solid with a fictitious elastic material. The displacement of the interior nodes is arbitrary. But the displacements of the far-field nodes are imposed to zero and the nodes on the moving boundaries are imposed to follow the structural motion (see section 3.6.2). The only solicitation is the motion of the moving boundary. Only the displacement and velocity have physical signification since it is a fictitious structural dynamic model.

In the fluid dynamics, the strong gradients of variables, such as pressure, density and velocity are in the zones close to the structure, small elements are required in these zones to obtain the computational accuracy. Since the elements in these zones are close to the moving boundaries, they are more at risk to get crashed. As the elements of the fluid mesh have different sizes, the fictitious material should not have the same stiffness, a small element which should suffer less deformation should be stiffer than the large elements. The mesh motion is defined by the following elasto-static equations [87] :

$$div\boldsymbol{\sigma} = 0 \tag{3.36}$$

where $\boldsymbol{\sigma}$ is fictitious stress tensor. The body forces and the fictitious density are assumed zero. The displacements of the nodes on the far-field boundaries conditions are imposed to zero. The displacement of the moving fluid boundary conditions which follows the structural motion is computed by the matcher module. The relation between the stress tensor and the strain tensor is assumed linear since the displacement of the structure is supposed small. Hook's law gives the following relation between the stress tensor and the

strain tensor ε :

$$\{\sigma\} = [\mathbf{H}]\{\varepsilon\} \tag{3.37}$$

$[\mathbf{H}]$ is defined as functions inversely proportional to the element volume :

$$[\mathbf{H}]^m = \frac{1}{1 + volume} \begin{bmatrix} 2 & 0 & 0 & 0 & 0 & 0 \\ 0 & 2 & 0 & 0 & 0 & 0 \\ 0 & 0 & 2 & 0 & 0 & 0 \\ 0 & 0 & 0 & 1 & 0 & 0 \\ 0 & 0 & 0 & 0 & 1 & 0 \\ 0 & 0 & 0 & 0 & 0 & 1 \end{bmatrix}$$

where *volume* is the element volume. **H** is different from one element to another. The virtual internal work for an element is given as :

$$W^e_{int} = \int_{\Omega_e} < \varepsilon^e >^T \boldsymbol{\sigma} d\Omega = \int_{\Omega_e} < \varepsilon^e >^T [\mathbf{H}]\{\varepsilon\} d\Omega \tag{3.38}$$

where W^e_{int} is the internal work of an element. ε denotes the virtual shear strain. Linear tetrahedral elements are used for the fluid mesh in this thesis. Using the same shape functions for the virtual shear strain and the real shear strain yields the following Galerkin formulation :

$$W^e_{int} = \mathbf{u}^{*e}_n \left(\int_{\Omega_e} [\mathbf{B}]^T [\mathbf{H}][\mathbf{B}] d\Omega \right) \mathbf{u}^e_n \tag{3.39}$$

According to the conservation law of energy, one obtains the following set of assembled algebraic equations :

$$\mathbf{Ku=F} \tag{3.40}$$

where **u** is the solution vector which represents the global nodal displacement, **K** is the symmetric stiffness matrix stored in vector form, **F** is the solicitation vector which represents the displacements of the moving boundaries. Using the linear GMRES algorithm with preconditioner ILUT, where the criterion of the convergence of GMRES resolution is chosen as 1.0^{-8} for the purpose of guaranteeing good accuracy of the mesh motion, the approximate solution of the displacement of the fluid nodes can be obtained. These displacements are used to update the coordinates of fluid nodes and to compute the grid velocities.

3.6 Matcher module for information transfer

In the computational aeroelasticity, information is exchanged on the fluid-structure interface through the boundary conditions. The CFD solver receives the displacement transferred from the CSD solver, which is used to update the coordinates of the moving fluid boundary. On the other hand, the CFD grid on the fluid-structure interface must follow the structural motion. The CSD solver receives aerodynamic loads which are used as structural prescribed forces on the fluid-structure interface. The conservation law of energy must be satisfied during these transfers which are performed through matcher module. If the structural and the fluid meshes have exactly the same grids on the fluid-structure interface, these transfers will be simply performed between fluid nodes and structure nodes. However, the two meshes do not necessarily match on the fluid-structure interface since the two models are usually discretized by different types and sizes of elements. The types of elements are chosen according to the computational criteria and the complexity of the

problems. For example, the structural element may be a quadrilateral and the fluid element may be a triangle. The fluid element size is usually smaller than that of the structural element for the purpose of computational performance, such as for the shock capture. In Figure 9, the CFD mesh on the fluid boundary is composed of triangular elements generated from CFD tetrahedral elements. But the structural mesh is composed of quadrilateral shell elements degenerated from 3D cubic elements. Not only do the nodes not coincide, but also there is a gap between the two grids. Since the fluid and structural nodes on the fluid-structure interface usually do not coincide, the information transfers can not be performed from node to node or from element to element on the fluid-structure interface. A specific technique is required to perform the information transfers. In fact, instead of point to point searching, a search for the associated element of a fluid node is performed since any fluid node on the fluid-structure interface must be associated with a structural element. This procedure of finding the associated structural element of a fluid node is known as pairing. A procedure of surface tracking performs the displacement transfer from the structural mesh to the fluid mesh. Another procedure known as loads projection performs the transfer of aerodynamic loads from the fluid mesh to the structural mesh.

3.6.1 Pairing

Pairing is used to find the corresponding structural element of any fluid node on the fluid-structure interface. Although any node of one grid can be projected on one element of another grid, it is better to perform information transfers between fluid nodes of one grid and structural elements of another grid for non-matching grids. As the fluid element size is usually smaller than the structural element size, if the structural nodes are projected on the fluid grid, some fluid elements may receive no structural projected node. Therefore, the pairing procedure of finding the associated element of a fluid node is performed between one fluid node and one structural element which associates with one or more than one fluid nodes (Figure 10).

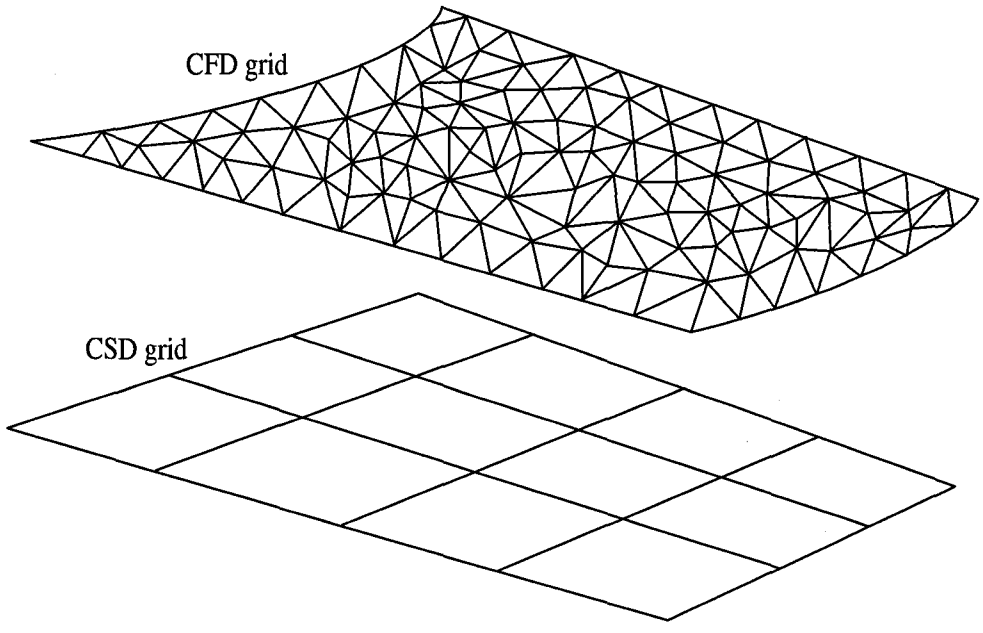

Figure 9 Non-matching grids between fluid and structural meshes

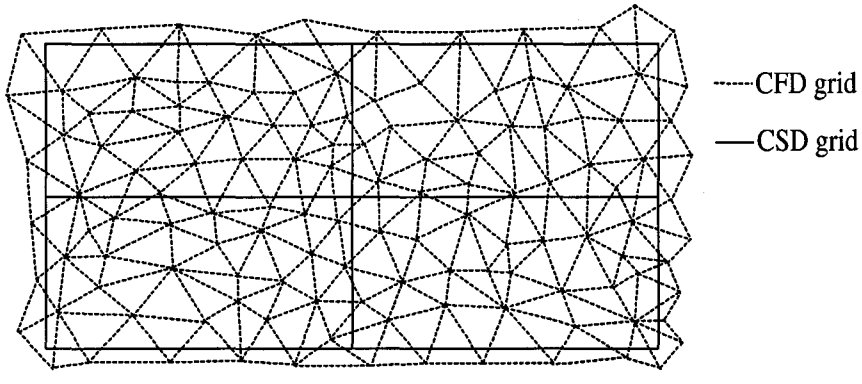

Figure 10 Relation between fluid nodes and structural elements

For a thin structure such as an aircraft wing, where shell element is used, there is only one element in the thickness direction and the shell element nodes are on the middle surface (see section 2.2.1.1). A gap always exists between the structural middle surface and the moving fluid boundary (Figure 11). The distance between each fluid node and its associ-

ated structural element is unchanged during the structural motion, since it is supposed that there is no deformation in the thickness direction (Figure 12).

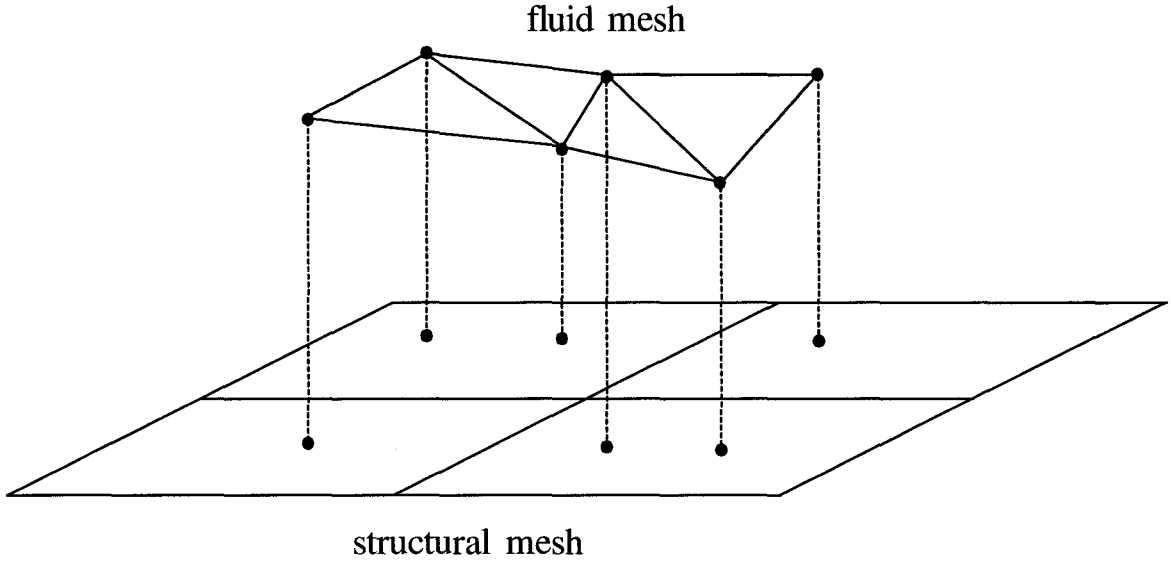

Figure 11 Projecting fluid nodes on the associated structural element

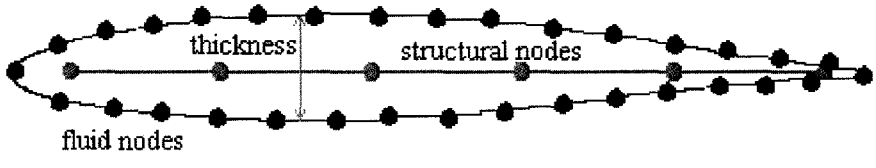

Figure 12 Fluid grid with thin structural elements

A structural quadrilateral can be divided into two triangles (Figure 13). Any point in the global coordinate system can be transformed into a local coordinate system using the following transform matrix. Figure 14 shows an example of a triangular structural

element and a fluid node q which is outside the plane of the triangular element. They can be respectively represented in the global coordinate system and in the local coordinate system.

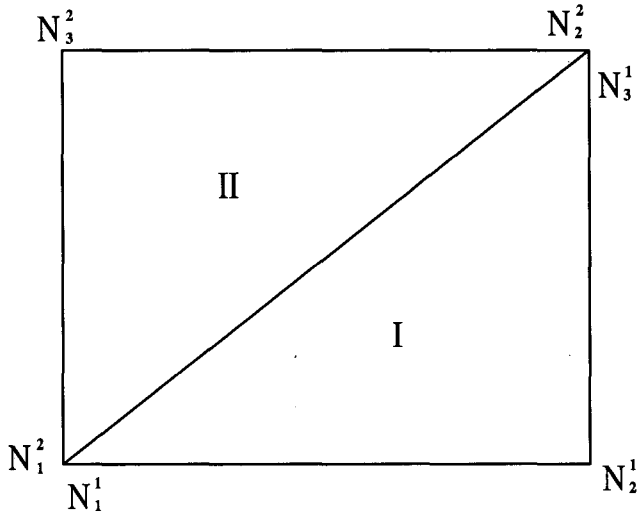

Figure 13 Quadrilateral element split into two triangular elements for pairing

In Figure 14, the coordinates in upper-case letters represent the coordinates in global coordinate system and the coordinates in lower-case letters represent the coordinates in the local coordinate system. The coordinates of point q and the vertexes of the triangle in the local coordinate system can be described as :

$$\begin{Bmatrix} x_i \\ y_i \\ z_i \end{Bmatrix} = [\mathbf{T}] \begin{Bmatrix} X_i \\ Y_i \\ Z_i \end{Bmatrix} \qquad (i = i, j, k, q) \tag{3.41}$$

where **T** denotes the transform matrix :

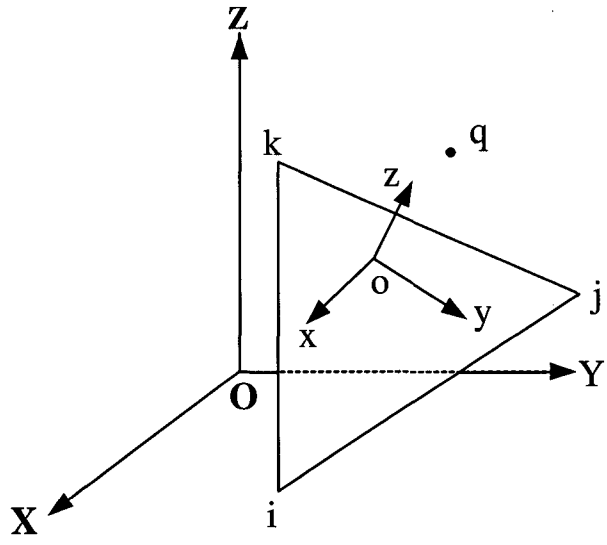

Figure 14 A triangular element and a fluid node in global and local coordinate systems

$$[\mathbf{T}] = \begin{bmatrix} a_1 & b_1 & c_1 \\ a_2 & b_2 & c_2 \\ a_3 & b_3 & c_3 \end{bmatrix}$$

with

$$a_1 = \frac{\mathbf{t}_1}{\|\mathbf{t}_1\|} \cdot \mathbf{i} \qquad b_1 = \frac{\mathbf{t}_1}{\|\mathbf{t}_1\|} \cdot \mathbf{j} \qquad c_1 = \frac{\mathbf{t}_1}{\|\mathbf{t}_1\|} \cdot \mathbf{k}$$

$$a_2 = \frac{\mathbf{t}_2}{\|\mathbf{t}_2\|} \cdot \mathbf{i} \qquad b_2 = \frac{\mathbf{t}_2}{\|\mathbf{t}_2\|} \cdot \mathbf{j} \qquad c_2 = \frac{\mathbf{t}_2}{\|\mathbf{t}_2\|} \cdot \mathbf{k}$$

$$a_3 = \frac{\mathbf{n}}{\|\mathbf{n}\|} \cdot \mathbf{i} \qquad b_3 = \frac{\mathbf{n}}{\|\mathbf{n}\|} \cdot \mathbf{j} \qquad c_3 = \frac{\mathbf{n}}{\|\mathbf{n}\|} \cdot \mathbf{k}$$

where $\mathbf{t}_1$ denotes the unit vector between node i and node j :

$$\mathbf{t}_1 = \frac{(X_j - X_i)\mathbf{i} + (Y_j - Y_i)\mathbf{j} + (Z_j - Z_i)\mathbf{k}}{\sqrt{(X_j - X_i)^2 + (Y_j - Y_i)^2 + (Z_j - Z_i)^2}}$$

another unit vector $\mathbf{t}_{30}$ can be obtained from node i and node k. :

$$\mathbf{t}_{30} = \frac{(X_k - X_j)\mathbf{i} + (Y_k - Y_j)\mathbf{j} + (Z_k - Z_j)\mathbf{k}}{\sqrt{(X_k - X_j)^2 + (Y_k - Y_j)^2 + (Z_k - Z_j)^2}}$$

The vectorial product of $\mathbf{t}_1$ and $\mathbf{t}_{30}$ yields a unit normal vector $\mathbf{n}$ which is perpendicular to $\mathbf{t}_1$:

$$\mathbf{n} = \mathbf{t}_1 \times \mathbf{t}_{30} \tag{3.42}$$

the vector $\mathbf{t}_2$ which is perpendicular to $\mathbf{t}_1$ and $\mathbf{n}$ can be obtained from the vector product of these two vectors :

$$\mathbf{t}_2 = \mathbf{t}_1 \times \mathbf{n} \tag{3.43}$$

In fact, $\mathbf{t}_1$, $\mathbf{t}_2$ and $\mathbf{n}$ represent the directions of x, y, z in the local coordinate system. After the geometric transformation, the triangular element in the local system is in parallel with the xoy plane. The three vertexes of the triangle have the same z coordinate in the local coordinate system. The triangle described in 3D in the global coordinate system is transformed into 2D in the local coordinate system since all points on the triangle have the same value in z direction. Because the distance between the fluid node and its associated structural element is assumed unchanged during the structural motion, the projected point of any fluid node on the triangle is unique. The coordinates (x_g, y_g) of node q in the local coordinate system can be obtained by the above transformation from the fluid node $q(X_g, Y_g, Z_g)$. If the fluid point is associated with one triangular element, the projected point must be inside this triangular element. The condition for point $g(x_g, y_g)$ to be associated with this triangular element is :

$$\min(N_n(x_g, y_g), 1 - N_n(x_g, y_g)) > 0 \qquad (n = i, j, k) \tag{3.44}$$

where $N_i(x_g, y_g), N_j(x_g, y_g), N_k(x_g, y_g)$ are the values of the corresponding shape functions at point (x_g, y_g).

The values of the shape functions of a structural element at the projected point can be computed by the following two steps. First, the point (ξ, η) in the referential bilinear element which corresponds to the projected point can be obtained by solving the following equations :

$$f_1(\xi, \eta) = a_0\xi + a_1\eta + a_0\xi\eta + a_3 - x_g \tag{3.45}$$

$$f_2(\xi, \eta) = b_0\xi + b_1\eta + b_0\xi\eta + b_3 - y_g \tag{3.46}$$

Then, the structural shape functions are obtained by replacing ξ and η in the following structural shape functions by the solutions of equations (3.45) and (3.46) :

$$N_1 = (1-\xi)(1-\eta)/4 \tag{3.47}$$

$$N_2 = (1+\xi)(1-\eta)/4 \tag{3.48}$$

$$N_3 = (1+\xi)(1+\eta)/4 \tag{3.49}$$

$$N_4 = (1-\xi)(1-\eta)/4 \tag{3.50}$$

The pairing procedure performs a loop over all structural elements to find the associated structural element. If the fluid node is not inside this element, the pairing procedure tests the next structural element. If the fluid node is inside the element, the associated element of this fluid node is found and the pairing continues to find the associated structural element for another fluid node. Finally a matrix **pairi**$(m, 6)$ can be constructed. The row of this matrix indicates the local number of the fluid nodes. The first column indicates the global number of the fluid node. The second column indicates the number of its associated

structural element. The other four columns indicate the values of the four structural shape functions at the projected point of the corresponding fluid node.

3.6.2 Surface tracking

The surface tracking ensures the fluid boundary on the fluid-structure interface to follow the structural motion exactly. Since the test case that will be studied is the AGARD 445.6 wing which is a thin shell, only one shell element is needed in the thickness direction. The nodes of a shell element are on the middle surface (see section 2.2.1.1), therefore, there is no contact between the structural nodes and the fluid elements, but a gap between them (Figure 15). Since the wing structure satisfies Reissner/Mindlin hypothesis, a straight line

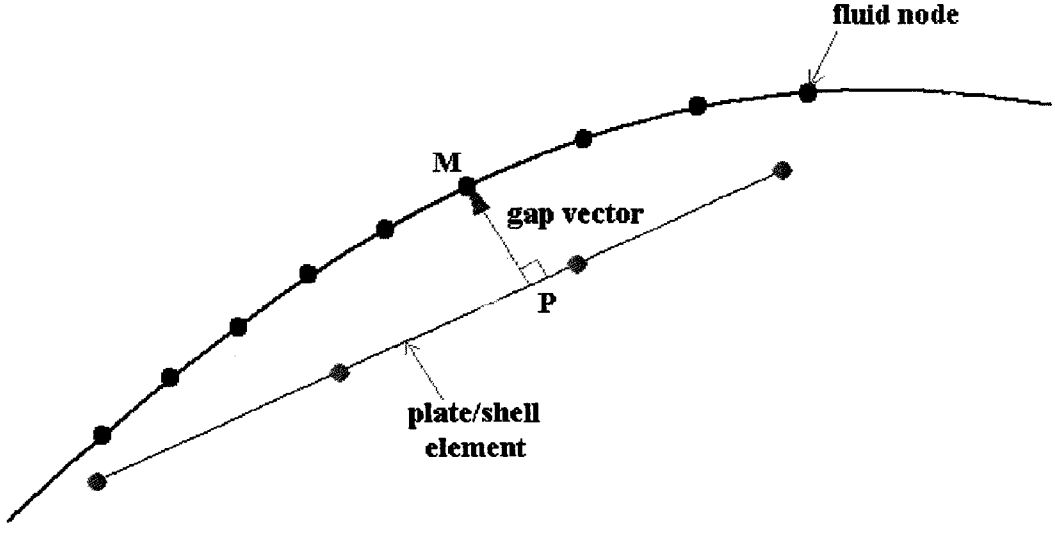

Figure 15 Gap between fluid nodes and structural elements

keeps straight during structural motion. It is supposed that there is no deformation in the thickness direction. The initial distance between a fluid node and its associated structural element is given by :

$$l_0 = \mathbf{n} \cdot (\mathbf{x}^f - \mathbf{x}_g)$$

where $\mathbf{n}$ is the average normal of the structural element, $(\mathbf{x}^f - \mathbf{x}_g)$ is the position difference vector between the position of one of the structural nodes and the fluid node. As the structural surface moves and deforms, this vector rotates and translates. It rotates in the same way as the normal vector of the structural surface. Since it is assumed that the length of this vector never changes during the structural motion, the distance between the fluid node and the structural element keeps constant. Since the fluid and the structural grids are separated with a constant distance, the fluid node position vector can be obtained from the summation of its projected point position vector and a vector which has the same direction of the normal vector of the structural element and has the magnitude of the initial distance between the fluid node and the structural element. Therefore, the updated fluid node position vector is given by :

$$\mathbf{x}^f = \mathbf{x}_p^f + l_0\mathbf{n} = \mathbf{x}_p^f(0) + \mathbf{u}^s + l_0\mathbf{n}$$

where $\mathbf{x}_p^f$ is the projected point position vector of the fluid node, $\mathbf{u}^f$ is the displacement of the fluid node. $\mathbf{x}^f$ is also given by the following equation :

$$\mathbf{x}^f = \mathbf{x}^f(0) + \mathbf{u}^f$$

Since

$$\mathbf{x}^f(0) = \mathbf{x}_p^f(0) + l_0\mathbf{n}$$

one obtains

$$\mathbf{u}^f = \mathbf{u}^s$$

n is given by the following relation :

$$\mathbf{n} = \sum_{i=1}^{4} N_i \mathbf{n}_i / \| \sum_{i=1}^{4} N_i \mathbf{n}_i \|_2$$

where $\mathbf{n}_i (i = 1, 2, 3, 4)$ is the normal vector of structural node i (Figure 16). They are obtained by the following equations :

$$\mathbf{n}_1 = (\mathbf{x}_2 - \mathbf{x}_1)(\mathbf{x}_3 - \mathbf{x}_1) / \| (\mathbf{x}_2 - \mathbf{x}_1)(\mathbf{x}_3 - \mathbf{x}_1) \|_2$$
$$\mathbf{n}_2 = (\mathbf{x}_3 - \mathbf{x}_1)(\mathbf{x}_4 - \mathbf{x}_1) / \| (\mathbf{x}_3 - \mathbf{x}_1)(\mathbf{x}_4 - \mathbf{x}_1) \|_2$$
$$\mathbf{n}_3 = (\mathbf{x}_3 - \mathbf{x}_2)(\mathbf{x}_4 - \mathbf{x}_2) / \| (\mathbf{x}_3 - \mathbf{x}_2)(\mathbf{x}_4 - \mathbf{x}_2) \|_2$$
$$\mathbf{n}_4 = (\mathbf{x}_4 - \mathbf{x}_2)(\mathbf{x}_1 - \mathbf{x}_2) / \| (\mathbf{x}_4 - \mathbf{x}_2)(\mathbf{x}_1 - \mathbf{x}_2) \|_2$$

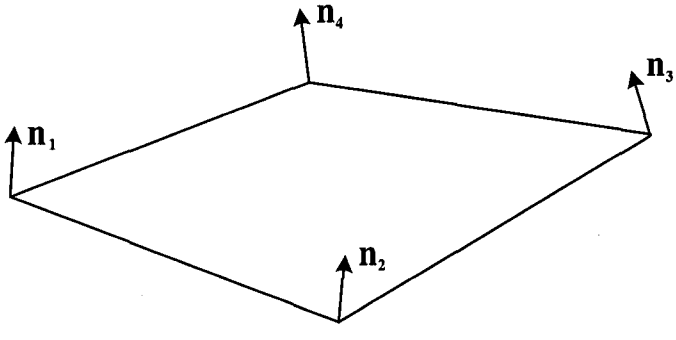

Figure 16 Normal vector of a structural element and its nodal normal

Since the displacement of the fluid point is equal to the displacement of its projected point, the displacement of the projected point of a fluid node can be obtained using the following interpolation of the nodal displacement vectors of its associated structural element :

$$\mathbf{u}_n^f = \mathbf{u}_s(x_g, y_g) = \sum_{m=1}^{m=m_s} N_m^s(x_g, y_g) \mathbf{u}_m^s \tag{3.51}$$

where $\mathbf{u}_n^f$ is the displacement of the projected point of fluid node n, $N_m^s(x_g, y_g)$ is the structural shape function of structural node m at projected point (x_g, y_g) and m_s is the total nodes of the structural element. The coordinates of the fluid node can be obtained by adding the distance of the gap which is the unchanged initial distance between the fluid node and its associated structural element.

3.6.3 Loads projection

The loads projection is performed according to the conservation law of energy which transfers from fluid domain to the structural domain through the fluid-structure interface. The aerodynamic loads induced to the structure by the fluid flow are computed using a fluid dynamic model with loads projection procedure. The displacement of the projected point of the fluid node n is given by equation (3.51). The displacement of any point in the fluid element is interpolated by the shape functions of fluid elements [45] :

$$\mathbf{u}^f = \sum_{n=1}^{n=n_f} N_n^f(x_g, y_g)\mathbf{u}_{f_n} \tag{3.52}$$

where $\mathbf{u}^f$ is the displacement of a point of the fluid element. N_n^f denotes the nth shape function of the fluid element. n_f denotes the total nodes of the fluid element. The work of the fluid tractions on the fluid side Γ_f of the fluid-structure interface can be written as :

$$\delta W^f = \int_{\Gamma_f} (-p\mathbf{n}+\boldsymbol{\sigma}^f\cdot\mathbf{n})\cdot\mathbf{u}^f ds = \sum_{m=1}^{m=m_s}(\sum_{n=1}^{n=n_f}(\int_{\Gamma_f}(-p\mathbf{n}+\boldsymbol{\sigma}^f\cdot\mathbf{n})N_n^f ds))N_m^s\cdot\mathbf{u}_m^s \tag{3.53}$$

The work done by the structural forces of one element on the fluid-structure interface Γ_1 can be written as :

$$\delta W^s = \sum_{m=1}^{m=m_s} \mathbf{f}^s\cdot\mathbf{u}_m^s \tag{3.54}$$

The nodal forces vector of a structural element which is given by the following equation can be considered as the interpolation of the fluid force of each node associated with this structural element.

$$\boxed{\mathbf{f}^s = \sum_{n=1}^{n=n_f} \phi_n N_m^s} \tag{3.55}$$

where ϕ_n denotes the numerical aerodynamic load flux [45] :

$$\boxed{\phi_n = \int_{\Gamma_f} (-p\mathbf{n} + \boldsymbol{\sigma}^f \cdot \mathbf{n}) N_n^f ds}$$

The main point of this procedure is to calculate this numerical force flux. The following section presents the calculation of this term. For simplicity, zero stress tensor is supposed which corresponds to the inviscid compressible flow described by Euler equations and triangular elements are chosen for both fluid and structural meshes.

The numerical force on the surface is always supposed in the inverse direction of the external normal of the fluid element. The magnitude of the numerical force acting on the node j in the local coordinate system (Figure 17) can be described as :

$$\phi_j = -\sum_e \int_{A^e} p N_n^f ds \tag{3.56}$$

where N_n^f is the shape function associated of node j. A^e denotes the surface of the element. p is the pressure on the element which is interpolated linearly as :

$$p = p_i N_i^f + p_j N_j^f + p_k N_k^f$$

where p_i, p_j and p_k are the normal pressure at nodes i, j, k. Therefore, the nodal force in equation (3.56) can be written as :

$$\phi_j = -\sum_e \left(p_i \int_{A^e} N_i^f N_j^f ds + p_j \int_{A^e} N_j^f N_j^f ds + p_k \int_{A^e} N_k^f N_j^f ds \right) \tag{3.57}$$

Since the three nodes have the same coordinate in the z direction in the local coordinate system, the integration on a surface in 3D in the global coordinate system becomes an integration on the same surface represented in 2D in the local coordinate system.

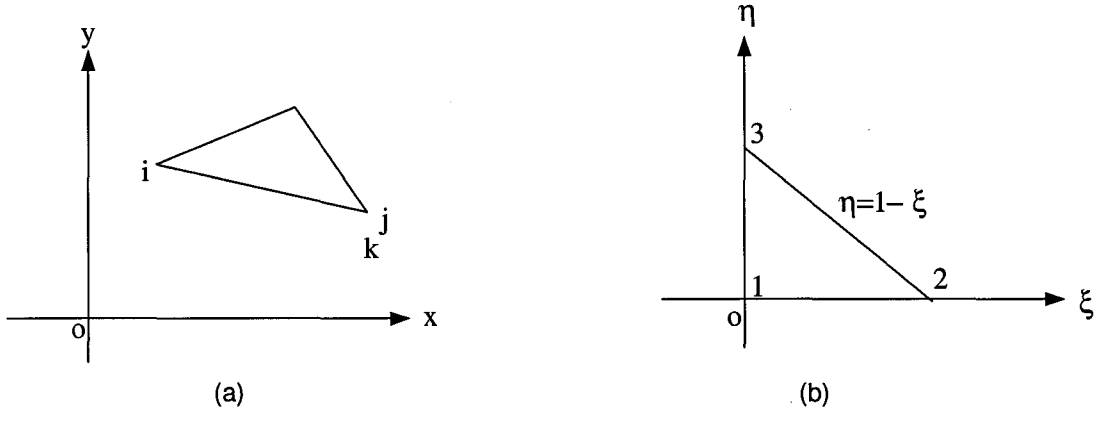

Figure 17 One real element transformed into one reference element

Using the geometrical transformation from a real element to a standard referential element, nodes i, j, k of a real element can be transformed into nodes 1, 2, 3 in a referential element (Figure 17). The integration $\int_{A^e} N_i^f N_j^f ds$ can be written as :

$$\int_{A^e} N_i^f N_j^f ds = \int_0^1 \int_0^{1-\xi} N_1^f(\xi,\eta) N_2^f(\xi,\eta) \det(J) d\eta d\xi$$

where $N_1^f(\xi,\eta)$, $N_2^f(\xi,\eta)$ are respectively the values of the shape functions of nodes 1 and 2 at point (ξ,η) in the referential element. $\det(J)$ is the Jacobian determinant. The shape

functions and the Jacobian determinant are expressed as follow :

$$N_1^f(\xi,\eta) = 1 - \xi - \eta$$

$$N_2^f(\xi,\eta) = \xi$$

$$N_3^f(\xi,\eta) = \eta$$

$$\det(J) = (x_j - x_i)(y_k - y_i) - (x_k - x_i)(y_j - y_i)$$

where A is the area of the triangle, x_i, y_i, x_j, y_j, x_k, y_k are the coordinates of nodes in the local coordinate system. The above integration becomes :

$$\int_{A^e} N_i^f N_j^f ds = 2A \int_0^1 \int_0^{1-\xi} (1 - \xi - \eta)\xi d\eta dxi = A^e/12$$

and the two other integration terms for ϕ_j in equation (3.57) can be written as :

$$\int_{A^e} N_j^f N_j^f ds = 2A \int_0^1 \int_0^{1-\xi} \xi^2 d\eta dxi = 2A^e/12$$

$$\int_{A^e} N_j^f N_k^f ds = 2A \int_0^1 \int_0^{1-\xi} \xi\eta d\eta dxi = A^e/12$$

Similarly, one can obtain ϕ_i and ϕ_k which correspond to the numerical force flux on the nodes i and k. Finally, the nodal force in the local coordinate system can be written as :

$$\begin{Bmatrix} \phi_i \\ \phi_j \\ \phi_k \end{Bmatrix} = \sum_e \frac{A^e}{12} \begin{bmatrix} 2 & 1 & 1 \\ 1 & 2 & 1 \\ 1 & 1 & 2 \end{bmatrix} \begin{Bmatrix} p_i \\ p_j \\ p_k \end{Bmatrix} \tag{3.58}$$

All of the three nodal numerical force flux are normal to the element surface which is in the z direction of the local coordinate system. They are represented in the global coordinate

system as $\boldsymbol{\phi_i} = \phi_i \mathbf{n}_i$, $\boldsymbol{\phi_j} = \phi_j \mathbf{n}_j$, $\boldsymbol{\phi_k} = \phi_k \mathbf{n}_k$, where $\mathbf{n}_i$, $\mathbf{n}_j$ and $\mathbf{n}_k$ are respectively the normal of the fluid nodes i, j and k.

3.7 Summary

Coupling nonlinear aeroelasticity solvers are based on the CSD, CFD and mesh solvers. The coupling is performed between these three solvers through the matcher module. Two computational solvers are detailed in this chapter. The first one is based on a CSD solver with the direct finite element discrete method. The second one is based on the modal analysis method with superposition by limited modes. It is supposed that the nonlinearity of the model is only from the transonic airflow. Therefore, only the CFD solver is based on a nonlinear model. The two CSD solvers are linear models. The mesh solver is also based on a linear model with the hypothesis of moderate grid displacement. The matcher module plays the role of transferring information between the CSD and CFD solver on the fluid-structure interface through the boundary conditions.

CHAPTER 4

FLUID-STRUCTURE COUPLING ALGORITHMS

4.1 Introduction

The discrete forms of the governing equations for each component of the aeroelasticity models are described in the previous chapter. The concept of aeroelasticity solvers deals with the implementation of the strategies of coupling these components which can be considered as independent solvers or modules. In this chapter, the coupling algorithm of the nonlinear computational aeroelasticity solver will be presented.

4.2 Coupling strategies

Aeroelasticity represents the mutual interaction of aerodynamic forces with elastic forces and inertial forces, where airflow passes over flexible structures. The structural deformation plays an important role in determining the external loads on the structure and the fluid flow plays an important role in determining its configuration. Naturally, an aeroelastic system can be considered as a unique system where the governing equations are formulated into only one set of equations. This approach leads to the writing of a whole new code which will become tedious to be modified in the future. For the purpose of developing a comprehensive and efficient code, another approach, which is usually used in modeling of multidisciplinary problems, deals with segregation of a complex system into some subsystems. This approach can reuse the existing solvers with minimal modifications.

Although the fluid dynamics and the structural dynamics in aeroelasticity cannot be considered independent but coupled, the governing equations can be solved in a segregated way at each time instant. Such strategy handles the dependence between the CFD and the CSD solvers in an iterative manner. In the aeroelasticity computation, the aerodynamic

loads and the structural motion are computed using respectively the CFD and the CSD solvers at each time step. Because of the moving fluid boundary and the non-matching between the fluid and the structural grids on the fluid-structure interface, the mesh solver and the matcher module are added in the CFD-CSD coupling (Figure 18). In this figure, the arrows represent the direction of information transfers. The double arrows indicate that the matcher module pilots these information transfers. Aerodynamic loads which transfer from the CFD solver to the CSD solver are piloted by the matcher module through the loads projection. Structural displacements which transfer from the CSD solver to the mesh solver are piloted by the matcher module through the surface tracking. The mesh solver, in its turn, provides updated coordinates and velocities of the fluid mesh to the CFD solver.

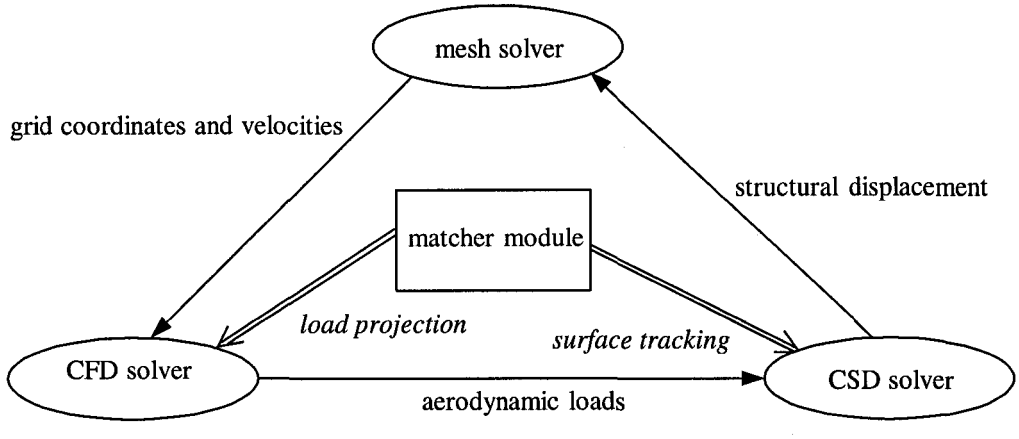

Figure 18 Coupling between CFD, CSD and Mesh Solvers

4.3 A recapitulation of the nonlinear computational aeroelasticity model

The aeroelasticity solvers result from the coupling of the CSD, CFD which are respectively developed for fluid and structural computations. The fluid and structural meshes are cho-

sen by the nature of the models. For example, the structural mesh uses shell elements while the fluid mesh uses tetrahedral elements. The boundary nodes and the interior nodes of the subdomains are two distinct nodes of the structural and fluid meshes. The computational aeroelasticity gives the solutions of the fluid and structural variables inside subdomains and on the boundaries. The CSD solver is in charge of computing the structural motion. The CFD solver is in charge of computing the fluid flow field. The variables are updated alternatively by CFD and CSD solvers. The coupling is performed through the boundary conditions by exchanging information between the CSD and CFD solvers. The models which consist of the nonlinear computational aeroelasticity model in space discretizaton are represented as follows :

CSD model :

$$\mathbf{M}^s\mathbf{u}^s_{,tt} + \mathbf{D}^s\mathbf{u}^s_{,t} + \mathbf{K}^s\mathbf{u}^s = \mathbf{F}^f \tag{4.1}$$

with initial and boundary conditions

Mesh model :

$$\mathbf{K}^m\mathbf{u}^m = \mathbf{F} \tag{4.2}$$

CFD model :

$$\mathbf{M}^f\mathbf{U}^f_{,t} + \mathbf{K}^f(\mathbf{U}^f, \mathbf{w}^f)\mathbf{U}^f = \mathbf{F}^s \tag{4.3}$$

with initial and boundary conditions

Matcher module :

at the fluid-structure interface :

$$\mathbf{u}^s = \mathbf{u}^m \tag{4.4}$$

$$\mathbf{u}^s_{,t} = \mathbf{u}^m_{,t} = \mathbf{u} \tag{4.5}$$

$$\boldsymbol{\sigma}^s_{ij} \cdot \mathbf{n}^s = -p\mathbf{n}^s \tag{4.6}$$

where $\mathbf{U}$ denotes the conservative variables, $\mathbf{u}^s_{,tt}$, $\mathbf{u}^s_{,t}$ and $\mathbf{u}^s$ denote respectively the structural acceleration, velocity and displacement vectors, $\mathbf{u}$ denotes the flow velocity vector, $\mathbf{M}^s$, $\mathbf{D}^s$ and $\mathbf{K}^s$ denote respectively the structural mass, damping and stiffness matrices, $\mathbf{K}^m$ denotes the fictitious stiffness matrix of mesh, $\mathbf{M}^f$ and $\mathbf{K}^f$ denote respectively the structural mass and stiffness matrices of the fluid, $\mathbf{F}^f$ and $\mathbf{F}^s$ denote respectively the aerodynamic loads vector and the sources vector, $\mathbf{u}^m$ denotes the mesh displacement vector, $\mathbf{F}$ is the solicitation vector which represents the displacements of the moving boundaries, $\boldsymbol{\sigma}^s_{ij}$ denotes the structural Cauchy stress tensor, $\mathbf{n}^s$ denotes the unit normal vector of the fluid-structure interface, p denotes the pressure of the fluid. In the CSD model, the external loads vector contains non-zero entries which correspond to the forces of the nodes on the fluid-structure interface. In the mesh model, the grid displacement on the fluid-structure interface is the interpolation of displacement obtained by a surface tracking procedure in the matcher module. In the CFD model, the fluid velocity is obtained using slip boundary conditions for Euler equations which represent inviscid compressible flow. The velocity in the direction normal to the boundary is supposed to be equal to the structural normal velocity. On the far-field boundary, the fluid velocity is imposed to be equal to the velocity of the oncoming flow.

The nonlinear aeroelasticity model resulting from the coupling of the models described by equations from (4.1) to (4.5) can be presented in the following form :

$$\left\{ \begin{array}{c} \mathbf{R}_1(\mathbf{Y},\mathbf{Z}) \\ \mathbf{R}_2(\mathbf{Y},\mathbf{Z}) \end{array} \right\} = 0 \tag{4.7}$$

where $\mathbf{Y}$ is the set of fluid and mesh variables which consist of vectors $\mathbf{U}^f$ and $\mathbf{u}^m$, $\mathbf{Z}$ is the set of structural variables. $\mathbf{R}_1$ and $\mathbf{R}_1$ are respectively the nonlinear functions of the fluid, mesh and structural variables. This system of nonlinear equations can be linearized into the following system of equations :

$$[\mathbf{K}_T] \left\{ \begin{array}{c} \delta\mathbf{Y} \\ \delta\mathbf{Z} \end{array} \right\} = - \left\{ \begin{array}{c} \mathbf{R}_1(\mathbf{Y},\mathbf{Z}) \\ \mathbf{R}_2(\mathbf{Y},\mathbf{Z}) \end{array} \right\} \tag{4.8}$$

where $\mathbf{K}_T$ is the tangent matrix as :

$$[\mathbf{K}_T] = \left[\begin{array}{cc} \mathbf{A} & \mathbf{C} \\ \mathbf{D} & \mathbf{B} \end{array} \right]$$

The solution for equations (4.8) are still difficult to be obtained due to the complexity of the sub-matrices $\mathbf{C}$ and $\mathbf{D}$ which are difficult to express analytically. Therefore, approximate methods are applied through iterative procedures of the segregated approaches.

4.4 Gauss-Seidel coupling algorithm

This coupling algorithm is one of the iterative procedures. Other procedures, such as Jacobi and Schur-complement procedures, can be found in Reference [104]. Gauss-Seidel coupling algorithm is a tight implicit algorithm, where the solution of the CFD solver at instant t^{n+1} is based on the assumption that the solution of the CSD solver at the same

step is already known and vice versa, for the solution of the CSD solver. The procedure of the resolution is performed by resolving iteratively equations (4.8) with the replacement of matrix $\mathbf{K}_T$ by the following matrix :

$$[\mathbf{M}] = \begin{bmatrix} \mathbf{A} & 0 \\ 0 & \mathbf{B} \end{bmatrix}$$

Since the CFD solver applied has ready used an implicit algorithm, it is used to pilot the coupling procedure. The coupling procedure is represented by the following algorithm and the following flow chart (Figure 19) :

Gauss-Seidel coupling Algorithm :

1. Allocate tables for the matcher module, CSD, CFD and mesh solvers
2. Identify the fluid nodes on the fluid-structure interface
3. Identify the associated structural element of each fluid node on this interface by the matcher module
4. Initialize the CFD solver and compute the pressure on the fluid elements of the moving boundary and project these pressures on the associated structural elements
5. Initialize the structural nodal displacements and nodal velocities and compute the nodal accelerations according to the initial displacements, velocities and the external forces on the structural nodes
6. Do the time loop in CFD solver until step 16
7. Apply a structural perturbation or a force distribution on the structure during a time period
8. Do the coupling iterative loop until step 15
9. Call matcher module to perform loads projection and compute structural displacement by calling the CSD solver

10. Compute the displacement of each fluid node on the fluid moving boundary by surface tracking
11. Call mesh solver to compute the nodal displacement of the fluid mesh
12. Update the fluid nodal coordinates and compute the fluid grid velocity using its displacement
13. Update the normal of the triangular fluid elements on the moving boundary and compute the fluid nodal velocities on the moving boundary
14. Compute fluid pressure using GMRES algorithm with ILUT preconditioner
15. End the coupling iterative loop
16. End the time loop
17. Stop

This coupling algorithm is applied to flutter simulations. At step 7, the aeroelasticity system receives a perturbed force on the structure at the first time step.

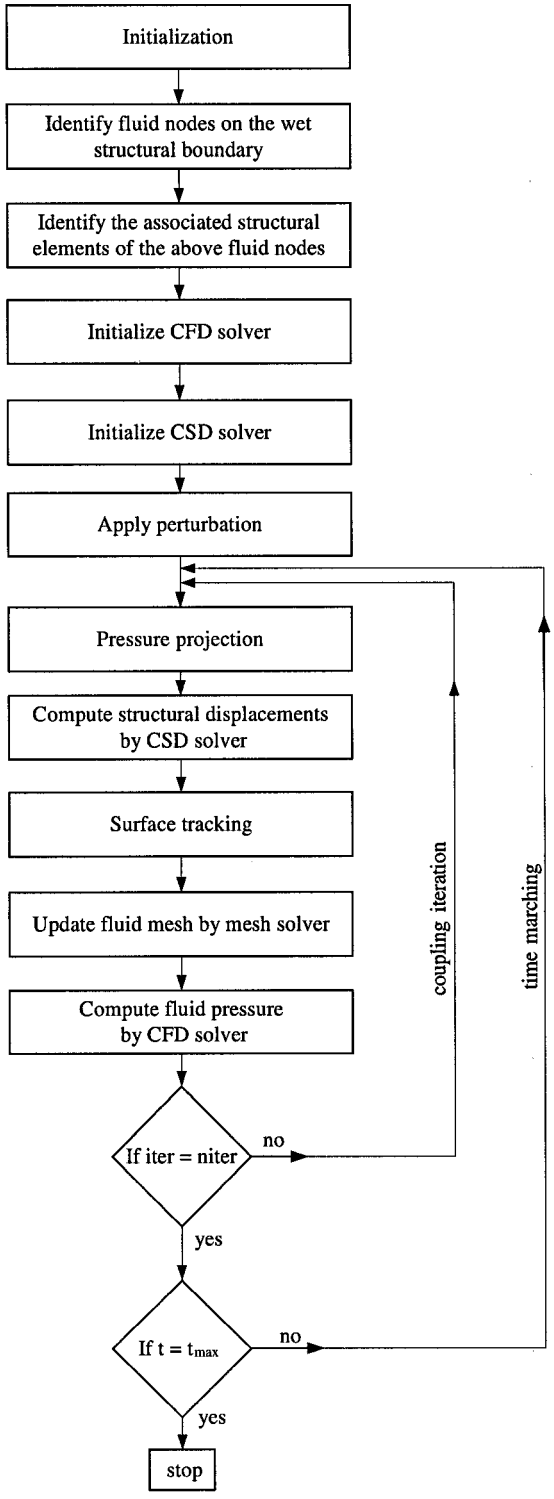

Figure 19 Coupling flow chart

4.5 Variant of the Gauss-Seidel coupling algorithm

This coupling algorithm can yield different staggered coupling procedures. The conventional sequential segregated procedure using one coupling iteration (Figure 20) is briefly described as follows. First, the variables of the structure solver, the mesh solver and CFD solver are initialized, then the initial pressure is sent to the CSD solver by the matcher module and a perturbation is applied on the structure, the CSD solver computes the displacements of the structure and transfers the boundary velocity to the mesh solver by the matcher module. The moving mesh solver computes the velocity of each node of the mesh (grid velocity) using the boundary conditions of the moving boundary obtained from the interpolation of the structural motion, then the mesh solver computes the grid velocity and transfers it to the CFD solver which in its turn computes fluid pressure according to the updated mesh coordinates. The fluid pressure is transferred to the CSD solver by the matcher module.

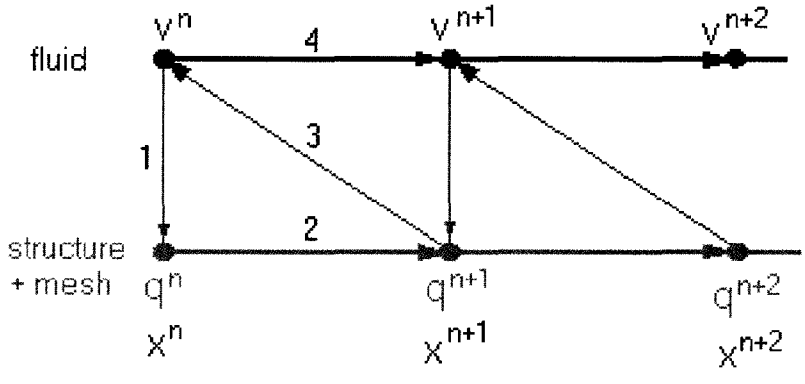

Figure 20 Sequential coupling procedure

For a better coupling, more coupling iterations can be used during each time step (Figure 21). There are some sub-iterations in which the information is transferred between the solvers.

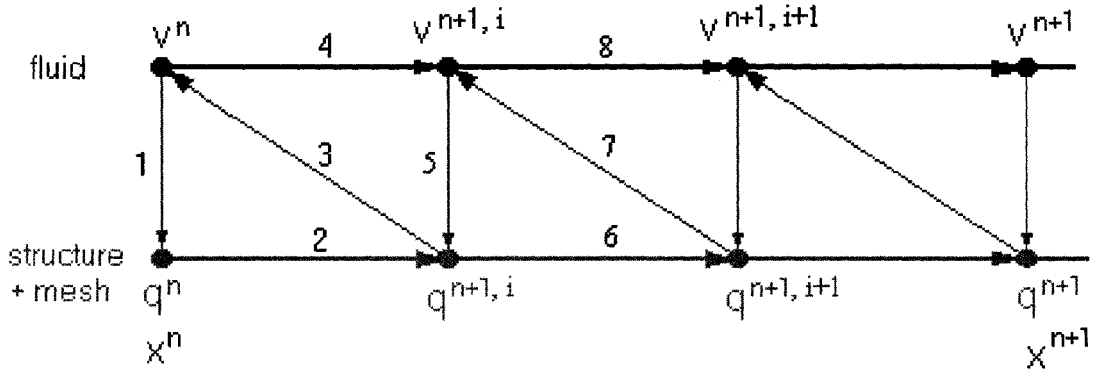

Figure 21 Sequential procedure of Gauss-Seidel algorithm with sub-iterations

The pressure used for the computation of the structural displacement can be chosen as the pressure at the current step.

4.6 Summary

The nonlinear aeroelasticity models are composed of the nonlinear CFD, the linear CSD, mesh solvers and the matcher module. The coupling nonlinear computational aeroelasticity solvers are based on the independent CSD, CFD and mesh solvers. The coupling strategy is based on the segregated procedure using the iterative approximate approach where a time staggering is possible during the computation.

CHAPTER 5

NUMERICAL RESULTS

5.1 Introduction

In the previous chapters, the models of the subsystems and the coupling algorithms for the nonlinear computational aeroelasticity have been described. The corresponding solvers of these subsystems are either reused or developed using appropriate computational techniques. The validation of these subsystems solvers are required except for the CFD solver. Since this solver has already been applied to various research projects in our laboratory, it is ready to be coupled with some moderate modifications to adapt to the moving fluid boundaries. In this chapter, first, numerical experiments are performed on the validation of the CSD-FEM and CSD-MAM solvers. Secondly, the validation will be performed on the coupled solvers between the CSD and mesh solvers through the matcher module to ensure the coupling without the CFD solver. Then, it is focused on the validation of the complete coupled nonlinear computational aeroelasticity solvers based on the solvers of these subsystems. Finally, the coupled solvers will be applied on the AGARD 445.6 aeroelastic wing for flutter simulation.

5.2 Validation of the CSD solvers

In this test, the two CSD solvers are respectively coupled in nonlinear computational aeroelasticity solvers. The CSD-FEM solver uses the general finite element discrete approach while the CSD-MAM solver benefits from the linear structural properties for saving the computing time and reducing the memory requirement. For the CSD-MAM solver, the modal parameters are extracted from ANSYS software since it is a commercial software commonly used in research and industries. The unsteady solution from the CSD-MAM

solver is compared to those obtained from ANSYS software while both of them use the same modal parameters. The second comparison is performed between our developed CSD-MAM and CSD-FEM solvers.

5.2.1 Extraction of natural frequencies and eigenmodes

The natural frequencies and mode vectors can be analytically obtained from the free vibration equations (2.21). For large discrete systems, these modal parameters can be extracted using ANSYS software. They can also be obtained using MATLAB after extracting mass and stiffness matrices from the CSD-FEM solver. The validation of the CSD-FEM model is performed through its comparison with the CSD-MAM model. Suppose that a square plate is clamped on its left side (Figure 24). This plate has a dimension of $10\ cm \times 10\ cm$, a thickness of $0.135\ cm$ with a density of $2710\ kg/m^3$, a Young's modulus of $7.728 \times 10^{10}\ N/m^2$ and a Poisson coefficient of 0.33. As the thickness is small, the deformation in the thickness direction is assumed negligible. The plate is discretized respectively by one and 25 shell elements (Figure 24 and Figure 25). The natural frequencies are represented in table I and table III. Table II and table IV show the deflections of the first mode in the thickness direction. These results indicate that the CSD-FEM model approaches the CSD-MAM model when the mesh is refined.

Table I

Natural frequencies obtained with a mesh of one element

mode	ANSYS (Hz)	CSD-FEM (Hz)
1	114.15	116.86
2	306.16	281.17

Table II

Deflections of the first mode obtained with a mesh of one element

node	ANSYS (m)	CSD-FEM (m)
3	-9.78	-9.05
4	-9.78	-9.05

Table III

Natural frequencies obtained with a mesh of 25 elements

mode	ANSYS (Hz)	CSD-FEM (Hz)
1	121.5	122.2
2	296.8	297.6
3	747.1	808.3
4	952.2	1011.5
5	1089.1	1161.6

Table IV

Deflections of the first mode obtained with a mesh of 25 elements

node	ANSYS (m)	CSD-FEM (m)
31	-10.34	-10.38
32	-10.49	-10.52
33	-10.58	-10.60
34	-10.58	-10.60
35	-10.49	-10.52
36	-10.34	-10.38

5.2.2 Initial acceleration

Since the initial displacement and velocity are imposed to zero, knowledge of the effect of the initial acceleration is important in the computation of the structural displacement. Numerical experiments show that the number of modes used for the superposition affects the initial acceleration. Increasing the number of modes used in the CSD-MAM solver decreases the difference between the initial accelerations obtained by the CSD-MAM and CSD-FEM solvers. Figure 26 shows the initial accelerations of points of one side of the plate under a static force of one Newton in the thickness direction on the upper corner (Figure 24). The difference between the values obtained by the CSD-MAM and CSD-FEM decreases with the increasing of the number of the modes used in the CSD-MAM solver. However, when the mesh is refined, more modes are required to get an initial acceleration close to that obtained by the CSD-FEM solver. Figure 27 shows the initial accelerations of the points on the same side of the plate. The results in Figures 26 and 27 are obtained using respectively a mesh with 25 elements (Figure 25) and another refined mesh with 100 elements which have less difference in natural frequencies (Table V) than that in table III. This numerical test shows that the difference of the accelerations can also be reduced by refining the mesh. This reduction can also be obtained by increasing the number of modes used in the modal superposition approach where the contribution of the higher frequencies is significant in the responses.

5.2.3 Validation of the CSD-MAM and CSD-FEM solvers

The CSD-MAM solver implements the modal analysis approach where the mode vectors and the natural frequencies can be extracted from any structural analysis software, such as the ANSYS software. The validation of this solver is performed by comparing its solutions with those obtained by the ANSYS software. These two CSD models are applied to the example in Reference [80] (Figure 28) which is used as reference in this test case. The plate has a dimension of $50\ cm \times 50\ cm$, a thickness of $0.5\ cm$ with a density of

Table V

Natural frequencies obtained by discretization with 100 elements

mode	ANSYS (Hz)	CSD-FEM (Hz)
1	121.5	121.6
2	294.6	294.5
3	742.7	757.0
4	950.9	964.8
5	1078.9	1093.8

7850 kg/m^3, a Young's modulus of 2.1×10^{11} N/m^2, a Poisson coefficient of 0.3 and a correction factor of shear stress of 0.833. The plate is discretized by 64 shell elements (Figure 29). Each element has four nodes with 6 degrees of freedom per node (three translations and three rotations) in the models of the CSD-MAM and the ANSYS software, but 9 nodes (three degrees of freedom per node : the translation normal to the plate and the two rotations respectively around x and y axes) in the model of Reference [80]. The translations of the 4 sides are imposed to zero as boundary conditions. Figures 30 shows the natural frequencies of the first six modes compared to those from the ANSYS software and those in the reference. Figures 31 to 33 show the vertical nodal displacements of mode 1, 3 and 5 of nodes 38, 39, 40, 41 (Figure 29). For simplicity, only the first three odd mode vectors are illustrated in these figures. A refined mesh shows also the same effect of the refined mesh as in the previous section, that the modal parameters extracted from the CSD-FEM solver approache those of the reference and those extracted from ANSYS software when the mesh is refined. For the dynamic analysis, a step force of 1000 Newtons exerts at point p on the middle surface of the plate which has the following coordinates : $x = 12.5\ cm$ and $y = 30\ cm$. The displacements in the thickness direction of this point are represented in the figures from 34 to 38. In Figure 34, these displacements are respectively computed by the CSD-MAM solver and the ANSYS software. Both tests use the same modal parameters extracted from the ANSYS software. The differences

between the displacements obtained by the two solvers are very small. The two curves are nearly superposed in this figure and are very close to the result in the reference. It shows that the CSD-MAM solver gets nearly the same results as those from the commercial ANSYS software and those in the reference when the modal parameters are extracted from the ANSYS software. The modal parameters can be also exacted from the CSD-FEM solver. The natural frequencies and modes vectors are computed by MATLAB using the mass and stiffness matrices obtained directly from the CSD-FEM solver. There is more difference between the displacements when the modal parameters extracted from the ANSYS software and those extracted from the CSD-FEM solver are used respectively in the CSD-MAM solver (Figure 35). This difference is due to the difference of the modal parameters obtained by different approaches. However, it decreases (Figure 36) when the mesh is refined by a mesh of 256 elements. The results from the CSD-FEM solver, where the finite element discrete method is applied directly, have the same effect as the refined mesh : the displacements in the thickness direction obtained by the CSD-FEM will approach those in Reference [80] and those obtained through the ANSYS software when the mesh is refined (Figures 37 and 38).

Finally, the validation of the CSD solvers is applied to the weakened model 3 of AGARD 445.6 aeroelastic wing [33]. The wing is made with laminated-mahogany and has a mass of $0.1276\ slug$ ($1.86227\ kg$), a Young's modulus of $4.7072\times10^5\ psi$ ($3.2455\times10^9\ N/m^2$), a Poisson coefficient of 0.31, a density of $0.8088\ slug/ft^3$ ($416.86\ kg/m^3$). The wing has a quarter-chord sweepback of 45 degrees and is fixed through its root. Its geometry is shown in Figure 39. The airfoil section is the symmetrical airfoil NACA 65A004 (Figure 40) with its nondimensional coordinates shown in table VI. Since the thickness of the wing is very small, the deformation in the thickness direction is also assumed negligible. The wing is discretized by 1176 quadrilateral shell elements with varying thickness (Figure 41). First, the modal analysis using the ANSYS software yields the modal parameters. The mode vectors provided by the ANSYS software are presented in Figure 42 compared

to those of Reference [102] which is used as the reference in this test. The difference of the modal parameters is also very small, especially for the first mode. Secondly, the natural frequencies and the modal vectors are extracted from the CSD-FEM solver. The comparison of these natural frequencies is shown in table VII. Since the CSD-FEM solver deals only with constant thickness shell elements, the computations of mass and stiffness matrices are performed using an average value of the four nodal thicknesses which yields more difference compared to the natural frequencies in the reference. Figure 43 shows the displacement in the thickness direction of one node (node 1250 in Figure 41) which is located on the point of the intersection between the tip and the leading edge, on which a Dirac force of 100 Newtons is exerted during the first one millisecond. The wing is initialized with zero displacement and zero velocity. The difference of these displacements obtained by the CSD-MAM solver using respectively the modal parameters extracted from ANSYS software and those obtained from the CSD-FEM solver are less than 5% which is from the difference of the models.

Remark 1 : The modal parameters and the initial acceleration are affected by the element size. The results obtained by the CSD solvers agree better if the mesh is refined. The CSD-MAM solver can give excellent results compared to those of the references when the same modal parameters are used. The results are still satisfying when this CSD solver uses the modal parameters extracted from the CSD-FEM solver. The results from CSD-MAM solver agree with those from the CSD-FEM solver when the mesh is refined.

Remark 2 : Modal analysis gives good results and high computing performance when the first few modes dominate the structural dynamic behavior. However, when high frequency modes play a non-negligible role, then a direct finite element analysis is required, such as the case of structural vibrations induced by a separated flow.

5.3 Coupling validation between the CSD and mesh solvers through the matcher

Before the validation of the complete coupling model between the CSD, CFD and mesh solvers through the matcher module, the next step is to validate the coupling of these components without the intervention of the CFD solver. This validation is performed through the following example where a fluid flow passes over a panel which is clamped at both ends (Figure 44). The fluid domain has dimensions of $0.1\ m \times 0.5\ m \times 1.5\ m$. The panel has a length of $0.5\ m$, a width of $0.1\ m$, a uniform thickness of $1.35 \times 10^{-3}\ m$, a Young modulus of $7.728 \times 10^{10}\ N/m^2$, a Poisson coefficient of 0.33 and a density of $2710\ kg/m^3$. Since the thickness of the panel is also very small, the deformation in the thickness direction is negligible, so shell elements are used for the structural model. The plate is discretized by a mesh of 500 quadrilateral shell elements with 561 nodes (11 rows and 51 columns). The natural frequencies and mode vectors (Figure 45) are extracted from the ANSYS software. The plate is initialized in a horizontal position with zero displacement and zero velocity. The fluid boundaries are imposed to be fixed, except the boundary in contact with the plate where the displacement is interpolated by the displacement of the plate through the matcher module. The structural damping is supposed to be 0.02. A concentrated force of 1000 Newtons applied on the center of the plate during the first one millisecond triggers the structural motion and the system starts the oscillation. The fluid mesh gets the same oscillating motion, and finally after 3 seconds the oscillating motion disappears. Figure 46 shows the position of the deformed plate at an instant after the application of an external force and its initial position. The results show that the fluid mesh (triangular elements in green color) on the interface follows exactly the structural motion (motion of the quadrilateral elements in red color). Figures 47 and 48 show respectively the mesh motion at its initial position and at another position after 0.15 seconds. The motion of the moving fluid boundary diffuses smoothly into the whole fluid domain towards its far-field boundaries.

Remark : Describing the mesh as an elastic media helps distributing interface displacement into the interior domain.

5.4 Validation of the nonlinear computational aeroelasticity solver

As the CFD solver has been a solver already validated in our laboratory and all the other solvers and the matcher module are validated in the previous sections, the complete nonlinear computational aeroelasticity solver can be validated. This validation is performed on the AGARD 445.6 aeroelastic wing which is mounted by its root (see Section 5.2.3) with zero angle of attack, zero initial displacement and velocity.

The wing is immersed in a fluid domain which is discretized by a coarse mesh composed of 177042 linear tetrahedral elements with 37965 nodes. The wing has the same structural mesh of AGARD 445.6 wing in section 5.2.3. Since the strongest variation of the fluid variables occurs around the wing, the mesh near the wing is much finer than in the rest of the fluid domain. There are 12921 fluid nodes of 25684 triangular elements on the wet surface of the wing on which slip boundary conditions are applied. The uniform oncoming flow which is a high transonic flow with a prescribed Mach number is applied on the entrance boundary. The boundary conditions on the far-field boundaries are imposed with the oncoming flow. The fluid variables are initialized with a solution of the CFD solver while the wing is considered as a rigid structure. The corresponding fluid configuration is considered as the initial state of the mesh for the unsteady simulation. From this state, the nonlinear computational aeroelasticity model receives a structural or load perturbation during a short period. The application of different types of perturbation is for the purpose of investigating the performance of the solvers. This perturbation triggers the fluid-structure interaction which results in wing vibrations. This deformation alters the fluid configuration. The change of the fluid configuration, in its turn, perturbs the dynamic pressure on the wing. The Mach number of the oncoming flow is chosen as 0.96 in order to simulate the critical point of the transonic dip. The effects of the time step and the

number of the coupling iteration are investigated in order to build a robust and efficient solver with large time step and small number of coupling iterations.

5.4.1 Responses of the aeroelasticity solver coupled with CSD-MAM/CSD-FEM

The CSD-MAM and the CSD-FEM solvers give structural displacements with little difference when a prescribed forces is applied on the wing. In the numerical experiments of this section, the wing is immersed in an airflow with Mach number of 0.96 and a reference aerodynamic pressure of 62 $lb/sqft$. A perturbation of a structural deformation of 0.5% of the wing's first mode is applied on the wing during a period, then this perturbation is released. Under this structural perturbation, the wing starts oscillation. These experiments are performed using respectively the CSD-MAM and the CSD-FEM solvers in the coupling algorithm. Figure 50 shows the lifts in these two cases. The difference of the results obtained by the two solvers with the two different coupled CSD solvers is very small. This difference is produced by the elimination of the mode vectors with high natural frequencies in the modal approach. This shows that the complete aeroelasticity solver where the linear CSD-MAM solver is coupled is able to represent the nonlinear aeroealasticity system while the structure is assumed linear. The coupling performed respectively with the two CSD solvers has proved the reutilization of the developed solvers.

5.4.2 Effects of the time step and the number of coupling iterations

The time step and the number of coupling iterations affect the computing time. A code with less coupling iterations and large time step provides a software with a higher performance. In the following numerical experiments to investigate the effects of the time step and the number of coupling iteration, a load perturbation is applied instead of a structural perturbation. A Dirac force of 100 Newtons is applied on the point at the intersection between the tip and the leading edge (node 1250 in Figure 41) as in section 5.2.3. This perturbation is exerted for a small period of time (during the first step of the computation).

The aerodynamic pressure on the wing skin is taken from the current pressure. Since the coupling iterations are the feedback of the communicated information between the CSD and CFD solvers, the time history of the generalized displacement of the first two modes in Figure 51 shows that with one coupling iteration (without feedback of information) the model provides an unstable solution. However, the solution is stable when the code uses 3 coupling iterations. Figures 52 and 53 show the time histories of the lift and the generalized displacements of the first two modes in the thickness direction with different time step and number of coupling iterations which characterize the performance of the codes. Only the generalized displacements of the first two modes are illustrated since the solutions are dominated by the first two modes, the contributions to the responses from the other modes are nearly negligible after a short period from the start of the tests. With 3 coupling iterations, the simulations provide the same critical flutter responses until the nondimensional time step increases to 0.3. However, as nondimensional time step keeps increasing, it is difficult to capture correctly the behavior of the modes. When the nondimensional time step increases to 0.3, the model yields flutter results with one coupling iteration and damping results with 3 coupling iterations which do not represent the real behavior of the system.

Remark : The CSD-MAM solver is able to represent the structural behaviors while the structure is assumed linear. The nonlinear computational aeroelasticity solver is capable of performing simulations using nondimensional time of 0.2 with 3 coupling iterations.

5.5 Applications to the AGARD 445.6 aeroelastic wing

In all of the previous sections, the first-order Euler-Scheme for the time discretization is used in the code. For the purpose of improving the performance of the code, this scheme which limits the accuracy of a time dependent solution is replaced by the second-order Gear-Scheme (see section 3.2). The simulations are performed on the AGARD 445.6 aeroelastic wing with the similar conditions of the previous section : the wing with zero

angle of attack which is immersed in an airflow of Mach number of 0.96 receives a perturbation of a Dirac force during the first time step. Different aerodynamic pressures of the oncoming flow are investigated to capture the critical flutter point and different time steps are used to get a higher performance of the code.

First, for the purpose to capture of the critical flutter point with a good accuracy, a relatively small nondimensional time step of 0.1 which corresponds to a real time step of 2.01×10^{-4} *seconds* is used in the numerical simulations. At the aerodynamic pressure of 60 $lb/sqft$ of the oncoming flow, the responses of the lift and the generalized displacements of the first two modes which dominate the responses of the structural displacements have nearly constant amplitudes and the critical flutter is considered captured (Figure 54). When the aerodynamic pressure of the oncoming flow increases to 61.3 $lb/sqft$, the responses of the wing get increasing amplitudes which are beyond the flutter point (Figure 54). Secondly, for the purpose of reducing the computing time, the simulations with the same aerodynamic pressures, but with a nondimensional time step of 0.3 are performed and the results are shown in Figure 55 which give the same conclusion. The computed frequencies f_d and the damping coefficients ζ of the responses of the lift and the generalized displacements of the first two modes are given by the following equations :

$$f_d = \frac{n}{T_t}$$

$$\zeta = \frac{\delta}{\sqrt{4\pi^2 + \delta^2}}$$

with

$$\delta = \frac{1}{n} \ln \left(\frac{x(t)}{x(t + T_t)} \right)$$

$$T_t = nT$$

where T is the period of the oscillation, n is the number of the periods taken in the calculation to increase the accuracy, $x(t)$ and $x(t + nT)$ are respectively the first and last peaks of the responses. The damping coefficients and the frequencies of the oscillation of the lift and the generalized displacements of the first two modes are summarized in Figure 22. The computed frequency of about 13.6 Hz (85.45 $radians/sec$) at aerodynamic pressure of 61.3 $lb/sqft$ with Mach number of 0.96 is very close to the experimental one of 13.9 Hz (87.3 $radians/sec$) of the weak model 3 in Ref. [33] in Figure 23. In simulation 1 and 3 where the aerodynamic pressure of the oncoming flow is 60 $lb/sqft$, the damping coefficients are very small positive or negative values. In these cases with nearly zero damping and equal oscillating frequencies of the first two modes (Figure 56), it is considered that the wing has reached the critical flutter. In simulation 2 and simulation 4 where the aerodynamic pressure has increased to 61.3 $lb/sqft$, the responses of the generalized displacements of the first two modes of the wing begin to get increasing amplitudes and the difference of the frequencies of the oscillation begins to increase. Even though they are still small, the increasing oscillations of the responses of the wing have moved away from those of the critical flutter point. This can be seen from the increased values of the damping coefficients of the lift, the generalized displacements of the two first modes and from the slight increasing oscillations of the responses in Figure 57.

Remark : The second-order scheme for the time discretization has better performance than the first-order scheme. The flutter at Mach number of 0.96 is captured at the aerodynamic pressure of 60 $lb/sqft$ of the oncoming flow with a nondimensional time step of 0.1. Higher performance which reduces the computing time is reached with a nondimensional time step of 0.3.

5.6 Summary

In this chapter, the validation of the coupled solvers is described by steps from the validation of the CSD solver to the whole coupled solvers. First, the validation of the CSD solvers shows good results compared to those in the references. Then, the validation of the coupled system without the intervention of the CSD solver has ensured that the mesh solver and the matcher module work well. Finally, the complete nonlinear computational aeroelasticity coupling solvers are validated and numerical simulations give satisfying results compared to the experimental data in the references.

Table VI

Nondimensional coordinates of airfoil NACA 65A004

x	y
0.0	0.0
0.005	0.00304
0.0075	0.00368
0.0125	0.00469
0.025	0.00647
0.05	0.00875
0.075	0.01059
0.1	0.01213
0.15	0.01459
0.2	0.01645
0.25	0.01788
0.3	0.01892
0.35	0.01962
0.4	0.01997
0.45	0.01996
0.5	0.01954
0.55	0.01868
0.6	0.01743
0.65	0.01586
0.7	0.01402
0.75	0.01195
0.8	0.00967
0.85	0.00729
0.9	0.0025
0.95	0.0049
1.0	0.00009

Table VII

Natural frequencies (Hz) for AGARD 445.6 from ANSYS software

Mode	Values from ANSYS software	Values from CSD-FEM	Values of Yate
1	9.6001	9.7601	9.5990
2	39.4191	45.4378	38.1650
3	49.6013	71.5621	48.3482
4	96.0949	112.7300	91.5448
5	126.2996	174.4325	118.1130

Nondimensional time step		P_ref = 60 lb/sqft			P_ref = 61.3 lb/sqft		
	No. of test	simulation 1			simulation 2		
		lift	mode 1	mode 2	lift	mode 1	mode 2
	damping	0.00063	0.00063	0.00065	-0.0054	-0.00477	-0.00375
	Freq (Hz)	13.51	13.53	13.53	13.75	13.6	13.63
0.1	state	**calculated flutter point**			flutter with a small increasing amplitude		
	No. of simulation	simulation 3			simulation 4		
		lift	mode 1	mode 2	lift	mode 1	mode 2
	damping	-0.0002	-0.00017	-0.00025	-0.00537	-0.00475	-0.00667
	Freq (Hz)	13.52	13.52	13.52	13.58	13.58	13.6
0.3	state	**calculated flutter point**			flutter with a small increasing amplitude		

Figure 22 Frequencies and damping coefficients of the oscillations of wing AGARD 445.6

Model description				M	ρ, slugs/cu ft	$\bar{\mu}$	ω_α, radians/sec	ω_h, radians/sec	V, ft/sec	q, lb/sq ft	$\frac{V}{b_a \omega_\alpha \sqrt{\bar{\mu}}}$
Panel span, ft	Mounting	Structure	Model								
1.250	Wall	Solid	*1	0.480	0.00208	19.250	620.6	-----	540.83	306.8	0.4333
			*1	.470	.00209	19.158	620.6	-----	550.05	295.4	.4256
2.500	Wall	Solid	1	.451	.00216	14.455	298.7	194.1	507.8	279.6	.4879
			1	.463	.00209	14.939	298.7	192.2	522.9	288.0	.4942
2.500	Wall	Weakened	1	.850	.000155	193.150	219.2	94.2	977.8	64.2	.5502
			1	.870	.000155	193.150	219.2	96.7	933.5	66.2	.5343
			2	.854	.000806	144.550	211.7	107.4	901.1	82.7	.5865
			3	.901	.000193	145.920	259.3	101.1	979.4	89.3	.5700
			3	.678	.000404	68.755	259.3	113.0	759.1	115.7	.4174
			3	.499	.000850	33.465	259.3	128.1	565.8	133.1	.4459
			3	.954	.000125	225.820	259.3	91.1	1,008.4	60.6	.5059
			3	.960	.000125	225.820	259.3	87.3	1,013.8	61.3	.5076
			3	.957	.000125	225.820	259.3	87.9	1,020.2	61.7	.5093
			3	1.072	.000107	259.590	259.3	86.7	1,131.0	66.1	.5201
			3	1.141	.000152	182.740	259.3	109.9	1,195.3	105.3	.4031
			4	.338	.00221	12.568	258.0	137.5	383.4	163.9	.4958
3.750	Wall	Solid	1	.496	.00194	17.055	202.9	125.6	569.0	316.0	.4938
1.167	Sting	Solid	Right panel	.466	.00199	20.291	608.97	409.9	589.0	282.5	.4500
			Right panel	.458	.00202	19.989	608.97	408.2	524.5	279.6	.4496

Figure 23 Flutter data measured in air (extracted from Ref. [33])

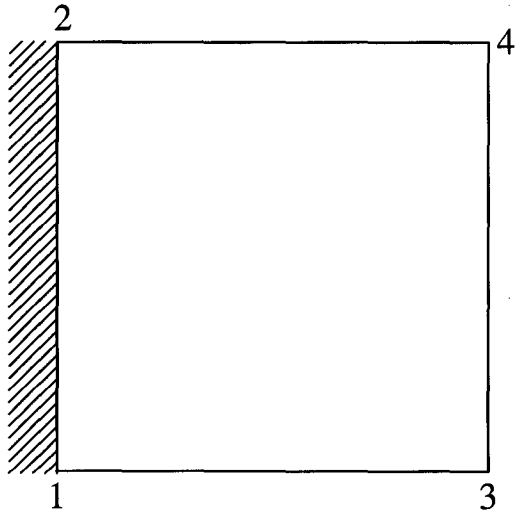

Figure 24 Plate discretized by one element

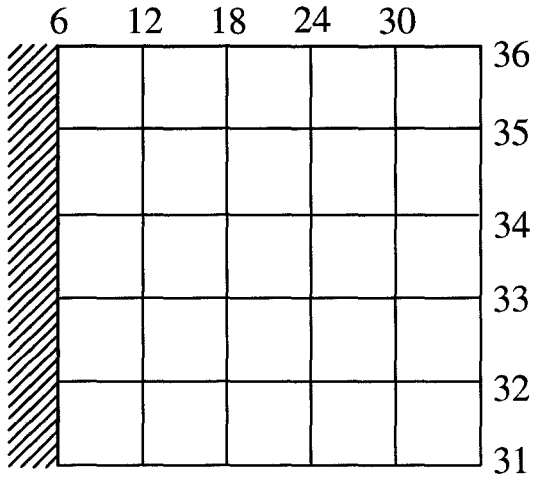

Figure 25 Plate discretized by 25 elements

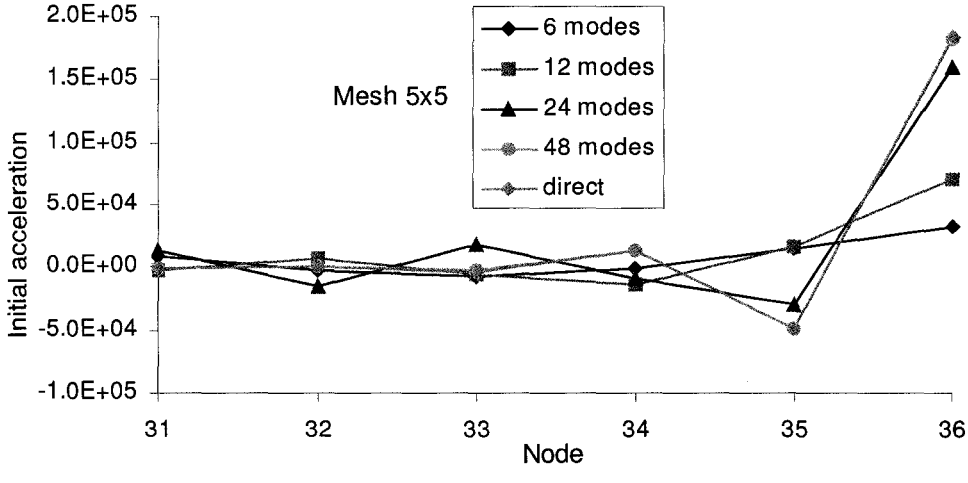

Figure 26 Initial accelerations of the free side under a static force

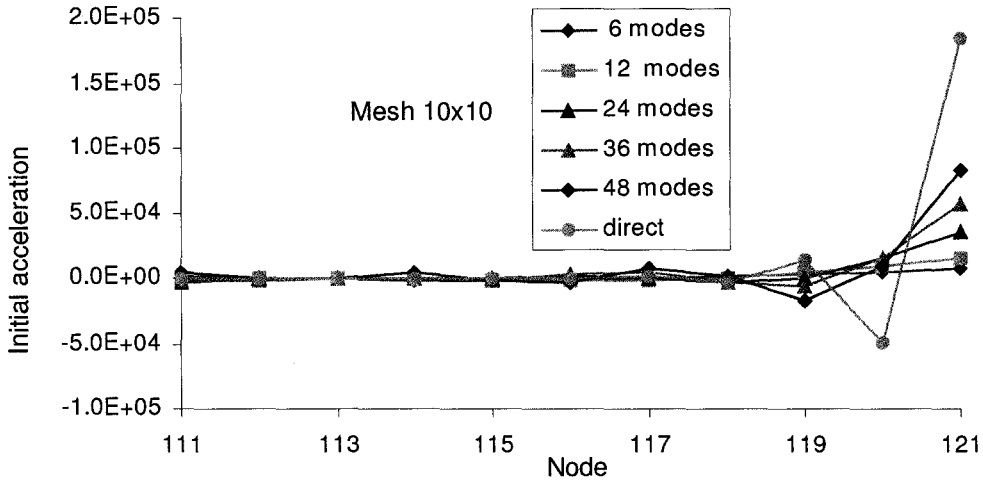

Figure 27 Initial accelerations of the free side under a static force with refined mesh

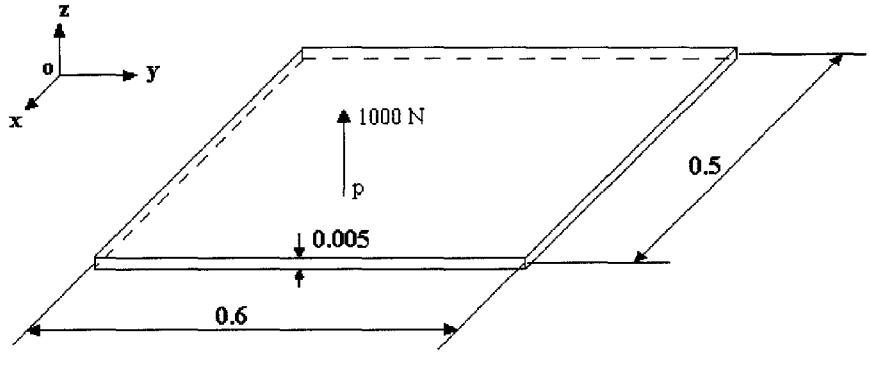

Figure 28 Geometry of a plate under a concentrated force of 1000 Newtons at the center of the plate (length unit in meter)

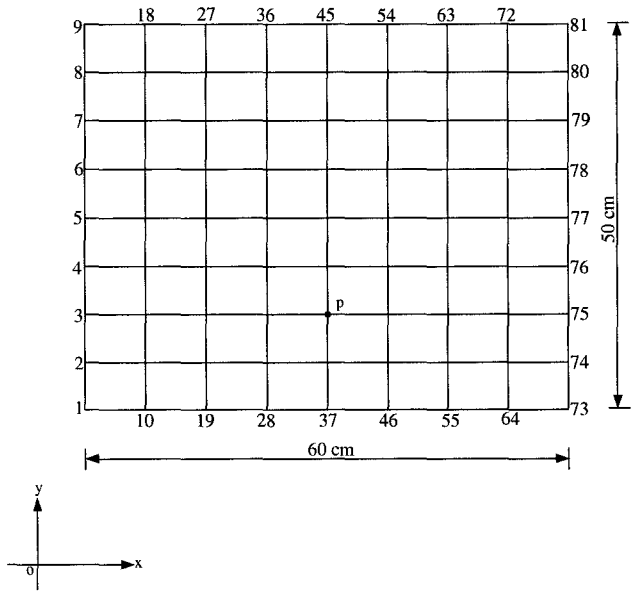

Figure 29 Plate discretized by 64 elements

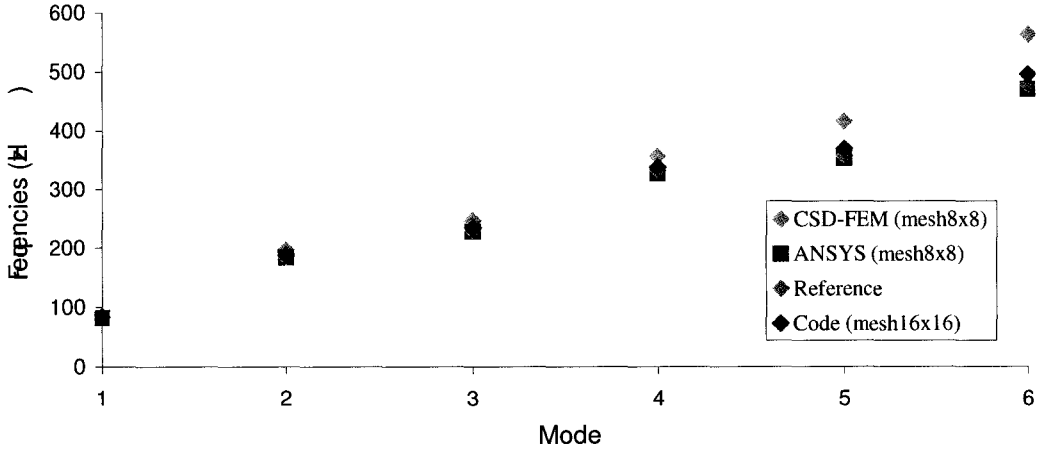

Figure 30 Comparable natural frequencies extracted from CSD-FEM solver

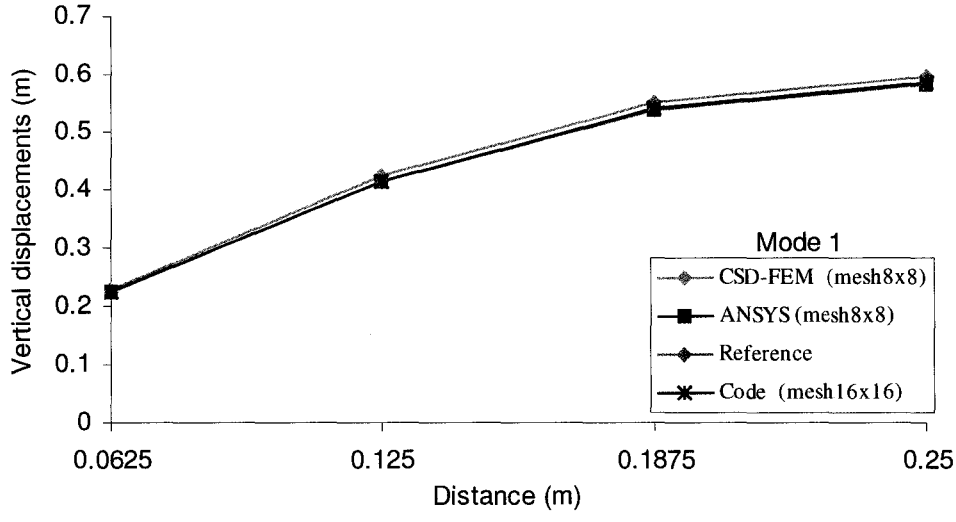

Figure 31 Vertical nodal displacements of the first mode extracted from CSD-FEM solver with comparisons

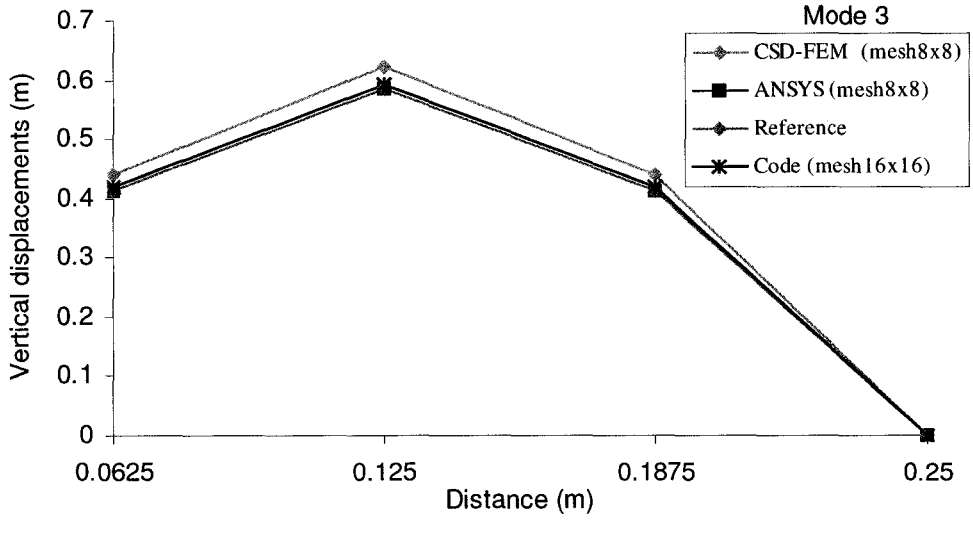

Figure 32 Vertical nodal displacements of the third mode extracted from CSD-FEM solver with comparisons

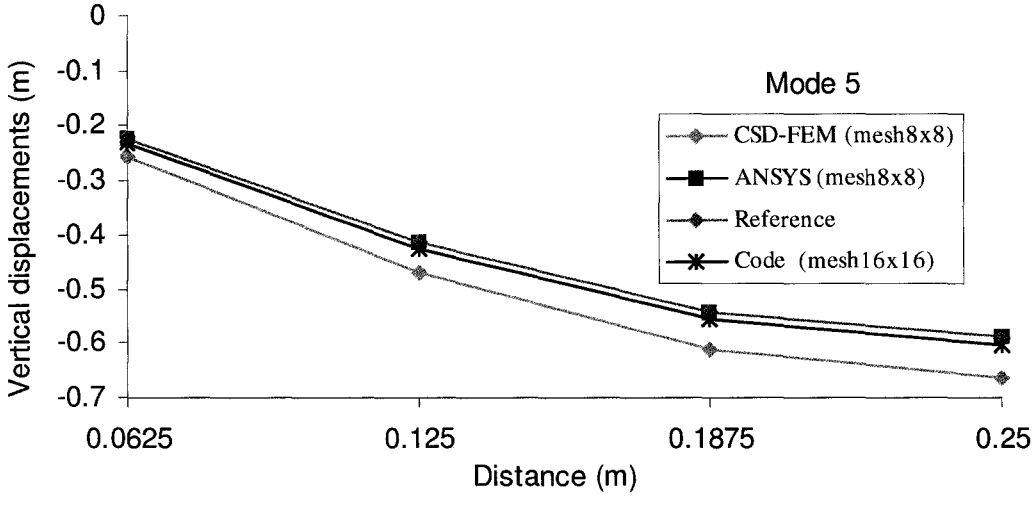

Figure 33 Vertical nodal displacements of the fifth mode extracted from CSD-FEM solver with comparisons

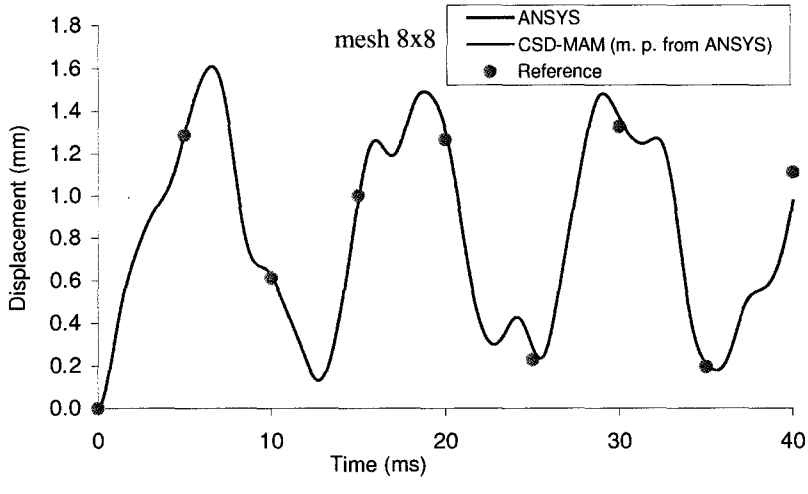

Figure 34 Displacement in thickness direction of a point computed by CSD-MAM using m. p. (modal parameters) extracted from ANSYS software

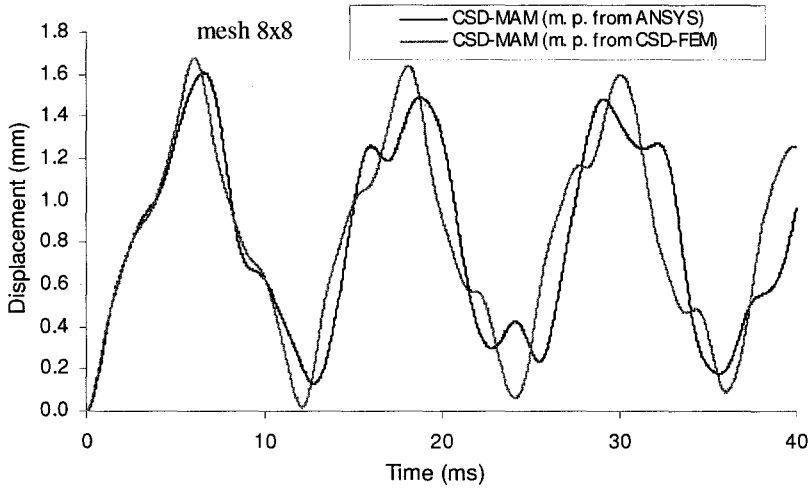

Figure 35 Displacement in thickness direction of a point computed by CSD-MAM using m. p. (modal parameters) extracted from CSD-FEM solver

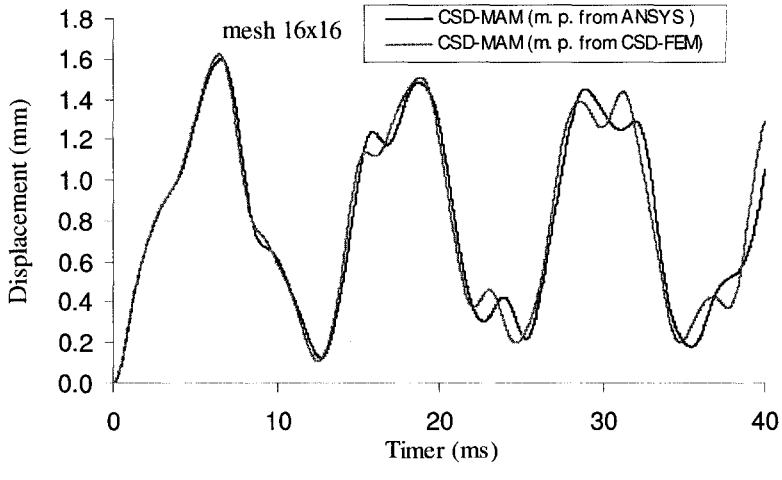

Figure 36 Displacement in thickness direction of a point computed by CSD-MAM using m. p. (modal parameters) extracted from CSD-FEM with refined mesh

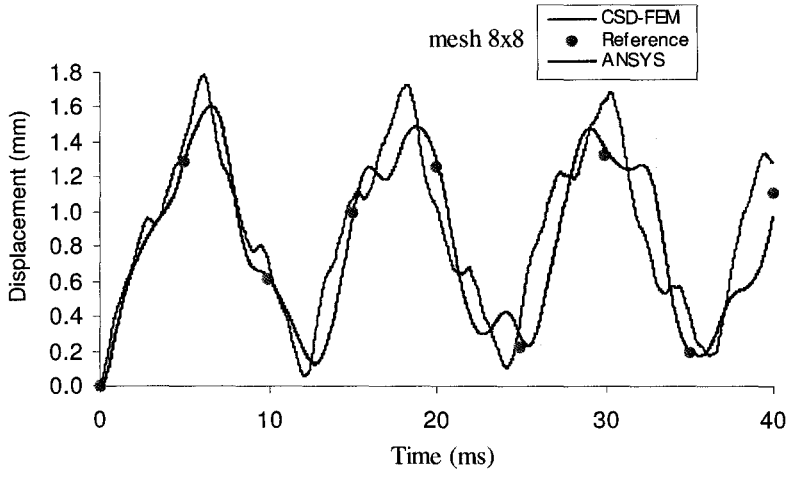

Figure 37 Displacement in the thickness direction of a point computed by CSD-FEM

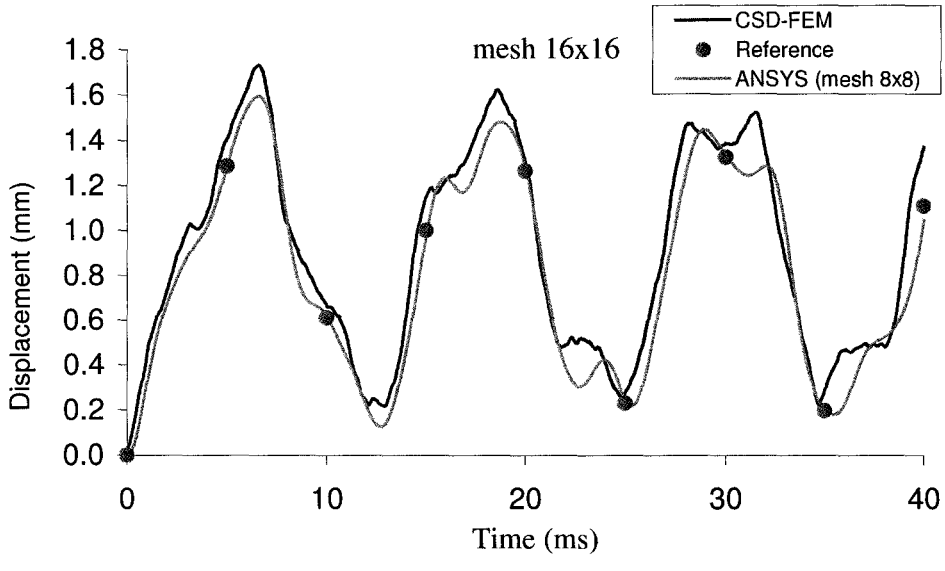

Figure 38 Displacement in the thickness direction of a point computed by CSD-FEM with refined mesh

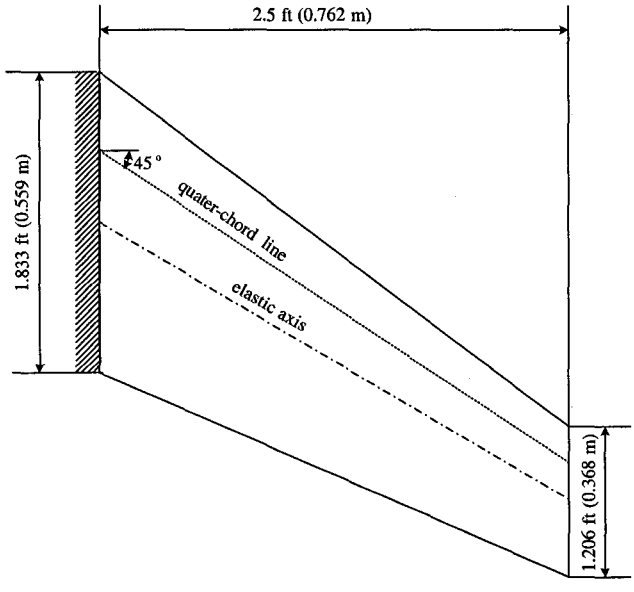

Figure 39 Geometry of Wing AGARD445.6

Figure 40 Profile of airfoil NACA 65A004

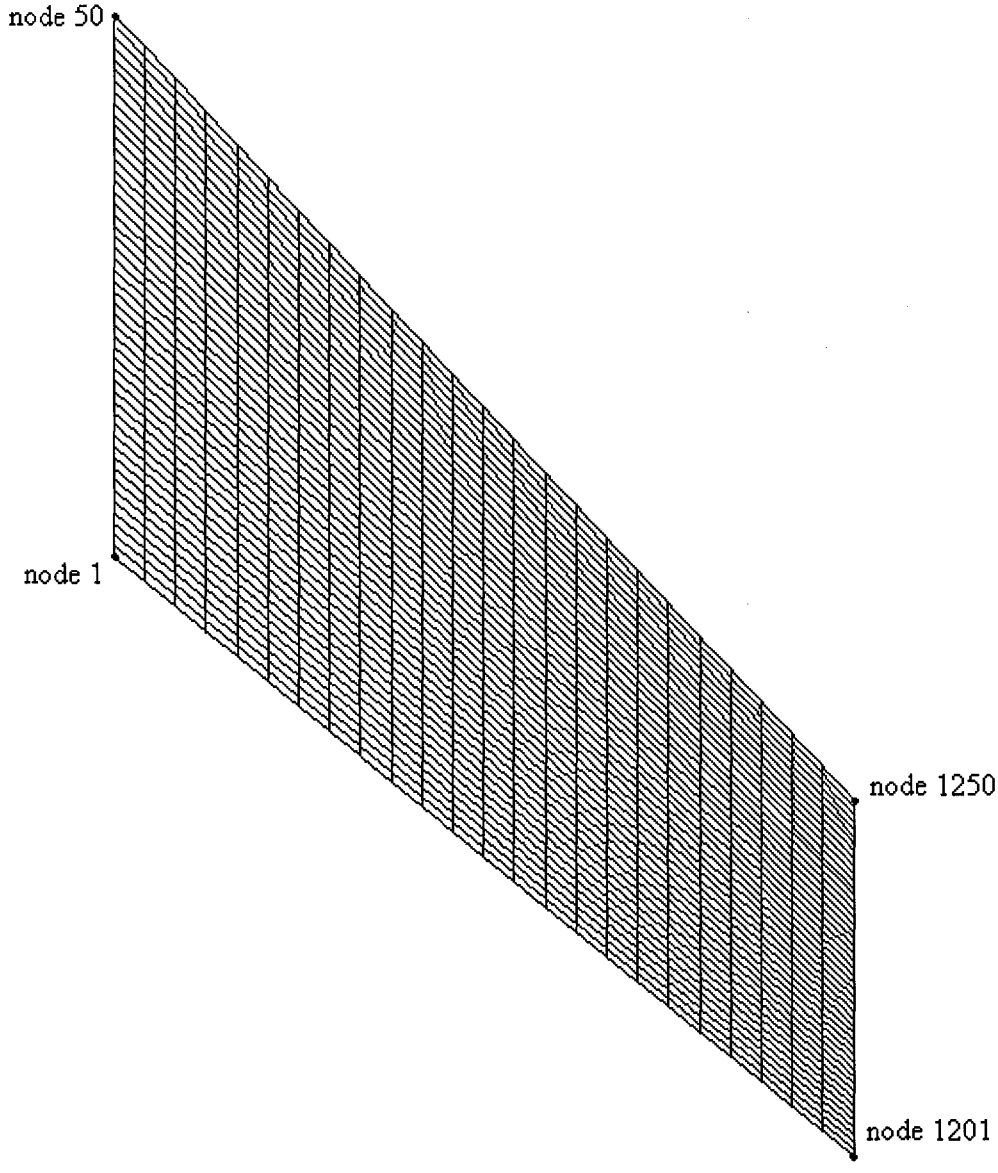

Figure 41 Structural mesh of Wing AGARD445.6 discretized by shell elements

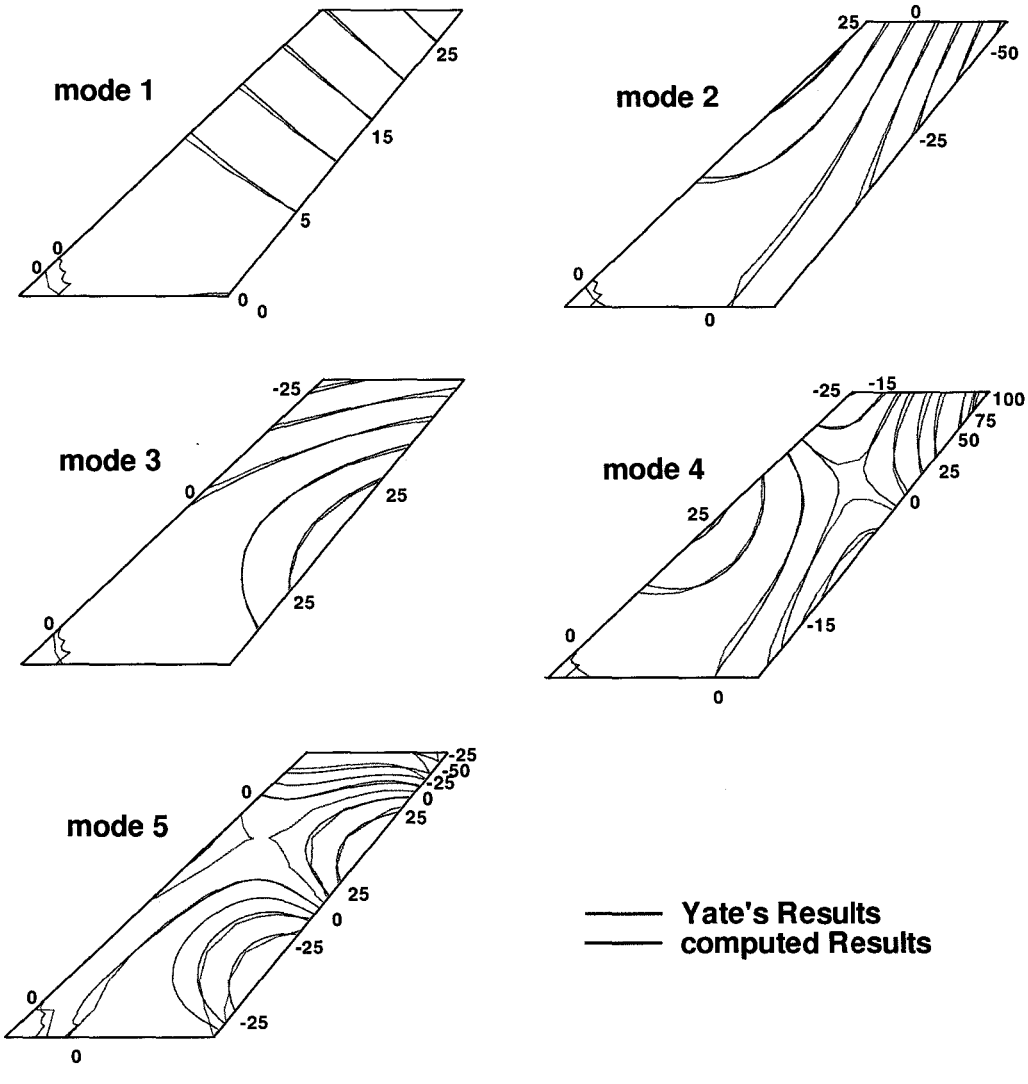

Figure 42 Mode vectors of wing AGARD 445.6 extracted from ANSYS

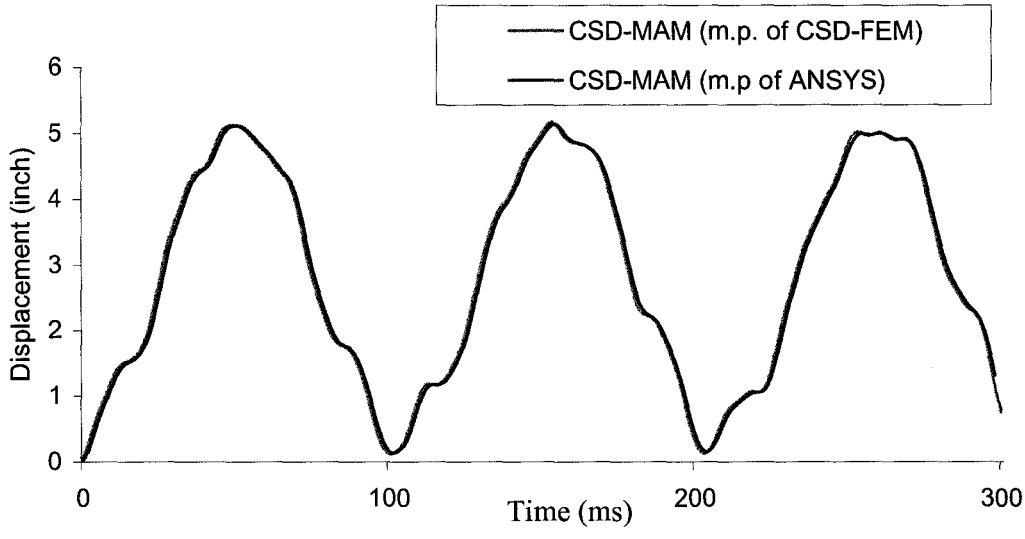

Figure 43 Displacement in thickness directions of the point at the intersection between the leading edge and the tip obtained from CSD-MAM using respectively m. p. (modal parameters) from CSD-FEM and ANSYS

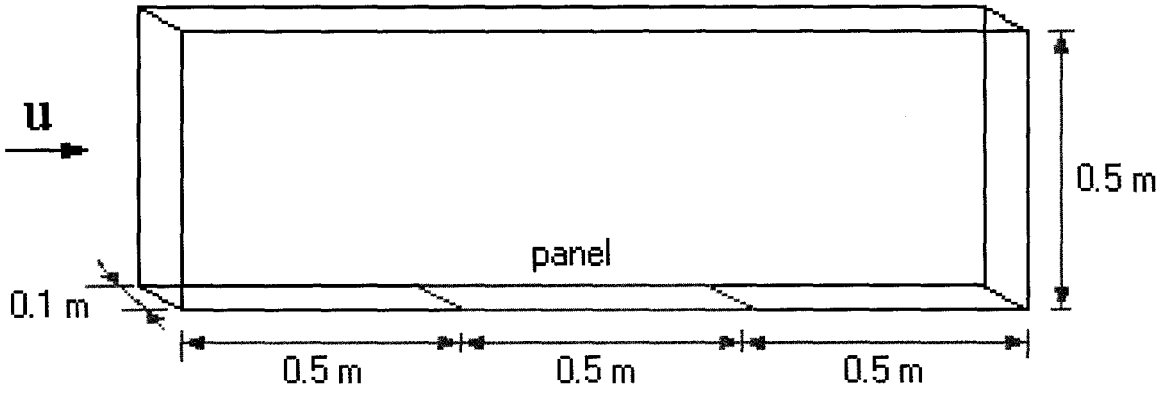

Figure 44 Geometry of fluid domain with a panel

First Mode (bending: 9.6192 Hz)

Second Mode (bending: 26.5096 Hz)

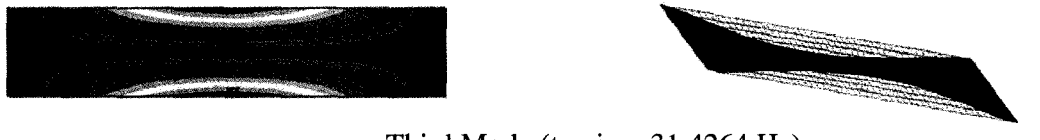

Third Mode (torsion: 31.4264 Hz)

Fourth Mode (bending: 52.1072 Hz)

Fifth Mode (combination of bending and torsion: 65.0327 Hz)

Figure 45 Mode shapes and natural frequencies of the panel

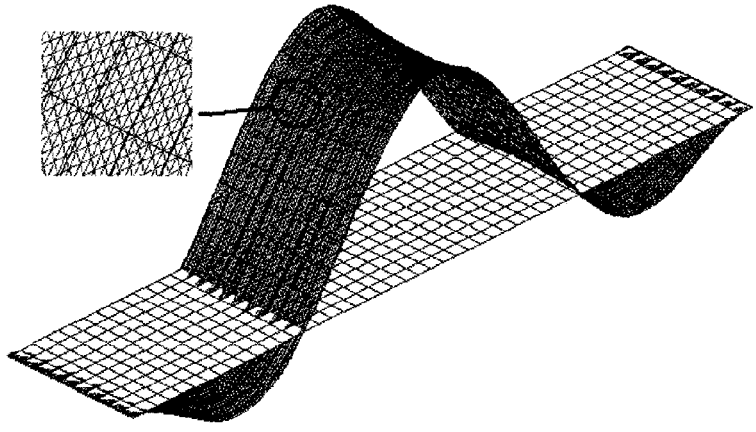

Figure 46 Movement of the fluid-structural interface

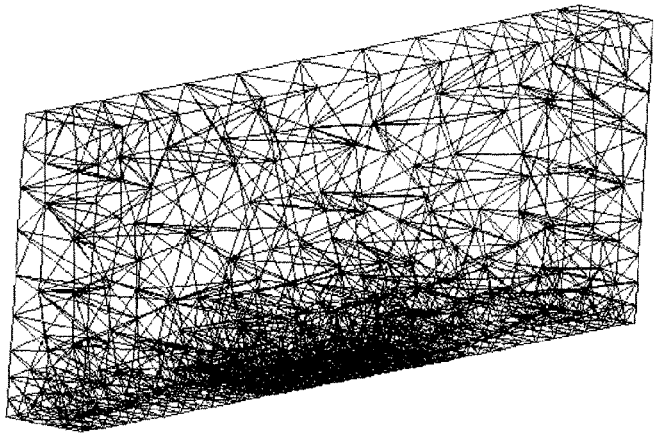

Figure 47 Initial fluid mesh (red zone represents the panel)

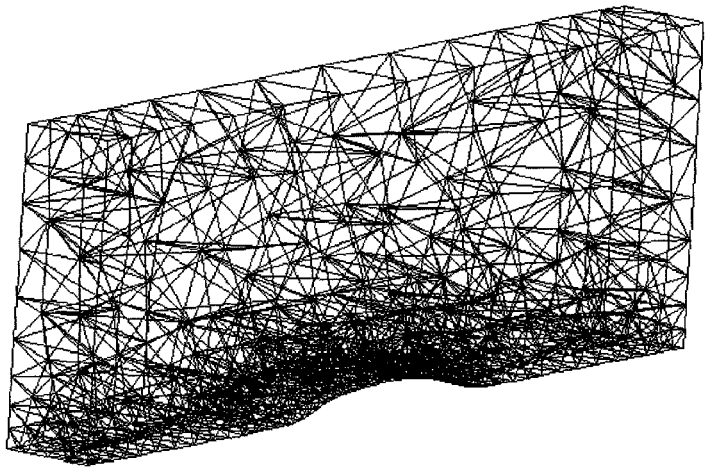

Figure 48 Fluid mesh at 0.15 second

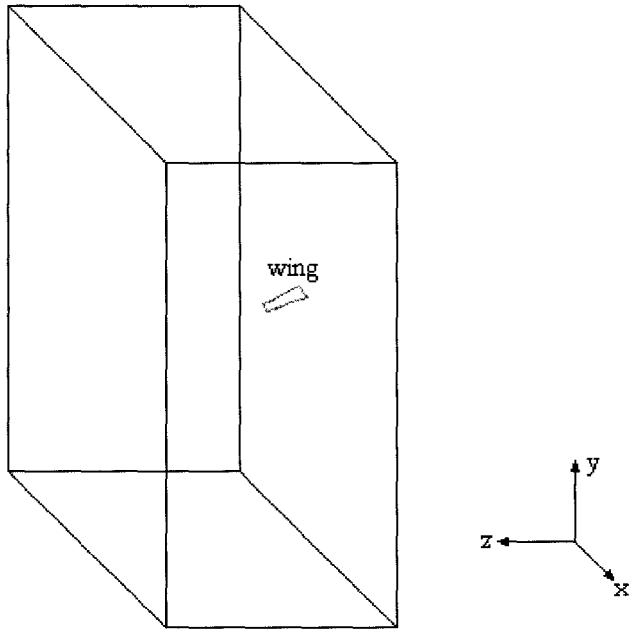

Figure 49 Wing AGARD445.6 in fluid domain

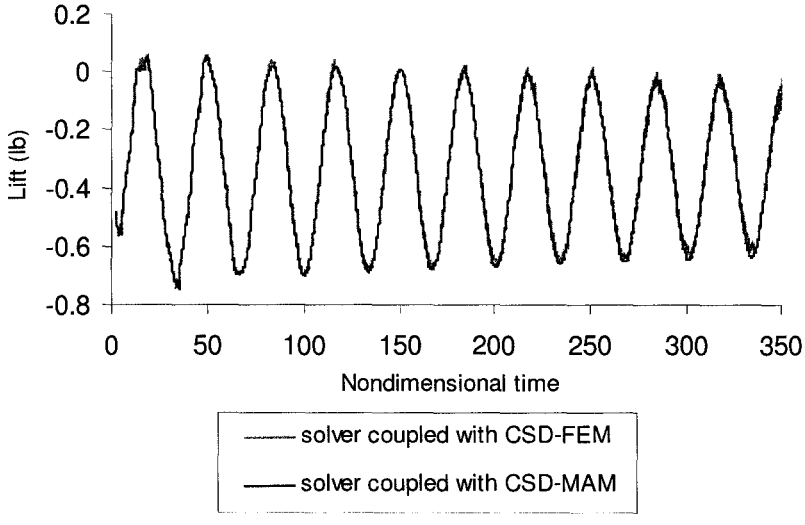

Figure 50 Lift on wing AGARD445.6 under a structural perturbation

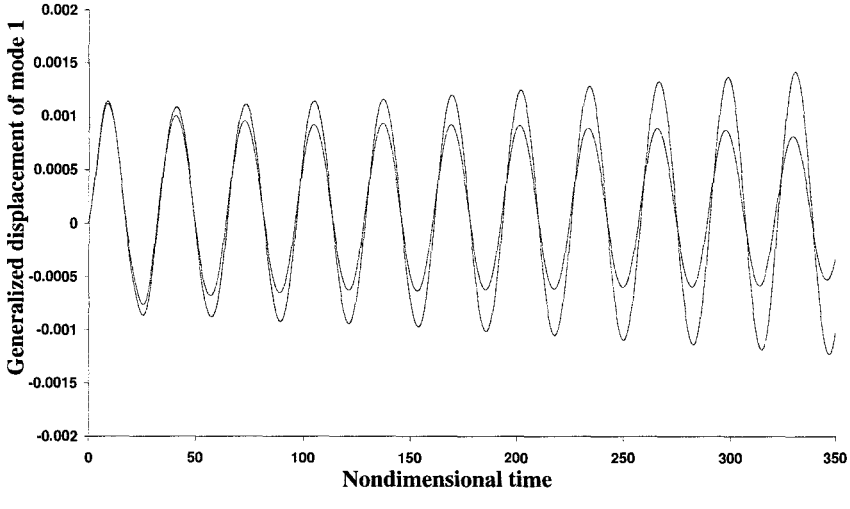

Figure 51 Time history of the generalized displacements of the first mode for the case Mach = 0.96, angle of attack = 0, nondimensional time step = 0.2, reference pressure = 62 lb/sqft with one (blue color) and 3 (green color) coupling iterations

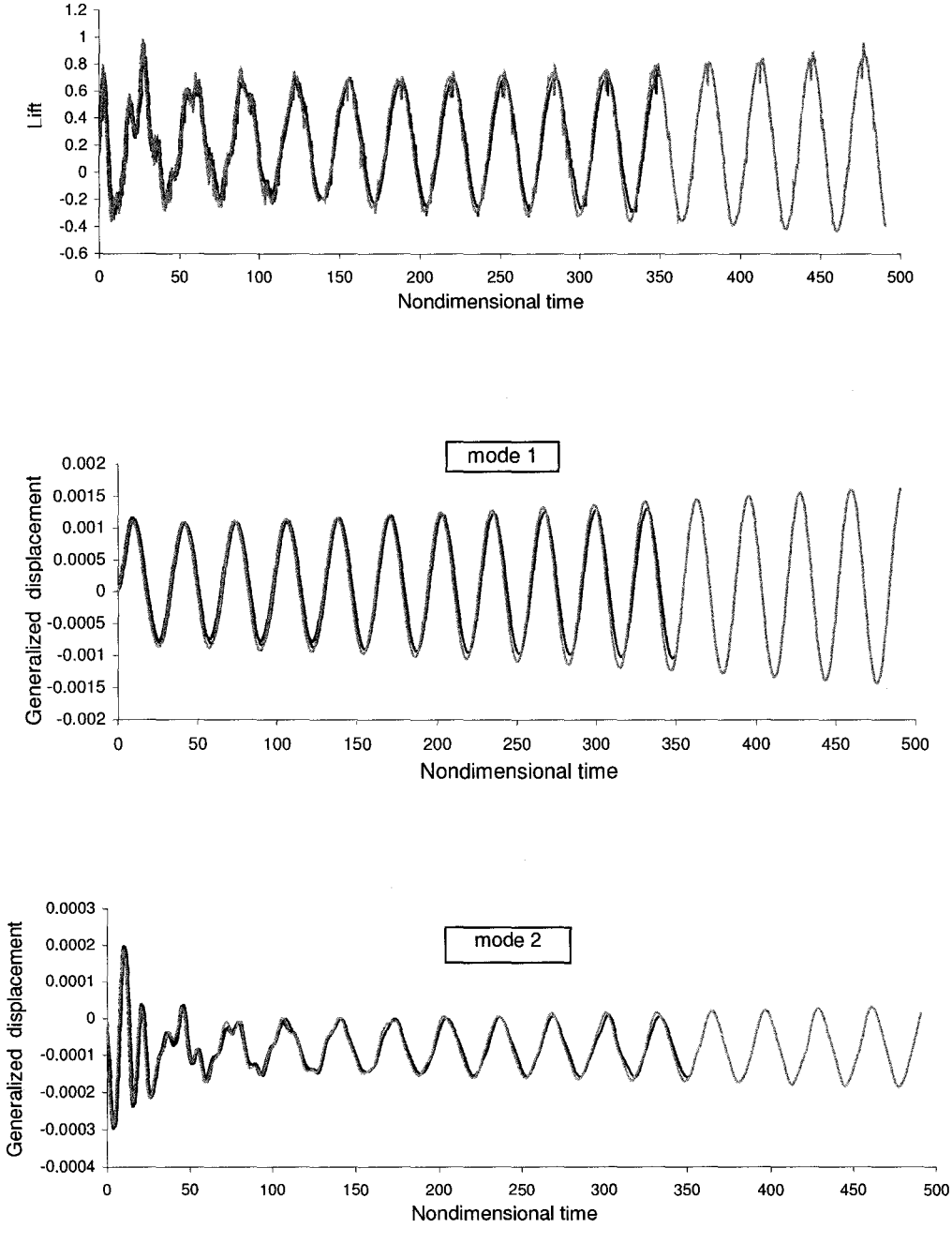

Figure 52 Time history of lift and generalized displacements for the case Mach = 0.96, angle of attack = 0, nondimensional time step = 0.1 (blue color), 0.2 (red color) and 0.3 (lemon color), reference pressure = 62 lb/sqft with one coupling iteration

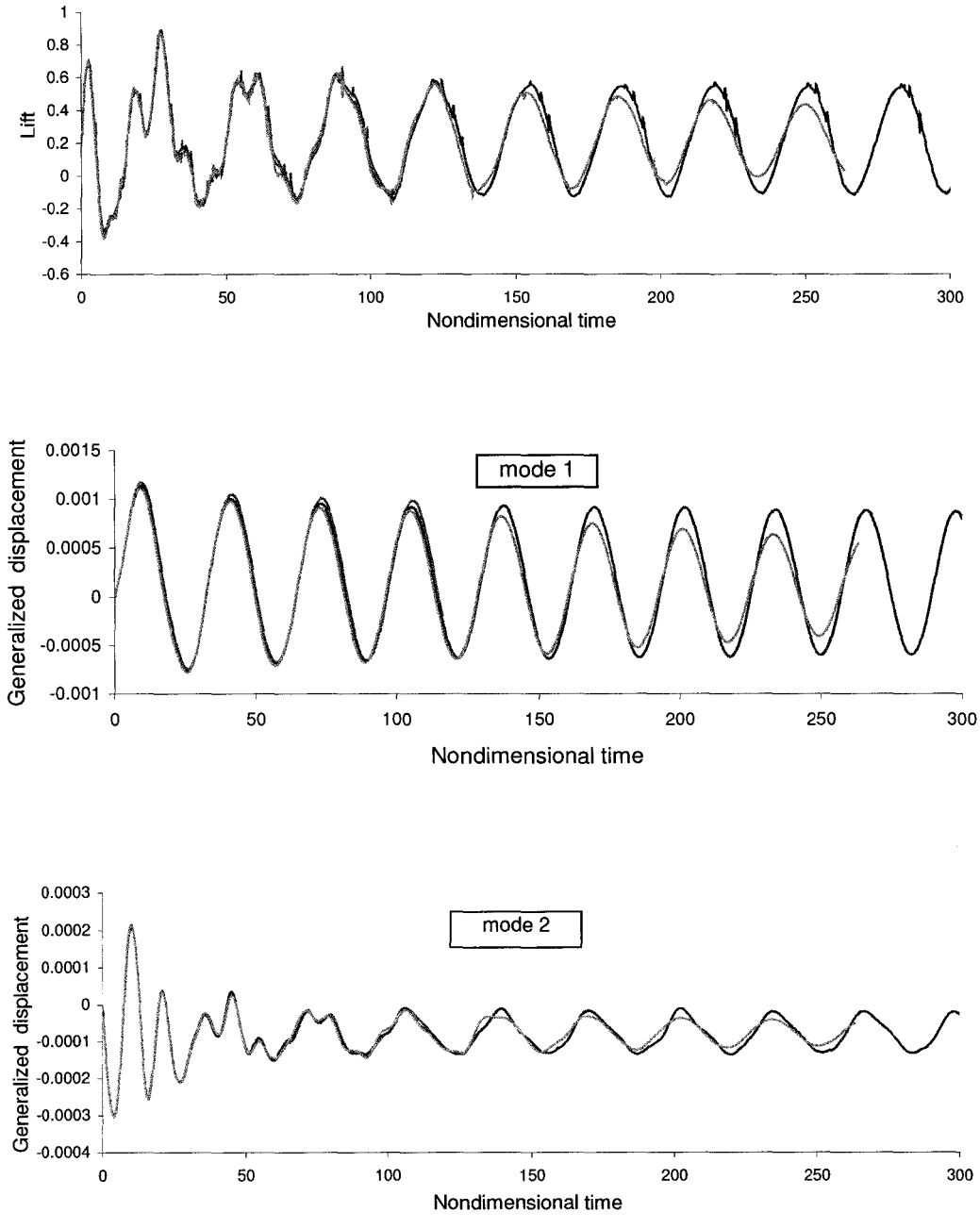

Figure 53 Time history of lift and generalized displacements of the first two modes for the case Mach = 0.96, angle of attack = 0, nondimensional time step = 0.1 (green color), 0.2 (red color) and 0.3 (lemon color), reference pressure = 62 lb/sqft with 3 coupling iterations

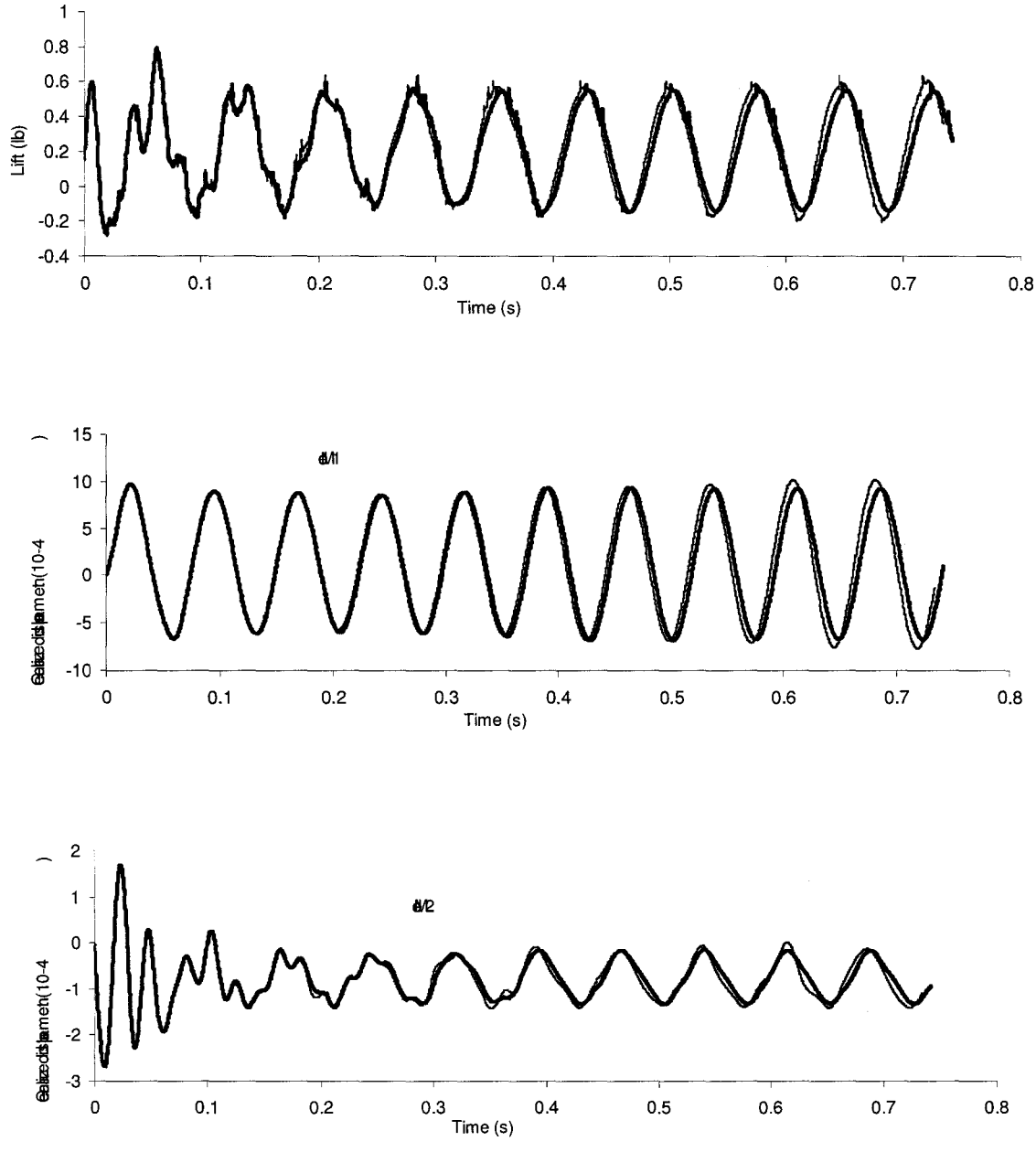

Figure 54 Time history of lifts on the wing AGARD 445.6 and generalized displacements of the first two modes under a load perturbation with nondimensional time step of 0.1 at aerodynamic pressures 60 $lb/sqft$ (blue thick curves) and 61.3 $lb/sqft$ (black thin curves)

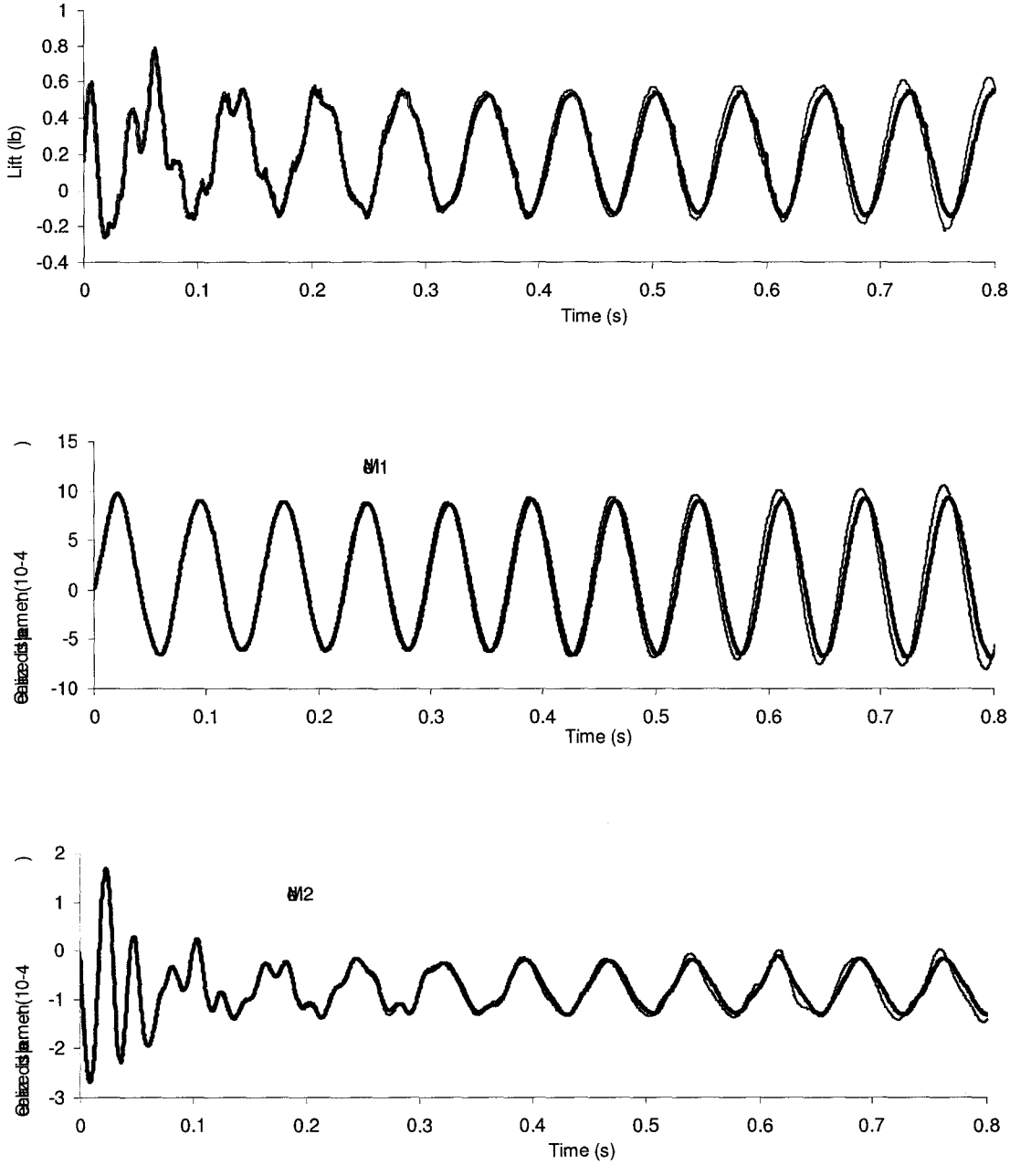

Figure 55 Time history of lifts on the wing AGARD 445.6 and generalized displacements of the first two modes under a load perturbation with nondimensional time step of 0.3 at aerodynamic pressures 60 $lb/sqft$ (blue thick curves) and 61.3 $lb/sqft$ (black thin curves)

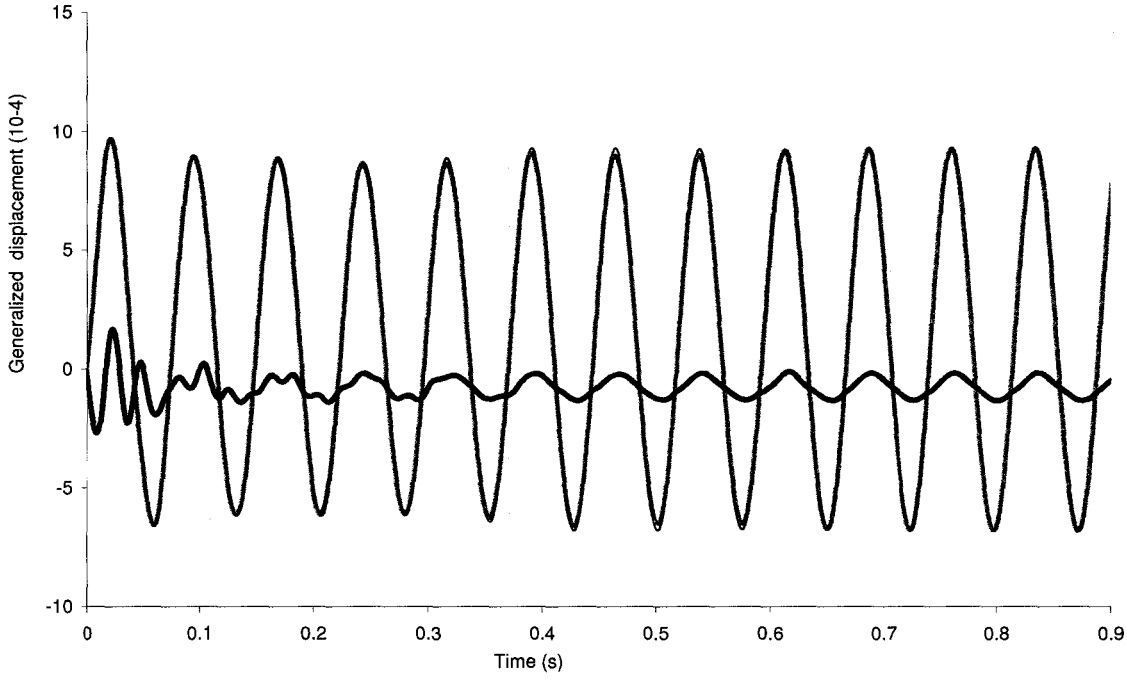

Figure 56 Time history of the generalized displacements of the first two modes of the wing AGARD 445.6 under a load perturbation with nondimensional time step of 0.1 (blue and red curves for mode 1 and mode2) and 0.3 (green and black curves for mode 1 and mode2), aerodynamic pressure of $q = 60\ lb/sqft$

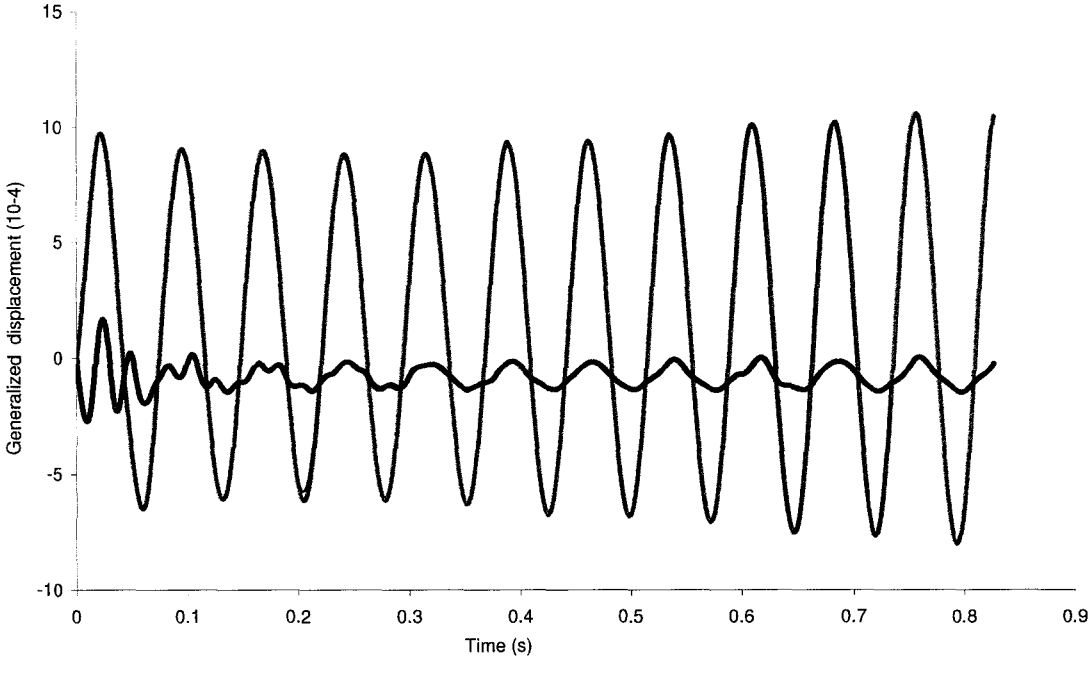

Figure 57 Time history of the generalized displacements of the first two modes of the wing AGARD 445.6 under a load perturbation with nondimensional time step of 0.1 (blue and red curves for mode 1 and mode2) and 0.3 (green and black curves for mode 1 and mode2), aerodynamic pressure of $q = 61.3\ lb/sqft$

CONCLUSIONS

The development of a comprehensive three-dimensional nonlinear computational aeroelasticity code for analysis of nonlinearity behaviors of inviscid compressible flows in transonic regime is the main objective of this thesis. The coupling strategy which is based on the idea of making the software development of multidisciplinary problems easier favors the software development in modularity and the reuse of the developed solvers. It allows us to use the robust validated nonlinear CFD solver of our laboratory in the CFD-based aeroelasticity code. However, the CSD, the mesh solvers and the matcher module are required to be developed due to the limitation of the accessibility of the CSD solvers, the time varying fluid domain and the non-matching grids on the fluid-structure interface.

Since the CFD model is assumed as the only nonlinear model of the aeroelasticity system, the CSD models are based on the linear structural theories. The modal superposition approach is used in the CSD-MAM solver for the benefit of the linear structural properties which can be used to save computing time and memory consumption, especially for flutter simulation of large structures with dynamic structural responses dominated by low natural frequencies. The CSD-FEM solver based directly on the finite element discrete approach has the generality in the applications of the structural dynamic modeling where high frequencies cannot be negligible, such as structural vibrations induced by separated flows. It can be extended to a nonlinear structural model.

For the purpose of adapting the fluid moving boundaries induced by the structural motion, the fluid mesh is updated by the mesh model which is a fictitious model composed of linear elasto material. This update is performed when it is necessary during the computation in order to keep the fluid elements from damage caused by the dilation or compression of its neighbor elements. As a result, the structural motion is diffused smoothly into the fluid domain from the moving fluid boundaries to the far-field boundaries.

The matcher module interprets, in the coupling aeroelasticity solver, the fluid-structure interaction on the interface where non-matching structural and fluid grids presents due to the difference of element sizes and types. For the computational accuracy, the transfers of aerodynamic loads and the structural displacements on this interface satisfy the conservation of energy.

In the CFD solver, the governing Euler equations for transonic flows is discretized on the moving fluid mesh which is updated by the mesh solver when it is necessary during the computation. The CFD solver takes into account the contribution of the velocity of the moving grid in the fluid convection. The nonlinear GMRES algorithm with ILUT preconditioner and the SUPG numerical stabilization technique with a shock capture are implemented in this CFD solver.

The complete nonlinear aeroelasticity solver adopts the Gauss-Seidel coupling algorithm which is piloted by the CFD solver. This implicit algorithm is a staggered one where the computational results are limited by the number of coupling iterations and the time step. The solver coupled respectively with the CSD-MAM and CSD-FEM solvers demonstrates the reuse of the developed solvers of the subsystems.

The numerical experiments for the validation of each solver and module before the complete coupling validation ensure the performance of each component of the code. The structural responses obtained respectively by the the CSD-MAM and CSD-FEM solvers have no significant difference and agree with those of the references. The validation of the mesh solver has proved that the model is able to distribute the structural motion into the fluid domain without element damage. The validation of the matcher module shows that the fluid moving boundaries follow the structural motion. This module is also successfully applied to a vibro-acoustic code [103].

The results of the flutter simulation applied to the AGARD 445.6 aeroelastic wing in transonic flows at Mach number 0.96 with zero angle of attack agree with those in the

references. The critical flutter pressure was obtained at $q = 60\ lb/sqft$ compared to $q = 61.3\ lb/sqft$ reported in the experimental study [33] and the computed frequency was about 13.6 Hz compared to 13.9 Hz [33]. This thesis provides a the methodology for computational aeroelasticity based on CSD and CFD solvers. Such models have also been reused to produce a parallel aeroelasticity solver [6, 100, 104]. Although this code is developed for the nonlinear aeroelasticity systems, other research of multidisciplinary models can benefit from this methodology of the reuse of existing solvers through the coupling strategy.

The main contributions of this project are stated as follows :

- Development of two CSD solvers : CSD-MAM and CSD-FEM which are comparable in applications of linear structures;
- Development of a mesh solver to adapt to the fluid mesh due to moving fluid boundaries which is able to diffuse correctly the motion of a moving fluid boundary into the fluid domain;
- Development of a matcher module for information transfer on the fluid-structure interface, where the aerodynamic loads project from the fluid grid to the structural grid and the moving fluid boundaries follows exactly the structural motion;
- Adaptation of the CFD solver to enable moving meshes. The ALE kinematic formulation is implemented in this modified CFD solver;
- Perform CFD-CSD-mesh coupling through the "matcher" module;
- Creation of a sequential coupling algorithm between the CSD, the CFD and the mesh solvers;
- Investigation of the reutilization of codes by applying respectively the CSD-MAM and the CSD-FEM solvers in the coupling. The CSD-FEM sovler can be extended to nonlinear structure;

- Investigation of the impact of the coupling iterations and the time step to the system's responses in the coupling algorithm.
- Validation of the software on the well-documented aeroelastic test case with the aeroelastic wing AGARD 445.6 and capture the flutter point at the transonic dip.

The refinement of the fluid mesh, the extensions of this code to other algorithms for the coupling between nonlinear CSD solvers and nonlinear CFD solvers described by Navier-Stokes equations for viscous flow with flow separation remain the principal improvements to this code in the future.

APPENDIX

SHELL ELEMENT Q4γ24

The shell element $Q4\gamma24$ has four nodes on the middle surface. Any point q of the element can be described by its corresponding point p on the middle surface whose coordinates can be interpolated by the coordinates of the four nodal coordinates of a bilinear element. The model is based on the shell displacement which is based on the covariant base $\mathbf{F}_z$. The position vector of any point on the middle surface of the element in the local coordinate system is represented by the following equations :

$$\mathbf{x}_p = \sum_{i=1}^{4} N_i(\xi,\eta)\mathbf{x}_i \tag{1}$$

with

$$\mathbf{x}_i = < \; x_i \quad y_i \quad z_i \; >^T$$

where x_i, y_i, z_i denote Cartesian coordinates of node i ($i = 1,2,3,4$), $N_i(\xi,\eta)$ are shape functions of the following bilinear referential element :

$$\mathbf{N} = < \; \frac{(1-\xi)(1-\eta)}{4} \quad \frac{(1+\xi)(1-\eta)}{4} \quad \frac{(1+\xi)(1+\eta)}{4} \quad \frac{(1-\xi)(1+\eta)}{4} \; >$$

where ξ, η are the referential coordinates ($-1 \leq \xi \leq 1$, $-1 \leq \eta \leq 1$).

The derivatives of these shape functions are given by the following equations :

$$\mathbf{N}_{,\xi} = \frac{1}{4} < \; -(1-\eta) \quad (1-\eta) \quad (1+\eta) \quad -(1+\eta) \; >$$

$$\mathbf{N}_{,\eta} = \frac{1}{4} < \; -(1-\xi) \quad -(1+\xi) \quad (1+\xi) \quad (1-\xi) \; >$$

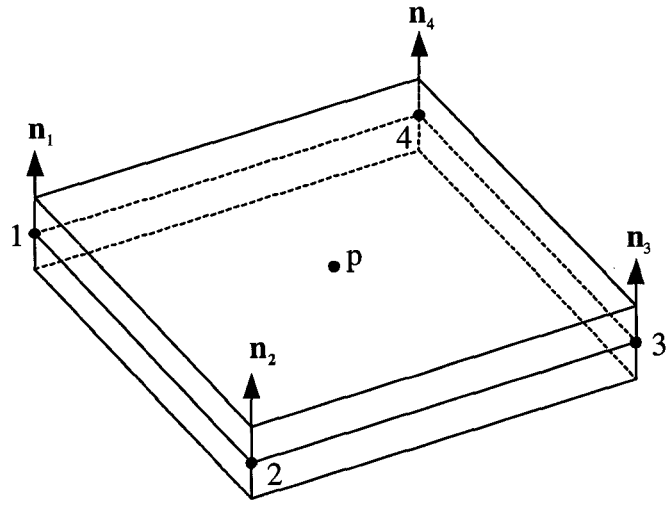

Figure 58 Linear shell element $Q4\gamma24$

These derivatives are used to interpolate the following orthogonal basic vector described by equations (2.3) and (2.4) :

$$\mathbf{a}_1 = \sum_{i=1}^{4} N_{i,\xi}(\xi,\eta)\mathbf{x}_i$$

$$\mathbf{a}_2 = \sum_{i=1}^{4} N_{i,\eta}(\xi,\eta)\mathbf{x}_i$$

The unit normal vector of point p on its tangent plane becomes :

$$\mathbf{n} = \frac{\mathbf{a}_1 \times \mathbf{a}_2}{|\mathbf{a}_1 \times \mathbf{a}_2|}$$

The position vector of any point $q(z \neq 0)$ of the shell element is defined as :

$$\mathbf{x}_q = \mathbf{x}_p + z\mathbf{n}$$

with $z = \zeta h/2$, where h is constant. The covariant base is :

$$[\mathbf{F}_z] = [\mathbf{a}_{1z} \vdots \mathbf{a}_{2z} \vdots \mathbf{n}]$$

$[\mathbf{F}_z]$ is linear in thickness direction (z direction). It is composed of the covariant base of the middle surface and the base of the derivative of its normal vector :

$$[\mathbf{F}_z] = [\mathbf{F}_0] + z[\mathbf{F}_n]$$

with

$$[\mathbf{F}_0] = [\mathbf{a}_1 \vdots \mathbf{a}_2 \vdots \mathbf{n}]$$

$$[\mathbf{F}_n] = [\mathbf{n}_{,\xi} \vdots \mathbf{n}_{,\eta} \vdots 0]$$

The determinant of the Jacobian matrix **J** is :

$$\det(J) = \det(\mathbf{F}_z) = \mu(z) \det(J_0)$$

where $\mu(z) = 1$ since the four nodes of $Q4\gamma24$ element are assumed coplanar.

The local coordinate system for any point on the middle surface of the element is transformed from the global coordinate system by an orthogonal base :

$$[\mathbf{Q}] = [\mathbf{t}_1 \vdots \mathbf{t}_2 \vdots \mathbf{n}]$$

where $\mathbf{t}_1 = \mathbf{a}_1/|\mathbf{a}_1|$, $\mathbf{t}_2 = \mathbf{n}_1 \times \mathbf{t}_1$. The normal vector of the middle surface is interpolated by the four nodal normal vectors.

$$\mathbf{n}_{,\xi} = \sum_{i=1}^{4} N_{i,\xi} \mathbf{n}_i$$

$$\mathbf{n}_{,\eta} = \sum_{i=1}^{4} N_{i,\eta}\mathbf{n}_i$$

where $\mathbf{n}_i$ is the unit normal vector at node i.

The local coordinate system for any node of the element is transformed from the global coordinate system by the following orthogonal base :

$$[\mathbf{Q}_i] = [\mathbf{t}_{1i} \vdots \mathbf{t}_{2i} \vdots \mathbf{n}]$$

where $\mathbf{Q}_i$ is obtained in the similar way as $\mathbf{Q}$.

The shell element $Q4\gamma24$ for the displacement model has five degrees of freedom in the local coordinate system (three translations and two rotations). The displacement of point q is the sum of the displacement of point p and the vector **pq** after its rotation. The virtual displacement described by equation (2.6) gives :

$$\mathbf{x}_q^* = \mathbf{x}_p^* + z\boldsymbol{\beta}^* = \sum_{i=1}^{4} N_i \mathbf{u}_{pi}^* + z\sum_{i=1}^{4} N_i(-\mathbf{t}_{2i}\theta_{1i}^* - \mathbf{t}_{1i}\theta_{2i}^*)$$

where θ_{1i}^* is the rotation in the plane $\mathbf{t}_{2i}$, $\mathbf{n}$, θ_{2i}^* is the rotation in the plane $\mathbf{t}_{1i}$, $\mathbf{n}$. In the global coordinate system, the virtual displacement is defined as :

$$\begin{Bmatrix} U_q^* \\ V_q^* \\ W_q^* \end{Bmatrix} = \begin{Bmatrix} U^* \\ V^* \\ W^* \end{Bmatrix} + z\left(-\theta_1^* \begin{Bmatrix} t_{2x} \\ t_{2y} \\ t_{2z} \end{Bmatrix} + \theta_2^* \begin{Bmatrix} t_{1x} \\ t_{1y} \\ t_{1z} \end{Bmatrix} \right)$$

where U_q^*, V_q^*, W_q^* are the displacements of point q in the global coordinate system. The virtual and the real displacement vectors of point q can be interpolated by the shape functions of this shell element :

$$\{\mathbf{u}_q^*\} = [\bar{\mathbf{N}}(\xi, \eta, z)]\{\mathbf{u}_n^*\}$$

$$\{\mathbf{u}_q\} = [\bar{\mathbf{N}}(\xi, \eta, z)]\{\mathbf{u}_n\}$$

where $\bar{\mathbf{N}}$ is a matrix with dimension (3×20) composed of the shape functions of the shell element which is based on the shape functions of its corresponding bilinear element :

$$[\bar{\mathbf{N}}] = \begin{bmatrix} \ldots & \vdots N_i & 0 & 0 & \vdots \frac{1}{2}\zeta N_i < \mathbf{V}_X > \vdots & \ldots & \\ \ldots & \vdots 0 & N_i & 0 & \vdots \frac{1}{2}\zeta N_i < \mathbf{V}_Y > \vdots & \ldots & i = 1, \ldots, 4 \\ \ldots & \vdots 0 & 0 & N_i & \vdots \frac{1}{2}\zeta N_i < \mathbf{V}_Z > \vdots & \ldots & \end{bmatrix}$$

where N_i is the bilinear shape functions and $\mathbf{V}_X, \mathbf{V}_Y, \mathbf{V}_Z$ are expressed as :

$$\begin{aligned} \mathbf{V}_X &= < \; -t_{2xi} \quad t_{1xi} \; > \\ \mathbf{V}_Y &= < \; -t_{2yi} \quad t_{1yi} \; > \\ \mathbf{V}_Z &= < \; -t_{2zi} \quad t_{1zi} \; > \end{aligned}$$

$\mathbf{u}_n^*$ and $\mathbf{u}_n$ are respectively the virtual and real nodal displacements which can be expressed as :

$$\begin{aligned} \{\mathbf{u}_n\} = < & U_1 \quad V_1 \quad W_1 \quad \theta_{11} \quad \theta_{21} \quad U_2 \quad V_2 \quad W_2 \quad \theta_{12} \quad \theta_{22} \\ & U_3 \quad V_3 \quad W_3 \quad \theta_{13} \quad \theta_{23} \quad U_4 \quad V_4 \quad W_4 \quad \theta_{14} \quad \theta_{24} >^T \end{aligned}$$

$$\begin{aligned} \{\mathbf{u}_n^*\} = < & U_1^* \quad V_1^* \quad W_1^* \quad \theta_{11}^* \quad \theta_{21}^* \quad U_2^* \quad V_2^* \quad W_2^* \quad \theta_{12}^* \quad \theta_{22}^* \\ & U_3^* \quad V_3^* \quad W_3^* \quad \theta_{13}^* \quad \theta_{23}^* \quad U_4^* \quad V_4^* \quad W_4^* \quad \theta_{14}^* \quad \theta_{24}^* >^T \end{aligned}$$

The virtual displacement is associated with the following virtual deformation due to the effect of the membrane bending :

$$[\boldsymbol{\varepsilon}_s^*] = \frac{1}{2}([\mathbf{L}_s^*] + [\mathbf{L}_s^*]^T) = \begin{bmatrix} \varepsilon_x^* & \gamma_{xy}^*/2 \\ sym. & \varepsilon_y^* \end{bmatrix}$$

The elementary virtual displacement gradient is given as :

$$[\mathbf{L}_s^*] = \begin{bmatrix} < t_1 > \\ < t_2 > \end{bmatrix} ([\mathbf{u}_{p,\xi}^* \vdots \mathbf{u}_{p,\eta}^*] + z[\boldsymbol{\beta}_{,\xi}^* \vdots \boldsymbol{\beta}_{,\eta}^*])[\mathbf{C}_0][\boldsymbol{\mu}]$$

where $[\boldsymbol{\mu}] = [\mathbf{I}]$ for a $Q4\gamma24$ element with four coplanar nodes. $\mathbf{L}_s^*$ can be developed as :

$$[\mathbf{L}_s^*] = \begin{bmatrix} L_{t11}^* & L_{t12}^* \\ L_{t21}^* & L_{t22}^* \end{bmatrix} = [\mathbf{L}_{s0}^*] + z[\mathbf{L}_{s\beta}^*] \tag{2}$$

where $\mathbf{L}_{s0}^*$ is the deformation of the middle surface, $\mathbf{L}_{s\beta}^*$ is the deformation due to the rotation around the normal of point p on the middle surface. $\mathbf{L}_{s0}^*$ and $\mathbf{L}_{s\beta}^*$ are given as :

$$[\mathbf{L}_{s0}^*] = \begin{bmatrix} \mathbf{t}_1 \cdot \mathbf{u}_{p,\xi}^* & \mathbf{t}_1 \cdot \mathbf{u}_{p,\eta}^* \\ \mathbf{t}_2 \cdot \mathbf{u}_{p,\xi}^* & \mathbf{t}_2 \cdot \mathbf{u}_{p,\eta}^* \end{bmatrix} [\mathbf{C}_0]$$

$$[\mathbf{L}_{s\beta}^*] = \begin{bmatrix} \mathbf{t}_1 \cdot \boldsymbol{\beta}_{,\xi}^* & \mathbf{t}_1 \cdot \boldsymbol{\beta}_{,\eta}^* \\ \mathbf{t}_2 \cdot \boldsymbol{\beta}_{,\xi}^* & \mathbf{t}_2 \cdot \boldsymbol{\beta}_{,\eta}^* \end{bmatrix} [\mathbf{C}_0]$$

with

$$[\mathbf{C}_0^*] = \begin{bmatrix} \mathbf{C}_{11}^0 & \mathbf{C}_{12}^0 \\ \mathbf{C}_{21}^0 & \mathbf{C}_{22}^0 \end{bmatrix} = \begin{bmatrix} \mathbf{a}^1 \cdot \mathbf{t}_1 & \mathbf{a}^1 \cdot \mathbf{t}_1 \\ \mathbf{a}^2 \cdot \mathbf{t}_2 & \mathbf{a}^2 \cdot \mathbf{t}_2 \end{bmatrix}$$

Therefore, the virtual deformation due to the effect of the membrane bending becomes :

$$< \boldsymbol{\varepsilon}_s^* > = < \ \varepsilon_x^* \ \ \varepsilon_y^* \ \ \gamma_{xy}^* \ > = < \boldsymbol{\varepsilon}_0^* > + z < \boldsymbol{\varepsilon}_1^* > \tag{3}$$

with

$$< \varepsilon_j^* >=< \quad L_{j11}^* \quad L_{j22}^* \quad L_{j12}^* + L_{j21}^* \quad > \qquad (j = 0, 1)$$

Using the shape functions, the virtual deformation ε_s^* can be represented by the nodal displacement vector $\mathbf{u}_n^*$:

$$< \varepsilon_s^* >= ([\mathbf{B}_0] + z[\mathbf{B}_1]) < \mathbf{u}_n^* > \tag{4}$$

with

$$[\mathbf{B}_0] = \begin{bmatrix} < \mathbf{t}_1 > C1_i & \vdots 0 \;\; 0 \vdots & \ldots & \\ < \mathbf{t}_2 > C2_i & \vdots 0 \;\; 0 \vdots & \ldots & i = 1, ..., 4 \\ < \mathbf{t}_1 > C2_i + < \mathbf{t}_2 > C1_i & \vdots 0 \;\; 0 \vdots & \ldots & \end{bmatrix}$$

$$C1_i = N_{i,\xi} C_{11}^0 + N_{i,\eta} C_{21}^0$$
$$C2_i = N_{i,\xi} C_{12}^0 + N_{i,\eta} C_{22}^0$$

$$[\mathbf{B}_1] = \begin{bmatrix} 0 \;\; 0 \;\; 0 & \vdots < \mathbf{V1}_i > C1_i \vdots & \ldots & \\ 0 \;\; 0 \;\; 0 & \vdots < \mathbf{V2}_i > C2_i \vdots & \ldots & i = 1, 4 \\ 0 \;\; 0 \;\; 0 & \vdots < \mathbf{V1}_i > C2_i + < \mathbf{V2}_i > C1_i \vdots & \ldots & \end{bmatrix}$$

For the Galerkin formulation, the real deformation can be written as :

$$\{\varepsilon_s\} = ([\mathbf{B}_0] + z[\mathbf{B}_1])\{\mathbf{u}_n\} \tag{5}$$

In equation (3.9), the internal work due to the deformation of the effect of the membrane bending can be written as :

$$W_{mf}^e = \int_{V^e} < \varepsilon_s^* > [\mathbf{H}]\{\varepsilon_s\} dV \tag{6}$$

The real shear strain can be obtained in the same way described above. Similar to equations (5), the real shear strain at any point q of the shell element is given as :

$$\{\gamma_s\} = \{\gamma_0\} + z\{\gamma_1\}$$

with

$$\{\gamma_0\} = \{\gamma_{s0}\} = [\mathbf{C}_0]^T\{\gamma_\alpha\}$$

and

$$\{\gamma_1\} = [\mathbf{bc}]^T\{\gamma_\alpha\}$$

where $\{\gamma_1\} =< \gamma_{xz} \quad \gamma_{yz} >^T$, $\{\gamma_0\} =< \gamma_x \quad \gamma_y >^T$, $\{\gamma_\alpha\} =< \gamma_\xi \quad \gamma_\eta >^T$
The covariant components γ_ξ and γ_η for any element are given by the following functions which are defined at the middle point of each side of the bilinear element :

$$\gamma_\xi = \frac{1-\eta}{2}\gamma_\xi^{A_1} + \frac{1+\eta}{2}\gamma_\xi^{A_2}$$
$$\gamma_\eta = \frac{1-\xi}{2}\gamma_\eta^{B_1} + \frac{1+\xi}{2}\gamma_\eta^{B_2}$$

where A_1, A_2, B_1, B_2 are the middle points of the four sides of a bilinear element which represent the middle surface of the shell element (Figure 59). $\gamma_\xi^{A_1}$, $\gamma_\xi^{A_2}$, $\gamma_\eta^{B_1}$, $\gamma_\eta^{B_2}$ can be expressed by the nodal displacements $\mathbf{u}_n$. Using the following function :

$$\{\gamma_\alpha\} = \left\{ \begin{array}{l} \boldsymbol{\beta} \cdot \mathbf{a}_1 + \mathbf{u}_{p,\xi} \cdot \mathbf{n} \\ \boldsymbol{\beta} \cdot \mathbf{a}_2 + \mathbf{u}_{p,\eta} \cdot \mathbf{n} \end{array} \right\}$$

One obtains :

$$\gamma_{\xi}^{A_1} = (\boldsymbol{\beta} \cdot \mathbf{a}_1 + \mathbf{u}_{p,\xi} \cdot \mathbf{n})_{\xi=0,\ \eta=-1}$$
$$\gamma_{\xi}^{A_2} = (\boldsymbol{\beta} \cdot \mathbf{a}_1 + \mathbf{u}_{p,\xi} \cdot \mathbf{n})_{\xi=0,\ \eta=1}$$
$$\gamma_{\eta}^{B_1} = (\boldsymbol{\beta} \cdot \mathbf{a}_2 + \mathbf{u}_{p,\eta} \cdot \mathbf{n})_{\xi=-1,\ \eta=0}$$
$$\gamma_{\eta}^{B_2} = (\boldsymbol{\beta} \cdot \mathbf{a}_2 + \mathbf{u}_{p,\eta} \cdot \mathbf{n})_{\xi=1,\ \eta=0}$$

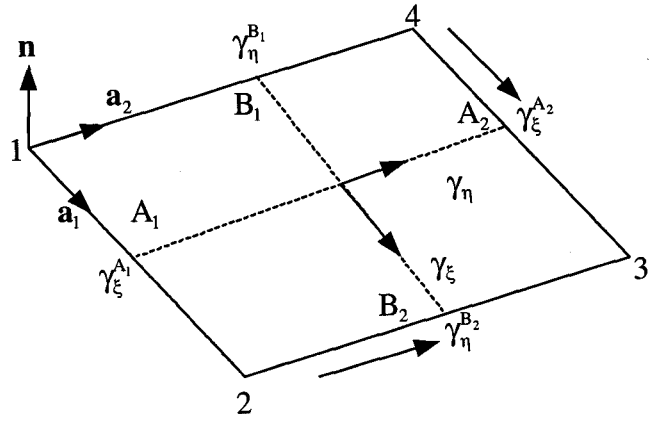

Figure 59 Description of shear strain of a bilinear element

Therefore, the vector $\{\gamma_{\alpha}\}$ can be expressed by the following nodal displacement vectors as :

$$\{\gamma_{\alpha}\} = [\mathbf{B}_{c\xi}]\{\mathbf{u}_n\} \tag{7}$$

$[\mathbf{B}_{c\xi}]$ is a matrix of 2×20 as :

$[\mathbf{B}_{c\xi}] =$

$$\left[\begin{array}{cccc:cccc:cccc:cccc:cccc} -<\mathbf{nA1}> & <\mathbf{AS1}^{A1}> & <\mathbf{nA1}> & <\mathbf{AS2}^{A1}> & <\mathbf{nA2}> & <\mathbf{AS2}^{A2}> & -<\mathbf{nA2}> & <\mathbf{AS1}^{A2}> \\ -<\mathbf{nB1}> & <\mathbf{AS1}^{B1}> & -<\mathbf{nB2}> & <\mathbf{AS1}^{B2}> & <\mathbf{nB2}> & <\mathbf{AS2}^{B2}> & <\mathbf{nB1}> & <\mathbf{AS2}^{B1}> \end{array}\right]$$

with

$$<\mathbf{nA1}>=\frac{1-\eta}{4}\mathbf{n}^{A1}$$

$$<\mathbf{nA2}>=\frac{1+\eta}{4}\mathbf{n}^{A2}$$

$$<\mathbf{nB1}>=\frac{1-\xi}{4}\mathbf{n}^{B1}$$

$$<\mathbf{nB2}>=\frac{1+\xi}{4}\mathbf{n}^{B2}$$

$$<\mathbf{AS1}^{A1}>=\frac{1-\eta}{4}<-\mathbf{a}^{A1}\cdot\mathbf{t}_2^{(1)}:\mathbf{a}^{A1}\cdot\mathbf{t}_1^{(1)}>$$

$$<\mathbf{AS1}^{A2}>=\frac{1+\eta}{4}<-\mathbf{a}^{A2}\cdot\mathbf{t}_2^{(4)}:\mathbf{a}^{A2}\cdot\mathbf{t}_1^{(4)}>$$

$$<\mathbf{AS1}^{B1}>=\frac{1-\xi}{4}<-\mathbf{a}^{B1}\cdot\mathbf{t}_2^{(1)}:\mathbf{a}^{B1}\cdot\mathbf{t}_1^{(1)}>$$

$$<\mathbf{AS1}^{B2}>=\frac{1+\xi}{4}<-\mathbf{a}^{B2}\cdot\mathbf{t}_2^{(2)}:\mathbf{a}^{B2}\cdot\mathbf{t}_1^{(2)}>$$

$$<\mathbf{AS2}^{A1}>=\frac{1-\eta}{4}<-\mathbf{a}^{A1}\cdot\mathbf{t}_2^{(2)}:\mathbf{a}^{A1}\cdot\mathbf{t}_1^{(2)}>$$

$$<\mathbf{AS2}^{A2}>=\frac{1+\eta}{4}<-\mathbf{a}^{A2}\cdot\mathbf{t}_2^{(3)}:\mathbf{a}^{A2}\cdot\mathbf{t}_1^{(3)}>$$

$$<\mathbf{AS2}^{B1}>=\frac{1-\xi}{4}<-\mathbf{a}^{B1}\cdot\mathbf{t}_2^{(4)}:\mathbf{a}^{B1}\cdot\mathbf{t}_1^{(4)}>$$

$$< \mathbf{AS2}^{B2} >= \frac{1+\xi}{4} < -\mathbf{a}^{B2} \cdot \mathbf{t}_2^{(3)} : \mathbf{a}^{B2} \cdot \mathbf{t}_1^{(3)} >$$

where $\mathbf{n}^{A1}$,$\mathbf{n}^{A2}$,$\mathbf{n}^{B1}$ and $\mathbf{n}^{B2}$ are the unit normal vectors at point $A1$, $A2$, $B1$ and $B2$:

$$\mathbf{n}^{A1} = \frac{\mathbf{n}_1 + \mathbf{n}_2}{|\mathbf{n}_1 + \mathbf{n}_2|}$$

$$\mathbf{n}^{A2} = \frac{\mathbf{n}_3 + \mathbf{n}_4}{|\mathbf{n}_3 + \mathbf{n}_4|}$$

$$\mathbf{n}^{B1} = \frac{\mathbf{n}_1 + \mathbf{n}_4}{|\mathbf{n}_1 + \mathbf{n}_4|}$$

$$\mathbf{n}^{B2} = \frac{\mathbf{n}_2 + \mathbf{n}_3}{|\mathbf{n}_2 + \mathbf{n}_3|}$$

$$\mathbf{a}^{A1} = \mathbf{a}_1^{A1} = \frac{1}{2}(\mathbf{X}_2 - \mathbf{X}_1)$$

$$\mathbf{a}^{A2} = \mathbf{a}_1^{A2} = \frac{1}{2}(\mathbf{X}_3 - \mathbf{X}_4)$$

$$\mathbf{a}^{B1} = \mathbf{a}_1^{B1} = \frac{1}{2}(\mathbf{X}_4 - \mathbf{X}_1)$$

$$\mathbf{a}^{B2} = \mathbf{a}_1^{B2} = \frac{1}{2}(\mathbf{X}_3 - \mathbf{X}_2)$$

$$\mathbf{t}_1^{(i)} = \mathbf{t}_{1i} \ ; \quad \mathbf{t}_2^{(i)} = \mathbf{t}_{2i} \qquad (i = 1, 2, 3, 4)$$

The real shear strain is written as :

$$\{\gamma_s\} = [\mathbf{B}_{c0}]\{\mathbf{u}_n\} \tag{8}$$

where

$$[\mathbf{B}_{c0}] = [C_0]^T [\mathbf{B}_{c\xi}]$$

The virtual shear strain is :

$$\{\gamma_s^*\} = [\mathbf{B}_{c0}]\{\mathbf{u}_n^*\} \tag{9}$$

The internal work due to shear strain is given by :

$$W_c^e = \int_{V^e} < \gamma_s^* > [\mathbf{G}]\{\gamma_s\} dV \tag{10}$$

Adding equations (6) and (10) yields the internal work of one element :

$$W_k^e = W_{mf}^e + W_c^e \tag{11}$$

As $dV = dzdA$, using equations (4), (5) and (6) yields the internal work due to the effect of membrane bending :

$$W_{mf}^e =< \mathbf{u}_n^{*e} > [\mathbf{K}_{mf}^e]\{\mathbf{u}_n^e\} \tag{12}$$

where

$$[\mathbf{K}_{mf}^e] = \int_{V^e}([\mathbf{B}_0]^T + z[\mathbf{B}_1]^T)[H]([\mathbf{B}_0] + z[\mathbf{B}_1])dzdA$$

and using equations (8), (9) and (10) yields the internal work due to the shear strain :

$$W_c^e =< \mathbf{u}_n^{*e} > [\mathbf{K}_c^e]\{\mathbf{u}_n^e\} \tag{13}$$

with

$$[\mathbf{K}_c^e] = \int_{V^e}[\mathbf{B}_{c0}]^T[\mathbf{G}][\mathbf{B}_{c0}]dzdA$$

Equations (11), (12) and (13) give the following stiffness matrix :

$$[\mathbf{K}^e] = [\mathbf{K}^e_{mf}] + [\mathbf{K}^e_c] \tag{14}$$

The elementary internal work which is the potential energy is given :

$$W^e_{int} = < \mathbf{u}^{*e}_n > [\mathbf{K}^e]\{\mathbf{u}^e_n\} \tag{15}$$

The external work due to inertial forces and concentrating forces is :

$$W^e_{ext} = < \mathbf{u}^{*e}_n > \{\mathbf{F}\} - < \mathbf{u}^{*e}_n > [\mathbf{M}^e]\{\ddot{\mathbf{u}}^e_n\} \tag{16}$$

where **F** is the nodal solicitation vector which represents the aerodynamic loads transferred from the CFD solver (see section 3.4), $\mathbf{M}^e$ is the elementary mass matrix which is given by the following equation :

$$[\mathbf{M}^e] = \int_{V^e}([\mathbf{N}]^T \rho [\mathbf{N}] dz dA$$

According to the conservation law of energy, equations (15) and (16) yield the following equations of motion for any element :

$$\mathbf{M}^e\ddot{\mathbf{u}}^e + \mathbf{D}^e\dot{\mathbf{u}}^e + \mathbf{K}^e\mathbf{u}^e = \mathbf{F}^e \tag{17}$$

The elementary displacement vector is composed of 20 degrees of freedom which corresponds to the total degrees of freedom of the four nodes with five degrees of freedom per node (three translations and two rotations).

The variables θ_{1i} and θ_{2i} of node i are defined differently according to the local coordinate system of each element since the elements attached to a node have different orthogonal base matrix $\mathbf{Q}_i$ at this point. They must be expressed by the global Cartesian coordinate system. Suppose the rotation vector $\boldsymbol{\theta}$ is expressed by θ_1, θ_2, θ_3 in the local coordinate system and by θ_X, θ_Y, θ_Z in the global coordinate system, it can be expressed as :

$$\boldsymbol{\theta} = \left\langle \begin{array}{ccc} \mathbf{t}_1 & \mathbf{t}_2 & \mathbf{n} \end{array} \right\rangle \left\{ \begin{array}{c} \theta_1 \\ \theta_2 \\ \theta_3 \end{array} \right\} = \left\langle \begin{array}{ccc} \mathbf{i} & \mathbf{j} & \mathbf{k} \end{array} \right\rangle \left\{ \begin{array}{c} \theta_X \\ \theta_Y \\ \theta_Z \end{array} \right\}$$

The rotation of the normal (see section 2.2.1.2) does not change by adding the component of θ in the normal direction since :

$$\boldsymbol{\beta} = \boldsymbol{\theta} \wedge \mathbf{n} = (\theta_1 \mathbf{t}_1 + \theta_2 \mathbf{t}_2 + \theta_3 \mathbf{t}_3) \wedge \mathbf{n} = -\theta_1 \mathbf{t}_2 + \theta_2 \mathbf{t}_1 = \beta_1 \mathbf{t}_1 + \beta_2 \mathbf{t}_2$$

Therefore, a small work which is negligible compared to the total energy of the system can be added to the internal work of each element for the purpose of transforming the coordinate system :

$$W_z = < \theta^*_{zn} > [\mathbf{K}_z]\{\theta_{zn}\}$$

with

$$[\mathbf{K}_z] = \alpha E \int_{A^e} < \begin{array}{cc} N_{,\xi} & N_{,\eta} \end{array} > [\mathbf{C}^0]^T [\mathbf{C}^0] \left\{ \begin{array}{c} N_{,\xi} \\ N_{,\eta} \end{array} \right\} J d\xi d\eta$$

where E is the material elastic modulus. α is a small coefficient which depends on the computer precision (between $1.0E-4$ and $1.0E-7$). $\mathbf{K}_z$ is a matrix with dimension 4×4 which corresponds to the rotation around the normal of the four nodes. The matrix $\mathbf{K}^e_c$ in equation (15) is expressed by a matrix of dimension 24×24 after adding matrix $\mathbf{K}_z$ [77]

After the transformation of the coordinate system, the virtual and real displacements become :

$$\{\mathbf{u}_n\} = < U_1 \;\; V_1 \;\; W_1 \;\; \theta_{X1} \;\; \theta_{Y1} \;\; \theta_{Z1} \;\; U_2 \;\; V_2 \;\; W_2 \;\; \theta_{X2} \;\; \theta_{Y2} \;\; \theta_{Z2}$$
$$U_3 \;\; V_3 \;\; W_3 \;\; \theta_{X3} \;\; \theta_{Y3} \;\; \theta_{Z3} \;\; U_4 \;\; V_4 \;\; W_4 \;\; \theta_{X4} \;\; \theta_{Y4} \;\; \theta_{Z4} >^T$$

$$\{\mathbf{u}_n^*\} = < U_1^* \;\; V_1^* \;\; W_1^* \;\; \theta_{X1}^* \;\; \theta_{Y1}^* \;\; \theta_{Z1}^* \;\; U_2^* \;\; V_2^* \;\; W_2^* \;\; \theta_{X2}^* \;\; \theta_{Y2}^* \;\; \theta_{Z2}^*$$
$$U_3^* \;\; V_3^* \;\; W_3^* \;\; \theta_{X3}^* \;\; \theta_{Y3}^* \;\; \theta_{Z3}^* \;\; U_4^* \;\; V_4^* \;\; W_4^* \;\; \theta_{X4}^* \;\; \theta_{Y4}^* \;\; \theta_{Z4}^* >^T$$

After assembling all elementary matrices, one obtains the following global equations :

$$\mathbf{M\ddot{u}} + \mathbf{Ku} = \mathbf{F} \tag{18}$$

where **u** is the global nodal displacement vector. **M** and **K** are global mass and stiffness matrices which are symmetrical and positively defined. **F** is the global solicitation vector which represents aerodynamic loads on the structural nodes.

BIBLIOGRAPHY

[1] Dowell, E. H. (1995). A Modern course in aeroelasticity (3rd rev. and enlarged ed.). Dordrecht, Pays-Bas : Kluwer Academic.

[2] Rifai, S. M., Johan, Z., Wang, W. P., Grisval, J. P., Hughes, T. J. R., & Ferencz, R. M. (1999). Multiphysics simulation of flow-induced vibrations and aeroelasticity on parallel computing platforms. *Computer Methods in Applied Mechanics and Engineering*, 174(3-4), 393-417.

[3] Cobun, P. (1987). New Approaches Speed X-33 Support at Marshall Center. *MARSHALL STAR*, Vol. 38 / Num. 8, October 22, 1997, NASA, Marshall Space Flight Center, Alabama.

[4] Kumar, A., Drummond, J. P., McClinton, C., R., & Hunt, J. L. (2001). Research in Hypersonic Airbreathing Propulsion at the NASA Langley Research Center. ISABE-2001 : Invited Lecture 4, NASA Langley Research Center.

[5] Farhat, C., Geuzaine, P., & Brown, G. (2003). Application of a three-field nonlinear fluid-structure formulation to the prediction of the aeroelastic parameters of an F-16 fighter. *Computers & Fluids*, 32(1), 3-29.

[6] Soulaïmani, A., BenElHajAli, A., & Feng, Z. (2004). A Parallel-Distributed Approach for Multi-Physic Problems with Application to Computational Nonlinear Aeroelasticity. *the Canadian Aeronautics and Space Journal*, 50(4), p. 221-235.

[7] Bisplinghoff, R. L., Ashley, H. (1962). Principles of Aeroelesticity. John Wiley and Sons, Inc.

[8] Fung, Y. C. (1969). An Introduction to the Theory of Aeroelasticity. Dover publications.

[9] Martin, E. D. (1974). A Generalized-Capacity-Matrix Technique for Computing Aerodynamic Flows. *Computers and Fluids*, Vol. 2, pp. 79-97.

[10] Bakhle, M. A., Mahajan, A. J., keith, T. G., & Stefko, G. L. (1991). Cascade Flutter Analysis with Transient Response Aerodynamics. *Computers and Structures*, Vol. 41, No. 5, pp. 1073-1085.

[11] Laporte, R. (1980). Lift improvement of an aerofoil by periodic deformations. *International Journal of Engineering Science*, 18(7), 957-970.

[12] Albano, E., & Rodden, W. P. (1969). Doublet-lattice method for calculating lift distributions on oscillating surfaces in subsonic flows. *AIAA Journal*, 7(2), 279-285.

[13] Rodden, W. P., Giesing, J. P., Kalman, T. P. (1971). New developments and applications of the subsonic Doublet-Lattice method for nonplanar configurations. *symposium on Unsteady Aerodynamics for Aeroelastic in interfering Surfaces*, AGARD CO-80-71, part II,1971.

[14] Chipman, R. R., & Rauch, F. J. (1975). Analytical and experimental study of the effects of wing-body aerodynamic interaction on space shuttle subsonic flutter. NASA Contractor Reports.

[15] Mykytow, W. J., Noll, T. E., Huttsell, L. J., & Shirk, M. H. (1972). Investigations concerning the coupled wing-fuselage-tail flutter phenomenon. *Journal of Aircraft*, 9(1), 48-54.

[16] Kalman, T. P., Rodden, W. P., & Giesing, J. P. (1971). Application of the Doublet-Lattice Method to nonplanar configurations in subsonic flow. *Journal of Aircraft*, 8(6), 406-413.

[17] The MacNeal-Schwendler Corporation. (1994). *MSC/NASTRAN Aeroelastic Analysis User's Guide*. Version 68, October, 1994.

[18] James, R. M. (1972). On the remarkable accuracy of the vortex lattice method. *Computer Methods in Applied Mechanics and Engineering*, 1(1), 59-79.

[19] Kida, T., & Take, T. (1983). A vortex-lattice method in the linear theory on a two-dimensional supercavitating flat plate foil. *Computer Methods in Applied Mechanics and Engineering*, 36(2), 191-205.

[20] Mook, D. T., & Nayfeh, A. H. (1990). Numerical simulations of dynamic/aerodynamic interactions. *Computing Systems in Engineering* 1(2-4), 461-482.

[21] Bristow, D. R., & Hawk, J. D. (1982). Subsonic panel method for the efficient analysis of multiple geometry perturbations. NASA Contractor Reports.

[22] Johnston, C. E., Youngren, H. H., & Sikora, J. S. (1985). Engineering applications of an advanced low-order panel method. Paper presented at the Aerospace Technology Conference & Exposition., Long Beach, CA, USA.

[23] Ojha, S. K., Shevare, G. R. (1985). Exact solution for wind tunnel interference using the panel method. *Computers & Fluids*, 13(1), 1-14.

[24] Petrie, J. A. H. (1978). Surface source and vorticity panel method. *Aeronautical Quarterly*, 29(pt 4), 251-269.

[25] Schippers, H. (1982). Application of multigrid methods for integral equations to two problems from fluid dynamics. *Journal of Computational Physics*, 48(3), 441-461.

[26] Marshall J. G., & Imregun M. (1996). A review of aeroelasticity methods with emphasis on turbomachinery applications. *Journal of Fluids and Structures*, 10(3), 237-267.

[27] Edwards, J. W., & Malone, J. B. (1992). Current status of computational methods for transonic unsteady aerodynamics and aeroelastic applications. *Computing Systems in Engineering*, 3(5), 545-569.

[28] Goorjian, P. M., & Guruswamy, G. P. (1988). Transonic unsteady aerodynamic and aeroelastic calculations about airfoils and wings. *Computers & Structures*, 30(4), 929-936.

[29] Wissink, A. M., Lyrintzis, A. S., & Chronopoulos, A. T. (1996). Efficient Iterative Methods Applied to the Solution of Transonic Flows. *Journal of Computational Physics*, 123(2), 379-393.

[30] Isogai, K. (1979). On the transonic-dip mechanism of flutter of a sweptback wing. *AIAA Journal*, 17(7), 793-795.

[31] Isogai, K. (1981). Transonic dip mechanism of flutter of a sweptback wing -2. *AIAA Journal*, 19(9), 1240-1242.

[32] Lee-Rausch, E. M., & Batina, J. T. (1993). Calculation of AGARD Wing 445.6 Flutter Using Navier-Stokes Aerodynamics. *AIAA Paper* No.93-3476.

[33] Yates, E. C., Land, N. S., & Foughner, J. T. (1963). Measure and calculated subsonic and transonic flutter characteristics of a 45° sweptback wing planform in air and in Freon-12 in the Langley transonic dynamic tunnel. NASA Technical note, D-1616, March 1963.

[34] Whitlow, J., W., Hafez, M. M., & Osher, S. J. (1987). An entropy correction method for unsteady full potential flows with strong shocks. *Journal of Fluids and Structures*, 1(4), 401-414.

[35] Batina, J. T., Bennett, R. M., Seidel, D. A., Cunningham, H. J., & Bland, S. R. (1988). Recent advances in transonic computational aeroelasticity. *Computers & Structures*, 30(1-2), 29-37.

[36] Holst, T. L. (2000). Transonic flow computations using nonlinear potential methods. *Progress in Aerospace Sciences*, 36(1), 1-61.

[37] Shankar, V., & Ide, H. (1988). Aeroelastic computations of flexible configurations. *Computers & Structures*, 30(1-2), 15-28.

[38] Guruswamy, G. P. (1988). Interaction of fluids and structures for aircraft applications. *Computers & Structures*, 30(1-2), 1-13.

[39] Morgan, K., Peraire, J., Peiro, J., & Hassan, O. (1991). The computation of three-dimensional flows using unstructured grids. *Computer Methods in Applied Mechanics and Engineering*, 87(2-3), 335-352.

[40] Mortchelewicz, G. D. (2000). Flutter simulations. *Aerospace Science and Technology*, 4(1), 33-40.

[41] Kousen, K. A. (1989). Nonlinear phenomena in computational transonic aeroelasticity. Ph.D. Thesis, University Microfilms International, Ann Arbor, Mich.

[42] Piperno, S., Farhat, C., & Larrouturou, B. (1995). Partitioned procedures for the transient solution of coupled aroelastic problems Part I : Model problem, theory and two-dimensional application. *Computer Methods in Applied Mechanics and Engineering*, 124(1-2), 79-112.

[43] Leger, T. J., Wolff, J. M., & Beran, P. S. (1999). Improved determination of aeroelastic stability properties using a direct method. *Mathematical and Computer Modelling*, 30(11-12), 95-110.

[44] Beckert, A. (2000). Coupling fluid (CFD) and structural (FE) models using finite interpolation elements. *Aerospace Science and Technology*, 4(1), 13-22.

[45] Farhat, C., Lesoinne, M., & Le Tallec, P. (1998). Load and motion transfer algorithms for fluid/structure interaction problems with non-matching discrete interfaces : Momentum and energy conservation, optimal discretization and application to aeroelasticity. *Computer Methods in Applied Mechanics and Engineering*, 157(1-2), 95-114.

[46] Farhat, C., & Lesoinne, M. (2000). Two efficient staggered algorithms for the serial and parallel solution of three-dimensional nonlinear transient aeroelastic problems. *Computer Methods in Applied Mechanics and Engineering*, 182(3-4), 499-515.

[47] Farhat, C. (1995). High performance simulation of coupled nonlinear transient aeroelastic problems. AGARD Report R-807, Special Course on Parallel Computing in CFD, NATO, october 1995.

[48] Farhat, C., Lesoinne, M., & Maman, N. (1995). Mixed explicit/implicit time integration of coupled aeroelastic problems : Three-field formulation, geometric conservation and distributed solution. *International Journal for Numerical Methods in Fluids*, 21(10), 807-835.

[49] Cebral, J. R., & Lohner, R. (1997). Fluid-Structure Coupling : Extensions and Improvements. *AIAA-97-0858*.

[50] Lohner, R. (1988). An adaptive finite element solver for transient problems with moving bodies. *Computers & Structures*, 30(1-2), 303-317.

[51] Maman, N., & Farhat, C. (1995). Matching fluid and structure meshes for aeroelastic computations : A parallel approach. *Computers & Structures*, 54(4), 779-785.

[52] Hassan, O., Probert, E. J., Morgan, K., & Weatherill, N. P. (2000). Unsteady flow simulation using unstructured meshes. *Computer Methods in Applied Mechanics and Engineering*, 189(4), 1247-1275.

[53] Guruswamy, G. P. (1990). Ensaero–A multidisciplinary program for fluid/structural interaction studies of aerospace vehicles. *Computing Systems in Engineering*, 1(2-4), 237-256.

[54] Formaggia, L., Peraire, J., & Morgan, K. (1988). Simulation of a store separation using the finite element method. *Applied Mathematical Modelling*, 12(2), 175-181.

[55] Donea, J., Giuliani, S., & Halleux, J. P. (1982). An arbitrary lagrangian-eulerian finite element method for transient dynamic fluid-structure interactions. *Computer Methods in Applied Mechanics and Engineering*, 33(1-3), 689-723.

[56] Hughes, T. J. R., Liu, W. K., & Zimmermann, T. K. (1981). Lagrangian-Eulerian finite element formulation for incompressible viscous flows. *Computer Methods in Applied Mechanics and Engineering*, 29(3), 329-349.

[57] Takashi Nomura, & Hughes, T. J. R. (1992). An arbitrary Lagrangian-Eulerian finite element method for interaction of fluid and a rigid body. *Computer Methods in Applied Mechanics and Engineering*, 95(1), 115-138.

[58] Soulaimani, A.,& Saad, Y. (1998). An arbitrary lagrangian Eulerian finite element formulation for solving three-dimensional free surface flows. *Comput. Maths. Appl. Mech. Engrg*, 162, 79-106.

[59] Soulaïmani, A., Forest, A., Feng, Z., BenElhadj, A., & Azami, A. (2001). A distributed Computing-based Methodology for Computational Nonlinear Aeroelasticity. Proceeding, 8th Aerodynamics Symposium, Toronto, Canada, 2001, 123-135.

[60] Farhat, C., Lesoinne, M., & Le Tallec, P. (1998). Load and motion transfer algorithms for fluid/structure interaction problems with non-matching discrete interfaces : Momentum and energy conservation, optimal discretization and application to aeroelasticity. *Computer Methods in Applied Mechanics and Engineering*, 157(1-2), 95-114.

[61] Elkadri E, N. E., Soulaimani, A., & Deschenes, C. (2000). A finite element formulation of compressible flows using various sets of independent variables. *Computer Methods in Applied Mechanics and Engineering*, 181(1-3), 161-189.

[62] Elkadri E, N. E. (1995). Une Méthode d'Éléments Finis pour la Dynamique des Gaz et Conception Orientée Objet du Code de Calcul. Ph. D thèse, Département de Génie Mécanique, Faculté des sciences et de génie, Université Laval, Québec.

[63] Farhat, C., & Lesoinne, M. (1996). On the accuracy, stability, and performance of the solution of three-dimensional nonlinear transient aeroelastic problems by partitioned procedures. *AIAA-96-1388*.

[64] Lesoinne, M., & Farhat, C. (1996). Geometric conservation laws for flow problems with moving boundaries and deformable meshes, and their impact on aeroelastic computations. *Computer Methods in Applied Mechanics and Engineering*, 134(1-2), 71-90.

[65] Farhat, C., Lesoinne, M., Stern, P., & Lanteri, S. (1997). High performance solution of three-dimensional nonlinear aeroelastic problems via parallel partitioned algorithms : methodology and preliminary results. *Advances in Engineering Software*, 28(1), 43-61.

[66] Koobus, B., & Farhat, C. (1999). Second-order time-accurate and geometrically conservative implicit schemes for flow computations on unstructured dynamic meshes. *Computer Methods in Applied Mechanics and Engineering*, 170(1-2), 103-129.

[67] Lepage, C. Y., & Habashi, W. G. (2000). Conservative Interpolation of Aerodynamic Loads for Aeroelastic Computations. *AIAA 2000-1449*, Atlanta.

[68] Salah, N. B., Soulaimani, A., & Habashi, W. G. (1999). A full-coupled finite element method for the solution of the 3D MHD equations with a GMRES-based algorithm. *AIAA paper No. 99-3322*.

[69] Soulaïmani, A., Ben Salah, N., & Saad, Y. (2002). Enhanced GMRES acceleration techniques for some CFD problems. *International Journal of Computational Fluid Dynamics*, 16(1), pp. 1-20.

[70] Price, S. J. (1999). Aeroelasticity. Course notes, Mcgill University, Montreal.

[71] Bendiksen, O. O. (2004). Nonlinear mode interactions and period-tripling flutter in transonic flow. *Journal of Fluids and Structures*, 19(5), 591-606.

[72] Price, S. J., Lee, B. H. K., & Alighanbari, H. (1993). Analysis of the post-instability behaviour of a two-dimensional airfoil with a structural nonlinearity. Paper presented at the 34th AIAA/ASME/ASCE/AHS/ASC Structures, Structural Dynamics and Materials Conference, Apr 19-22 1993, La Jolla, CA, USA.

[73] Price, S. J., & C.Mardsen. (2001). An Evaluation of Aeroelastic Parameter Identification Using Sine-Sweep Excitation. Proceeding, 8th Aerodynamics Symposium, Toronto, Canada, 111-120.

[74] Rothwell, A. (1991). Multi-level optimization of aircraft shell structures. *Thin-Walled Structures*, 11(1-2), 85-103.

[75] Piperni, P., Abdo, M., & Kafyeke, F. (2003). The Building Blocks of A Multi-Disciplinary Wing Design Method. Paper presented at the CASI 50th Conference, Montreal.

[76] Fielding, P. J. (1999). Introduction to Aircraft Design. Combridge University Press.

[77] Batoz, J.-L., & Dhatt, G. (1992). Modélisation des structures par éléments finis (Vol. 3). Sainte-Foy Paris : Presses de l'Université Laval, Hermès.

[78] Dhatt, G., & Touzot, G. (1981). Une présentation de la méthode des éléments finis. Sainte-Foy Paris : Presses de l'Université Laval, Maloine.

[79] Lê, N. V. (2000). Éléments finis en applications. Notes de cours, Département Génie Mécanique, École Technologie Supérieure, Université du Québec, Montréal.

[80] Gmür, T. (1997). Dynamique des structures analyse modale numérique. Lausanne, Suisse : Presses polytechniques et universitaires romandes.

[81] Liu, F., Cai, J., & Zhu, Y. (2001). Calculation of Wing Flutter by a Coupled Fluid-Structure Method. *Journal of Aircraft*, Vol. 38(No. 2), 334-342.

[82] Sato,T., Obayashi, S., & Nakahashi, K. (2000). Aerodynamic and Aeroelastic Simulation of Unsteady Flows over Wings. 8th Annual Conference of the CFD, Montreal, Canada, vol.2, 643-650.

[83] Faucher, V., & Combescure, A. (2003). A time and space mortar method for coupling linear modal subdomains and non-linear subdomains in explicit structural dynamics. *Computer Methods in Applied Mechanics and Engineering*, 192(5-6), 509-533.

[84] Guruswamy, G. P. (2002). A review of numerical fluids/structures interface methods for computations using high-fidelity equations. *Computers & Structures*, 80(1), 31-41.

[85] Kuethe, A. M., & Chow, C.-Y. (1986). Foundations of aerodynamics : bases of aerodynamic design (4th ed.). New York, N.Y. : J. Wiley and Sons.

[86] Warsi, Z. U. A. (1999). Fluid dynamics : theoretical and computational approaches (2nd ed.). Boca Raton, Flor. : CRC Press.

[87] Soulaïmani, A., BenElHajAli, A., & Feng, Z. (2002). Nonlinear Computational Aeroelasticity : Formulations and Solution Algorithms. NATO-AVT, Meeting Proceedings RTO-MP-089, pp. 45-01 to 45-13.

[88] Soulaimani, A., Fortin, M., Dhatt, G., & Ouellet, Y. (1991). Finite element simulation of two- and three-dimensional free surface flows. *Computer Methods in Applied Mechanics and Engineering*, 86(3), 265-296.

[89] Holt, M., & Meade, J., A. J. (1992). Flight vehicle aerodynamics calculated by a Galerkin finite element/finite difference method. *Computing Systems in Engineering*, 3(1-4), 413-421.

[90] Farhat, C., Lesoinne, M., & Maman, N. (1995). Mixed explicit/implicit time integration of coupled aeroelastic problems : Three-field formulation, geometric conservation and distributed solution. *International Journal for Numerical Methods in Fluids*, 21(10), 807-835.

[91] Saad, Y. (1996). Iterative methods for sparse linear systems. Boston, Mass. : PWS Publishing.

[92] Saad, Y., & Schultz, M. H. (1986). GMRES : a generalized minimal residual algorithm for solving nonsymmetric linear systems. *SIAM Journal on Scientific and Statistical Computing*, 7(3), 856-869.

[93] Soulaimani, A., & Fortin, M. (1994). Finite element solution of compressible viscous flows using conservative variables. *Computer Methods in Applied Mechanics and Engineering*, 118(3-4), 319-350.

[94] Ben Salah, N., Soulaimani, A., & Habashi, W. G. (2001). A finite element method for magnetohydrodynamics. *Computer Methods in Applied Mechanics and Engineering*, 190(43-44), 5867-5892.

[95] Batoz, J.-L., & Dhatt, G. (1990). Modélisation des structures par éléments finis (Vol. 1). Sainte-Foy Paris : Presses de l'Université Laval, Hermès.

[96] Hughes, T. J. R.,& Brooks, A. (1979). A multidimensioal upwind scheme with no crosswind diffusion. *Finite element methods for convection dominated flows*, (ed. T.J.R. Hughes) AMD Vol. 34, Amer. Soc. of Mech. Eng., New York, 19-35.

[97] Soulaimani, A., Saad, Y., & Rebaine, A. (2001). An edge based stabilized finite element method for solving compressible flows : formulation and parallel implementation. *Computer Methods in Applied Mechanics and Engineering*, 190(49-50), 6735-6761.

[98] Soulaimani, A., Fortin, M., Ouellet, Y., Dhatt, G., & Bertrand, F. (1987). Simple continuous pressure elements for two- and three-dimensional incompressible flows. *Computer Methods in Applied Mechanics and Engineering*, 62(1), 47-69.

[99] Brooks, A. N., & Hughes, T. J. R. (1982). Streamline upwind/Petrov-Galerkin formulations for convection dominated flows with particular emphasis on the incompressible Navier-Stokes equations. *Computer Methods in Applied Mechanics and Engineering*, 32(1-3), 199-259.

[100] Soulaïmani, A., BenElhajAli, A., & Feng, Z. (2002). A distributed Computing-based Methodology for Nonlinear Aeroelasticity. *Paper AIAA 2002-0868, 40th Aerospace sciences, Meeting & Exhibit*, January 2002, Reno, NV.

[101] Farhat, C., Geuzaine, P., & Grandmont, C. (2001). The Discrete Geometric Conservation Law and the Nonlinear Stability of ALE Schemes for the Solution of Flow Problems on Moving Grids. *Journal of Computational Physics*, 174(2), 669-694.

[102] Yates, E. C. (1987). AGARD Standard Aeroelastic Configuration for Dynamics Response. Candidat Configuration I.-Wing 445.6. NASA TM 100492.

[103] Bouchra, Y. (2003). Contribution au développement et à la validation d'un code d'éléments finis pour des problèmes d'élasto-acoustique. Mémoire de Maîtrise, Département de Génie Mécanique, Université du Québec à Montréal.

[104] Soulaïmani, A., Feng, Z., & Ben Haj Ali, A. (2005). Solution techniques for multiphysics problems with application to computational nonlinear aeroelasticity. *Nonlinear Analysis*, In Press.